# Analysis of the Transition Between Tubular Modular Track and Ballasted Railway

by

Deon Visser

*Thesis presented in partial fulfilment of the requirements for the degree of Master of Science in Civil Engineering at the University of Stellenbosch*

Department of Civil Engineering,
University of Stellenbosch,
Private Bag X1, Matieland 7602, South Africa.

Supervisor: Dr. JAvB Strasheim

March 2016

# Declaration

By submitting this thesis electronically, I declare that the entirety of the work contained therein is my own, original work, that I am the sole author thereof (save to the extent explicitly otherwise stated), that reproduction and publication thereof by Stellenbosch University will not infringe any third party rights and that I have not previously in its entirety or in part submitted it for obtaining any qualification.

Signature:  ...............................................................

D Visser

Date:                    March 2016

# Abstract

Tubular Modular Track (TMT) is a relatively new rail design invented in 1989. The system is ballastless and is designed to continuously support the rails on twin reinforced concrete (RC) beams which are founded on a specially designed subgrade. These RC beams are linked together by galvanised steel gauge bars which encircle the RC beams and provide links to fasten the rails to the RC beams with the use of rail clip fasteners. Elastomeric pads are placed in-between the rail and the RC beam to provide shock and sound absorption and grout is placed below the RC beams to level the TMT beams and ensure constant contact between the RC beams and the subgrade. With the introduction of high speed trains and ballastless rail systems the design of the transitions between ballasted and ballastless rails needs special attention. Multiple studies have been done on transitions between various types of ballastless rail and ballasted rail, but limited research is available on transitions between TMT and ballasted rail. To improve the confidence in the use of the TMT system in a transition various analyses are performed on the RC beam, the main supporting component of the system, for varying train speeds and varying rail irregularity angles due to elevation changes in the rail which occur because of ballast settlement at the track transition.

The TMT structure is supported by different layers of subgrade which need to be incorporated in the finite element (FE) model of the system, but modelling the subgrade as a continuum increases the computational cost of the analysis. To simplify the modelling of the subgrade elastic foundation theory with plate bearing test (PBT) models are investigated. The subgrade can then be replaced with an elastic support. The PBT model and the elastic subgrade stiffness are verified by using previous research models which simulate PBT and determine an elastic stiffness to replace the subgrade.

To analyse the TMT structural components a static, three-dimensional (3D), FE model is created of the structure. The TMT 3D model is also verified using models used in previous research which analysed the TMT structure. A 3D model of the structure requires a fine mesh to accurately model the cross sections of the TMT components, making the analysis computationally expensive. To simplify the model a two-dimensional (2D) model is created using beam and plane stress elements. For the 2D model a damping factor sensitivity analysis is performed to determine the influence of damping on the behaviour of the structure. The 2D model is then loaded statically and dynamically to determine the dynamic amplification factor (DAF) for the displacements, bending moments and shear forces in the rail and RC beam.

In order to create the ballast to the TMT transition model, a model of the ballasted rail is required. A 3D discrete element (DE) model of the ballasted rail was attempted by modelling the ballast as discrete particles in the 3D space and placing the rail and sleepers on the particles. The discrete element method (DEM) was found to be a complex method of modelling the ballast and required time expensive analyses. Convergence errors were encountered in the modelling and analysis process. Due to limited available assistance and knowledge the results of the DEM model were inconclusive. This problem can be attributed to the fact that DEM is a new feature introduced into the available software, i.e. Abaqus. A similar approach to the simplification, analysis and results presentation of the TMT 2D model was used for the ballasted model. Plane stress, plane strain and 2D beam elements are used and the ballast and subgrade are modelled according to the elastic foundation theory in order to simplify the ballasted rail model. To calibrate the model results displacement measurements, taken on a reference ballasted rail, are compared to the model displacement results. The model is loaded statically and dynamically to determine the DAF for the displacements of the rail and sleepers and the bending moments and shear forces of the rail are presented.

The ballast to TMT transition model is created by combining the simplified ballast and TMT 2D models. To calibrate the modelling of a transition with simplified 2D methods site displacement measurements are compared to the displacement results of a calibration model. After calibration various dynamic models are created of the ballast to TMT transition to investigate the impact of the transition on the displacements, bending moments and shear forces in the TMT RC beam. Sixteen ballast to TMT transition models with varying train speeds and irregularity angles are created and the results of these models were used in a sensitivity analysis for the response of the RC beam. Results show that RC beam displacements, maximum hogging bending moments and shear forces are sensitive to an increase in train speeds, but are more sensitive to an increase in rail irregularity angle. The maximum sagging bending moments remain constant because wheel loads remain the same for all models.

It is concluded that the design of a transition zone should focus on achieving gradual elevation change between supporting structures rather than increasing the stiffness of the ballasted structure at the transition. Regular track maintenance to limit elevation changes at the transitions due to subsidence of the ballasted rail is also of utmost importance to limit the bending moments and resulting stresses in the rail components.

# Uittreksel

Tubular Modular Track (TMT) is 'n relatiewe nuwe spoorondersteuningstelsel wat in 1989 ontwerp is. Die sisteem maak nie gebruik van ballas nie, maar is ontwerp om die spoorstawe deur middel van twee gewapende beton balke, wat op 'n spesiale grondformasie neergelê is, te ondersteun. Gegalvaniseerde staal stawe bied vasmaakplek vir die spoorstawe en word gebruik om die beton balke aan mekaar te koppel deurdat dit die balke omring. Elastomeriese kussings tussen-in die spoorstawe en beton balke verskaf skok- en klankdemping aan die sisteem en voegbry word onder die beton balke geplaas om die korrekte hoogte te verseker en om konstante kontak tussen die beton balke en fondament te verseker. Met die gebruik van hoëspoedtreine en nuwe spoorsisteme (wat nie van ballas gebruik maak nie) word spesiale aandag aan die ontwerp van oorgange tussen spore met ballas en spore sonder ballas geverg. Verskeie studies is al oor die oorgange tussen verskillende spoorsisteme gedoen, maar beperkte navorsing oor die oorgang tussen ballas-spore en TMT is beskikbaar. Om die vertroue in die gebruik van die TMT spoorsisteem in spooroorgange te verbeter is verskeie analises van die gewapende beton balke, die hoof ondersteuningskomponente van die TMT sisteem, in hierdie ondersoek uitgevoer. Die analises is met wisselende treinsnelhede en wisselende hoeke van onreëlmatigheid in die spoor, wat as gevolg van die versakking van die ballas by die spooroorgang plaasvind, uitgevoer.

Die TMT struktuur word deur verskeie formasielae wat in die eindige element (EE) model in aanmerking gebring moet word ondersteun, maar deur die formasie as 'n kontinuum te modelleer word die analise se berekeningskoste verhoog. Om die formasiemodellering te vereenvoudig word die elastiese fondasieteorie en die plaatdraagtoets (PDT) ondersoek. Dan kan die formasie met 'n elastiese ondersteuning vervang word. Die PDT en die elastiese formasiestyfheid is deur vorige navorsing, wat die PDT simuleer en die elastiese formasiestyfheid bepaal, verifieer.

'n Statiese, drie-dimensionele (3D) EE model is van die TMT struktuur geskep om die komponente van die struktuur te analiseer. Die TMT 3D model is ook deur vorige navorsing, wat die TMT struktuur analiseer het, geverifieer. Vir 'n 3D model van die struktuur word 'n fyn maas benodig om die dwarssnit van die verskeie TMT komponente akkuraat te modelleer. In terme van berekeningstyd maak dit die analise van die struktuur duur. Om die model te vereenvoudig word balk- en vlakspanningselemente gebruik om 'n twee-dimensionele (2D) model van die struktuur te skep. Die invloed van demping op die gedrag van die struktuur word bepaal deur 'n sensitiwiteitsanalise vir demping uit te voer. Daarna is die struktuur staties en dinamies belas om die dinamiese vergrotingsfaktor (DVF) vir die verplasings, buigmomente en skuifkragte in die gewapende beton balke te bepaal.

Om die model van die oorgang tussen ballas-spoor en TMT te skep word 'n model van die ballas-spoor benodig. 'n Poging was aangewend om 'n 3D diskrete element (DE) model van die ballas spoor te skep deur die ballas as diskrete partikels in die 3D ruimte te modelleer en die spoorstawe en dwarslêers bo-op die partikels te plaas. Daar is gevind dat die diskrete element metode (DEM) 'n komplekse metode is om die ballas te modelleer en dat dit tydsgewys duur is om te analiseer. Konvergeringsfoute vir die modellering en analiseproses van die DEM model was teëgekom. Die resultate van die DEM model was, as gevolg van beperkte kennis en beperkte toegang tot bystand, onbeslis. Die probleem kan toegeskryf word daaraan dat DEM 'n nuwe toevoeging tot die beskikbare sagteware (Abaqus) is. Vir die vereenvoudiging, analise en die aanbieding van resultate van die ballasmodel was 'n soortgelyke benadering as die vir die TMT model gebruik. Om die model te vereenvoudig is 2D balk-, vlakspannings- en vlakvervormingse-lemente gebruik en die ballas en formasielae is volgens die elastiese fondasieteorie gemodelleer. Verplasingsmetings, gemeet op 'n verwysings ballas-spoor, is met die model se verplasingsresul-tate vergelyk om die model te kalibreer. Daarna is die struktuur staties en dinamies belas om die DVF vir die verplasings van die spoorstaaf en dwarslêers en die buigmomente en skuifkragte van die spoorstaaf te bepaal.

Die model van die oorgang tussen die ballas-spoor en TMT is geskep deur die onderskeie, vereenvoudigde 2D modelle met mekaar te kombineer. Om die modellering van die oorgang met vereenvoudigde 2D modelle te kalibreer is verplasingsmetings van 'n bestaande spoor met die verplasingsresultate van 'n kalibrasie oorgangsmodel vergelyk. Na kalibrasie is daar verskeie dinamiese modelle van die oorgang tussen die ballas-spoor en TMT geskep om die impak van die oorgang op die verplasings, buigmomente en skuifkragte in die TMT gewapende beton balke te bepaal. Sestien oorgangsmodelle met wisselende treinsnelhede en onreëlmatigheidshoeke is geskep en die resultate van hierdie modelle is in 'n sensitiwiteitsanalise vir die reaksie van die beton balke gebruik. Die resultate wys dat die verplasings, sakkingsbuigmomente en skuifkragte in die beton balke sensitief vir 'n verhoging in treinsnelheid is, maar nog meer sensitief vir 'n verhoging in die onreëlmatigheidshoek is. Die opbuigingsmomente bly konstant, omdat die wiellaste vir al die modelle konstant bly.

Die gevolgtrekking word gemaak dat 'n oorgansone 'n geleidelike oorgang in die ligging van die spoor tussen verskillende spoorsisteme moet bied, in plaas daarvan om die styfheid van die ballas-spoor by die oorgang te verhoog. Gereelde spooronderhoud is ook uiters belangrik om die veranderinge in spoorligging, as gevolg van versakking in die ballas-spoor by die spooroorgang, te beperk, om die buigmomente en gevolglike spannings in die spoorkomponente te beperk.

# Acknowledgements

First and foremost I thank the Lord for helping me complete my thesis and I would like to express my gratitude to the following people for their contribution to my thesis:

Dr JAvB Strasheim for his support, input and guidance.

Prof PJ Gräbe for the provision of the displacement measurements on the reference rail.

Greg Mitchell and Hellmut Bowles of FEAS (Pty) Ltd for their technical support with the Abaqus models.

My parents for their constant support and encouragement throughout my studies.

Liné Loubser for her love and constant support and for believing in my abilities to complete my thesis when I did not. I could not have done it without you.

# Contents

CONTENTS                                                                                        x

# List of Figures

# List of Tables

# List of Abbreviations

| | |
|---|---|
| 2D | Two-dimensional |
| 3D | Three-dimensional |
| BOEF | Beam on Elastic Foundation |
| DE | Discrete Element |
| DAF | Dynamic Amplification Factor |
| DEA | Discrete Element Analysis |
| DEM | Discrete Element Method |
| FE | Finite Element |
| FEA | Finite Element Analysis |
| FEM | Finite Element Method |
| FWC | Flangeway Clearance |
| PBT | Plate Bearing Test |
| PVC | Polyvinyl Chloride |
| RC | Reinforced Concrete |
| RP | Reference Point |
| TMT | Tubular Modular Track |
| TT | Tubular Track |

# List of Symbols

| Symbol | Description | Units |
|---|---|---|
| $a$ | Ellipse major axis | [mm] |
| $A$ | Cross section area | [m$^2$] |
| $A_s$ | Shear cross section area | [m$^2$] |
| $b$ | Ellipse minor axis | [mm] |
| $\mathbf{C}$ | Damping matrix | [-] |
| $C_n$ | Normal direction contact damping | [N.s/m$^2$] |
| $C_t$ | Tangential direction contact damping | [N.s/m$^2$] |
| $D$ | Shear force | [N] |
| $E$ | Young's modulus | [MPa] |
| $E^*$ | Function of E and $\upsilon$ | [-] |
| $f$ | Frequency | [Hz] |
| $g$ | Gravitational acceleration | [m/s$^2$] |
| $G$ | Shear modulus | [N/m$^2$] |
| $h$ | Cant | [m] |
| $h_d$ | Cant deficiency | [m] |
| $H_w$ | Cross wind force | [kN] |
| $I$ | Moment of inertia | [mm$^4$] |
| $k$ | Stiffness | [N/m] |
| $k_s$ | Modulus of subgrade reaction | [N/mm$^3$] |
| $\mathbf{K}$ | Stiffness matrix | [-] |
| $K_n$ | Normal direction contact stiffness | [N/m] |
| $K_t$ | Tangential direction contact stiffness | [N/m] |
| $L$ | Length | [m] |
| $L_c$ | Characteristic length | [m] |
| $L_k$ | Klingel lateral movement wavelength | [m] |
| $L^*$ | Hunting lateral movement wavelength | [m] |
| $m$ | Mass of train per wheelset | [kg] |
| $M$ | Bending moment | [N.m] |
| $\mathbf{M}$ | Mass matrix | [-] |
| $p$ | Pressure | [MPa] |
| $p_c$ | Vehicle centre of gravity distance | [m] |
| $p_w$ | Distance of lateral wind force resultant | [m] |

| | | |
|---|---|---|
| $P$ | Force | [N] |
| $q$ | Pressure | [MPa] |
| $q(w)$ | Distributed load | [N/m] |
| $Q_{centr}$ | Increase in vertical load due to centrifugal force | [kN] |
| $Q_{dyn}$ | Dynamic wheel load components | [kN] |
| $Q_{stat}$ | Static wheel load | [kN] |
| $Q_{tot}$ | Total vertical load | [kN] |
| $Q_{wind}$ | Increase in vertical load due to cross wind | [kN] |
| $r$ | Wheel radius | [m] |
| $R$ | Curve radius | [m] |
| $s$ | Gauge width | [m] |
| $t$ | Thickness | [mm] |
| $u$ | Displacement | [m] |
| $\dot{u}$ | Velocity | [m/s] |
| $\ddot{u}$ | Acceleration | [m/s$^2$] |
| $v$ | Train speed | [km/h] |
| $w$ | Displacement | [m] |
| $y_0$ | Klingel lateral movement amplitude | [mm] |
| $\ddot{y}_{max}$ | Klingel movement maximum lateral acceleration | [m/s$^2$] |
| $Y_{centr}$ | Lateral force due to centrifugal force | [kN] |
| $Y_{dyn}$ | Dynamic lateral force components | [kN] |
| $Y_{flange}$ | Lateral force exerted on outer rail due to flanging | [kN] |
| $Y_{tot}$ | Total lateral force | [kN] |
| $Y_{wind}$ | Lateral force due to cross winds | [kN] |

**Greek symbols**

| | | |
|---|---|---|
| $\alpha$ | Irregularity angle | [rad] |
| $\delta$ | Deflection | [mm] |
| $\lambda$ | Wheel conicity | [rad] |
| $\mu$ | Friction coefficient | [-] |
| $\omega_n$ | Natural frequency | [Hz] |
| $\sigma$ | Stress | [MPa] |
| $\theta$ | Angle between local axes | [rad] |
| $\upsilon$ | Poisson's ratio | [-] |
| $\varphi$ | Track quality factor | [-] |
| $\xi$ | Damping ratio | [-] |

# Chapter 1

# Introduction

Tubular Modular Track (TMT) is a relatively new rail design which was invented in 1989 by the South African, Peter Küsel [29, 52]. Unlike a conventional rail, where the rails are supported by wood or concrete sleepers and ballast, the TMT system is ballastless. The rails are continuously supported on twin reinforced concrete (RC) beams laid on a specially designed subgrade. These RC beams are held together by galvanised steel gauge bars which encircle the RC beams and the rails are tied to the beams using standard rail clip fasteners. Elastomeric pads are placed between the rail and RC beam to provide shock and sound absorption and a grout layer is placed beneath the RC beams to help level the rail line and ensure constant contact with the ground [55]. Some of the components of the TMT system are visible in Figure 1.1.

With the introduction of high speed trains the problem of transitions between ballastless and ballasted rails has been identified. According to Lei and Mao [30] a transition is the location where there is an abrupt change in the vertical track stiffness. Shan et al. [43] has a similar opinion, explaining the transition as an area where there is an abrupt change in the track stiffness and adds that deformation variations in the railway between two systems help describe the transition. A transition between TMT and ballasted rail is shown in Figure 1.1.



Figure 1.1: Transition between TMT and ballasted rail.

Rail vehicles passing across these transitions induce dynamic shock effects in the ballast and beam supported rails and their respective substructures. These effects cause peak stress and strain levels at the transition zone [49]. If these transitions are not maintained regularly the ballast will deteriorate at an accelerated rate leading to pumping of ballast, swinging or hanging sleepers, permanent deformations, worn track components and loss of surface and gauge. These effects could create the potential for a train derailment [30].

A major problem that arises at transitions is the differential settlement of the different rail support structures and foundations, which creates an irregularity angle. The irregularity angle is the angle of the rail in the transition zone between the different types of rail systems. This difference in track settlement increases the vertical interaction forces between the wheels of the rail vehicle and the rail; the vertical acceleration of the rail vehicle; and the vertical acceleration of the rail [30].

Through experience, according to Shan et al. [43], it is known that transition zones between two different rail types provide smoother transfers from the stiffer, ballastless rail to the less stiff, ballasted railway, or from less stiff to more stiff. This ensures that the settling of the ballast will be more even.

There has been extensive research done on the transition between different types of rail support structures and multiple solutions have been recommended for the negative effects occurring at these transitions [30, 43, 49, 57, 36]. However, the specific transition between TMT and ballasted rail shows very little research done [57, 45]. The aim of this study is to investigate different methods of analysing TMT, ballasted rail and a transition between the two and what the sensitivity of the transition is to train speed and rail irregularity angle with regard to displacements, shear forces and bending moments.

Research [2, 30, 43, 4] confirms that the effects of transitions on rail structures are barely noticeable at low train speeds. The analyses done in this study will determine the behaviour of the TMT and ballasted rail structures at a speed of 94 km/h, the speed at which the reference train travelled. After the TMT and ballast models have been verified the transition model is analysed for various train speeds in order to determine the effect of the train speed on the transition. Although train speed is a determining factor of the transition behaviour, research [30] suggests that the irregularity angle of the rail has a greater influence on the behaviour of the rail. Various irregularity angles are included in the transition model and combined with the different train speeds to create a sensitivity analysis of the transition structure.

## 1.1   Research objectives

As mentioned above this study investigates different methods of analysing the considered rail structures and aims to determine the sensitivity of the TMT structure to the transition for different speeds and rail irregularity angles. To achieve this the following objectives are set:

- create a finite element (FE) model of the TMT structure;

- create a discrete element (DE) and FE model of the ballasted structure;

- combine the TMT and ballast FE models to create the transition model and implement various train speeds and rail irregularity angles;

- determine the impact of the transition on the different rail structures; and

- determine the sensitivity of the TMT structure to the transition for different variables.

The model representing the transition between TMT and ballasted rail can be broken up into three different subsections, namely the TMT, transition and ballasted sections. The TMT and ballasted sections are analysed separately to allow comparison with previous research and reference rail displacement measurements. These comparisons are intended to verify the behaviour of the TMT and ballasted models. When verified the different models are combined to create the rail transition model.

## 1.2 Thesis outline

In Chapter 2 sections 2.1, 2.2 and 2.3 describe the ballasted, transition and TMT sections of the transition structure respectively. A short description of the features of each component of the transition system such as geometry, model material properties, operational characteristics and structural functions is provided. Some geometrical details of the TMT and ballasted systems have not been described in detail in order to protect the intellectual property of the involved parties.

Chapter 3 provides a summary of the research relevant to this investigation done to date in the form of a literature review.

- Section 3.1 covers the interaction between the wheel and the rail. The interaction between the wheel and rail includes the guidance of the train by the rails and the contact between the wheel and the rail as described by the Hertz contact theory.

- Elastic foundation theory is investigated in Section 3.2. The elastic foundation theory allows the replacement of the foundation layers by springs which model the stiffness of the foundation. Three methods used to replace the foundation with springs, the Winkler and Pasternak foundation, and the method of determining the spring stiffness with the plate bearing test (PBT) are investigated to describe the elastic foundation theory.

- The possible load parameters of the rail are explained in Section 3.3. The loads covered are the static loads, namely vertical, lateral and longitudinal rail forces and dynamic loading of the railway including the use of the dynamic amplification factor (DAF).

- Finally Section 3.4 describes the discrete element method (DEM). DEM is used to model the ballasted rail. The section covers methods of DEM modelling and the theory behind DEM.

Chapter 4 summarizes the research methodology of the thesis, explaining the methods used to create the models and the analysis methods of these models.

Chapter 5 covers the separate analysis of the TMT section and the results obtained from these analyses.

- In Section 5.1 the available FEM elements and the element types assigned to TMT components are described.

- Section 5.2 explains the methods of contact enforcement between the TMT components.

- Section 5.3 discusses analysis methods and results of the subgrade investigation.

- The behaviour of the TMT section when statically loaded is investigated in Section 5.4.

- In Section 5.5 the behaviour of the TMT section when a moving load is applied is investigated.

The ballasted rail structure is investigated in Chapter 6 and discusses methods of modelling the ballasted rail in 3D DEM and 2D FEM. These methods are implemented to create a static 3D DEM model of the rail and then simplify the model to a static and dynamic 2D FEM model. To ensure accurate modelling the results of these models are calibrated with displacement measurements of a reference rail. With the ballasted model calibrated the 2D TMT model and 2D ballasted model can be combined to create the ballast to TMT transition model.

In Chapter 7 modelling the transition with simplified 2D FEM models is calibrated with displacement measurements of a reference transition structure. The calibrated methods are used to create the ballast to TMT transition models, with train speed and rail irregularity angle as variables, and a sensitivity analysis is performed for the RC beam of the TMT structure under the various variable conditions.

- Section 7.1.1 discusses the calibration ballast-Sonneville transition model created to calibrate the simplified 2D transition model and the following section presents the results of the calibration model and compares them to the reference transition measurements.

- Section 7.1.3 describes the various ballast to TMT transition models created to perform the sensitivity analysis of the RC beam. The subsequent section presents the results of the various analyses in the form of a sensitivity analysis.

Conclusions on the dynamic behaviour of the transition between ballast and TMT are provided in Chapter 8, as well as some conclusions on the separate behaviour of the TMT structure and ballasted structure. The sensitivity of the TMT structure to the different variables at the transition is discussed; recommendations are given for modelling the transition as a 2D FEM model and approaching the problem of transitions between ballast and TMT; and suggestions are made for future research for topics which fall outside the scope of this study.

# Chapter 2

# Rail Transition Sections

A typical rail transition consists of three different sections: a stiff rail system; a less stiff rail system and a transition zone between the two systems. In this study the stiff system is the TMT structure and a ballasted rail structure is the less stiff system. The transition zone is a part of the ballasted structure where the ballast has been stabilized in some manner, different kinds of stabilisation are investigated below. The behaviour, components and properties of the three different sections are discussed below.

## 2.1    Ballasted Rail

Ballasted rail is the primary structure used for the construction of rail lines since the introduction of freight and passenger trains. It consists of rails, rail pads, sleepers, rail fasteners, ballast and sub-ballast. Figure 2.1 shows a typical ballasted rail, with the described components shown in Figure 2.2. The system makes use of the rails, sleepers and a ballast bed to transfer the applied loads to the subgrade. The transfer of loads relies on the principle of stress reduction where the high contact stress between the rail vehicle wheel and the rail is reduced to a manageable stress at the interface between the ballast and the subgrade by increasing the contact area [16].

Since the inception of ballasted rail the principle of its function has not changed significantly and its performance has remained satisfactory over the years by adapting and making use of new and available technology. However, with modern railway operation some of the ballasted rail disadvantages are becoming more prominent making ballastless alternatives more appealing [16].

### 2.1.1    Advantages of ballasted rail

Rail structure component configuration and sizing are determined by aspects like axle loads, train speeds, required service life, maintenance required, local conditions and availability of materials. When considering all these aspects no single type of railway structure will excel in every way and it needs to be considered which type of rail structure will perform best under

Figure 2.1: Ballasted rail [56], components of ballasted rail shown in Figure 2.2.

the prevailing conditions. Some advantages of ballasted rail, which make it an ideal option for some conditions, are listed below [16].

- It as a proven method

- Cost of construction is relatively low

- Replacement of track structure components can be done without disturbing large parts of the track

- The track geometry can be adjusted and corrected with relative ease

- Small adjustments of the track lay-out is possible

- Surface water drains away from the ballast bed well

- Good elasticity in the displacement behaviour of the ballast bed

- Good damping of sound created by vibrations in the railway

But ballasted rail also has a number of disadvantages which has lead to the recent research and developments in ballastless rail. Some of these disadvantages are [15]:

- At later stages of the rail lifespan the track starts to move ("float") in lateral and longitudinal directions due to the non-linear displacement properties of the materials

- Limited lateral acceleration of trains is allowed in curves due to the low lateral resistance of ballast

- When trains traverse the track at higher speeds (>275 km/h [37]) ballast can be churned up (thrown/shot up), which causes damage to the rails and wheels

- Decrease in drainage due to ballast fouling

### 2.1.2   Components of the ballasted rail

This study uses a ballasted rail structure based on a reference rail, which has rail transitions and supports trains travelling at speeds of up to 160 km/h. Figure 2.2 shows the components of a ballasted rail. The reference rail uses concrete sleepers with steel reinforcing and dolomite ballast. Some other components of the ballasted rail structure will be discussed in a later section.
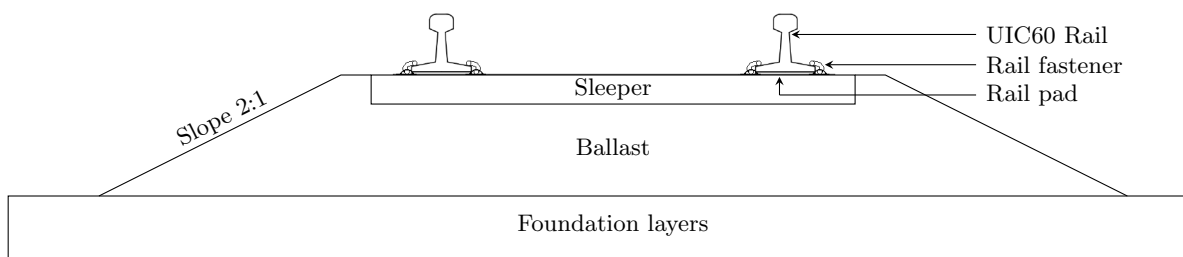


Figure 2.2: Ballasted rail cross-section.

**Ballast**

Railway ballast consists of angular crushed hard rock 25 mm to 63 mm in diameter. The rails and sleepers are placed on the ballast. The function of the ballast is to transfer forces from the rails and sleepers to the subgrade. A wide variety of materials can be used as ballast and the choice of ballast is mainly determined by availability and performance of the ballast. This variety of ballast materials consists of materials such as dolerite, greywacke, shale, pebbles, crushed granite, basalt, limestone, dolomite and slag [56, 44]. The functions of ballast are to [44]:

- resist vertical, lateral and longitudinal forces;

- provide elasticity and energy absorption;

- provide voids for fouling material;

- allow maintenance by tamping (recompaction of ballast underneath the sleepers);

- allow immediate drainage of water; and

- reduce the pressure below the sleeper to acceptable levels at the subgrade.

The ballast bed gains its compressive strength from the internal friction between the crushed rock particles, but it has no tensile strength and limited lateral strength. The ballast bed

typically has a thickness of 250 - 300 mm measured from the lower face of the sleeper to the surface of the subgrade. The particles contained in the ballast bed should be hard, be resistant to wearing, have a good particle distribution, be cubic in shape and have sharp edges [16].

Figure 2.3 shows the grading requirements for freight transport as specified by Transnet Freight Rail [44]. The ballast used for this study has a grading range between 26.5 mm and 63 mm and the material is dolomite, which is a sedimentary carbonate rock. Figure 2.4 shows the dolomite ballast as used in a rail line and Table 2.1 summarizes the typical material properties of ballast.

Table 2.1: Dolomite ballast material properties [54, 44].

| Young's Modulus [GPa] | Poisson's Ratio [−] | Density [kg/m³] |
|---|---|---|
| 52 | 0.25 | 2 830 |
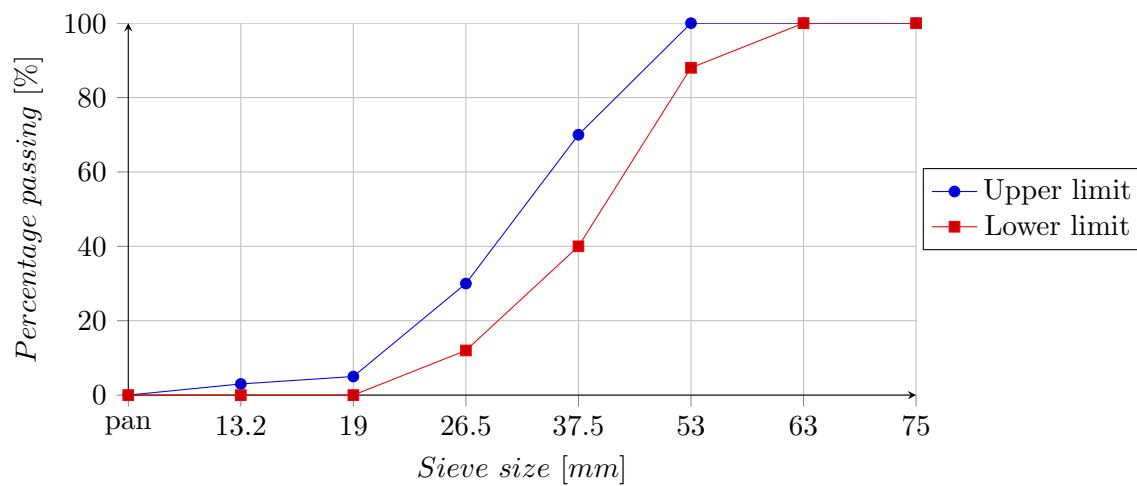


Figure 2.3: Specifications for ballast according to Transnet [44].



Figure 2.4: Dolomite ballast [44].

**Sleepers**

Rail sleepers are typically made of concrete or wood, the sleepers used for this study are concrete sleepers. Sleepers are placed underneath the rails and on top of the ballast to transfer vertical loads from the rails to the ballast. In order to resist longitudinal and transverse forces the sleepers need to be embedded within the ballast. Ballast underneath the sleepers needs to be compacted in such a way that the sleepers are only supported at the areas beneath the rail and not in the middle or edges of the sleepers. This can cause the sleepers to bend and change the gauge measurement or inclination of the rails. The main functions of sleepers are to:

- provide support and fixing positions for rail footings and fasteners;

- withstand rail forces and transfer them to the ballast;

- maintain rail gauge and inclination;

- act as insulators between the rails; and

- resist other impacts, like mechanical influences and weathering.

The sleepers used for the reference rail are B70 concrete sleepers. Figure 2.5 shows an example of such a sleeper and Table 2.2 describes the characteristics of the sleeper.
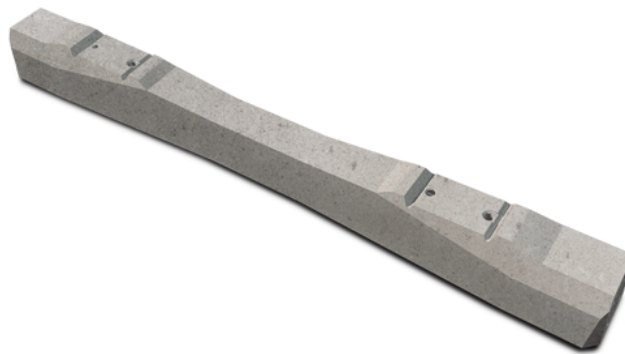


Figure 2.5: B70 concrete sleeper example [39].

Table 2.2: B70 concrete sleeper characteristics [39].

| | | |
|---|---:|---|
| Permissible axle load | 25 | tonne |
| Maximum speed | 250 | km/h |
| Weight | 280 | kg |
| Length | 2 600 | mm |
| Width | 300 | mm |
| Sleeper height | 234 | mm |
| Height of rail-seat centre | 214 | mm |
| Height of sleeper centre | 175 | mm |

## 2.2 Tubular Modular Track

TMT is a ballastless rail system with a structure providing continuous support to the rail, unlike ballasted rail where support is only provided at intervals where sleepers are placed. The TMT rails are continuously supported on twin RC beams laid on a specially designed subgrade. These RC beams are held together by galvanised steel gauge bars to provide lateral support to the structure. Elastomeric pads are placed on top of the beams and underneath the rails to provide shock and sound absorption. The rails are tied to the beams using standard rail clip fasteners. A grout layer is placed beneath the RC beams to help level the structure and ensure constant contact with the ground [55]. Figure 2.6 shows a cross section of this system.
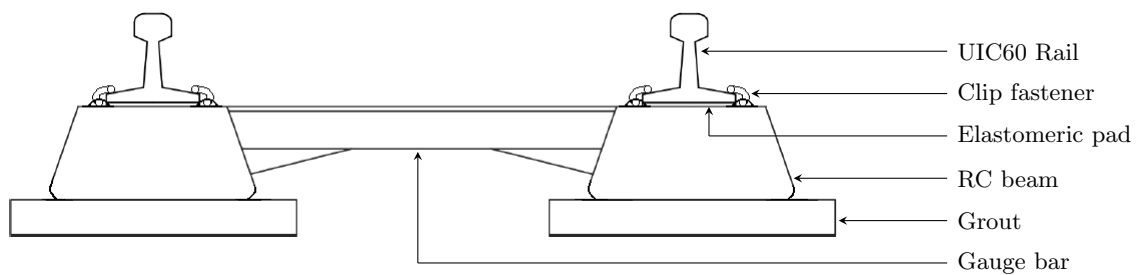


Figure 2.6: TMT cross section.

### 2.2.1 Advantages of the TMT structure

Site-specific requirements of the TMT structure can be satisfied by designing the structure to suit different load types, operating speeds, annual tonnages and prevailing geotechnical conditions. After designing the system according to the specific requirements the modules are created by assembling the pre-cast RC beams and gauge tie bars off-site. These modules can then be transported to a specific site where they are placed in position and the elastomeric pads and rails are added to the structure. Figure 2.7 shows a pre-manufactured module and a constructed TMT rail. Manufacturing the modules in this manner reduces the construction time of the rail, reduces the risk of faulty construction and allows faster traffic readiness [55].



Figure 2.7: A pre-manufactured module and a completed TMT rail [55].

Some of the main advantages of TMT over ballasted rail are [20]:

- Lower stresses on the subgrade due to a larger effective contact area

- Reduced deflections resulting in longer lifespan of the rail

- Less required maintenance for geometry correction

- Decrease in earthworks due to narrower structure

- Improved stability of the track

- No fouling of ballast, good for desert conditions

- Good alternative when ballast is not readily available

- Continuous rail support provided

### 2.2.2 Components of the TMT structure

The TMT structure consists of the components shown in Figure 2.6. Below follows a description of each component. The rail and rail clip fasteners are discussed in a later section.

**Elastomeric pad**

The elastomeric pad, which is placed between the rail and the RC beam, decreases the stiffness of the contact between the rail and the RC beam. This decrease in stiffness increases deflections and reduces noise and high-frequency vibrations of the track [55]. These attributes of the elastomeric pad ensure a smoother ride and decrease the damage on the RC beam created by the impact of the rail on the RC beam. The elastomeric pad also provides a constant contact patch between the rail and the RC beam and provides a larger distribution area for stresses, eliminating stress peaks in the contact area. The material properties used for the modelling of an elastomeric pad typically used in TMT construction are shown in, Table 2.3.

Table 2.3: Elastomeric pad material properties [45, 58].

| Thickness [mm] | Width [mm] | Young's Modulus [MPa] | Poisson's Ratio [$-$] | Density [kg/m$^3$] | Static Stiffness [N/mm$^3$] | Dynamic Stiffness [N/mm$^3$] |
|---|---|---|---|---|---|---|
| 5 | 150 | 32.6 | 0.35 | 900 | 2.932 | 5.255 |

**Reinforced concrete beam and grout**

The RC beam acts as a stiff beam which has to carry the bending moments and shear forces applied to it through the rail. The cross-section shape of the RC beam is shown in Figure 2.6. The steel reinforcement and the polyvinyl chloride (PVC) duct pipe (for placement of services) in the centre of the beam are not shown in Figure 2.6. The RC beam has a wider base than

Table 2.4: Concrete and grout material properties [45].

| Material | Young's modulus [MPa] | Poisson's ratio [-] | Density [kg/m$^3$] |
|---|---|---|---|
| Concrete | 27 460 | 0.2 | 2 200 |
| Grout | 12 768 | 0.25 | 2 100 |

the rail in order to distribute stresses more evenly to the subgrade and avoid high stress peaks which cannot be carried by the soil.

A layer of grout of approximately 80 mm thick is placed between the RC beam and the subgrade to ensure continuous contact between the RC beam and the subgrade. The grout also helps with levelling the RC beams and fills the gaps between the ends of the RC beams. The RC beams are typically 5.9 m long and have a gap of 100 mm between them. Table 2.4 shows the concrete and grout material properties used for modelling purposes.

**Gauge bars**

The gauge bars maintain the gauge of the structure when lateral loads are applied in curves or in other cases where cross winds or hunting of rail vehicles lead to transverse loading of the rail tracks. The bars do not contribute to the vertical stiffness of the structure. Creating the Tubular Track modules is made possible by the gauge bars which hold the RC beams together to create the module for ease of assembly and the bars provide points to fix the rail to the RC beams.

## 2.3   Transition Zone

With the introduction of high speed trains the problem of transitions between ballastless and ballasted rail has been identified. A transition is the location where two different types of rail support structures meet and an abrupt change in the vertical track stiffness occurs [30]. Rail vehicles passing across these transitions induce dynamic shock effects in the ballastless and ballast supported rails and their respective substructures. A major problem that arises at these transitions is the differential settlement of the different rail support structures and foundations.

It has been found that transition zones between two different rail types provide smoother transfers between the two types of rail structures. This ensures that the settling of the ballast will be more even and that less damage will be experienced by supporting elements [43].

The transition zone typically starts at the end of the ballastless rail and extends a certain distance into the ballasted rail. The function of the transition zone in this area of the rail is to increase the stiffness of the less stiff rail in order to decrease the jump or provide a smoother transition in stiffness between the two different types of rail structures; smoothing out the differential rail settlement over a longer distance and in effect decreasing the irregularity angle. There are various transition zones that are being used or have been researched [36, 43, 57].

(a) Extra rails.



(b) Bitumen stabilized ballast.



(c) Stiff material gradual incline.



(d) Increased sleeper cross section.



(e) Longer sleepers.



(f) Steel "fingers".



(g) Stiffer subgrade.
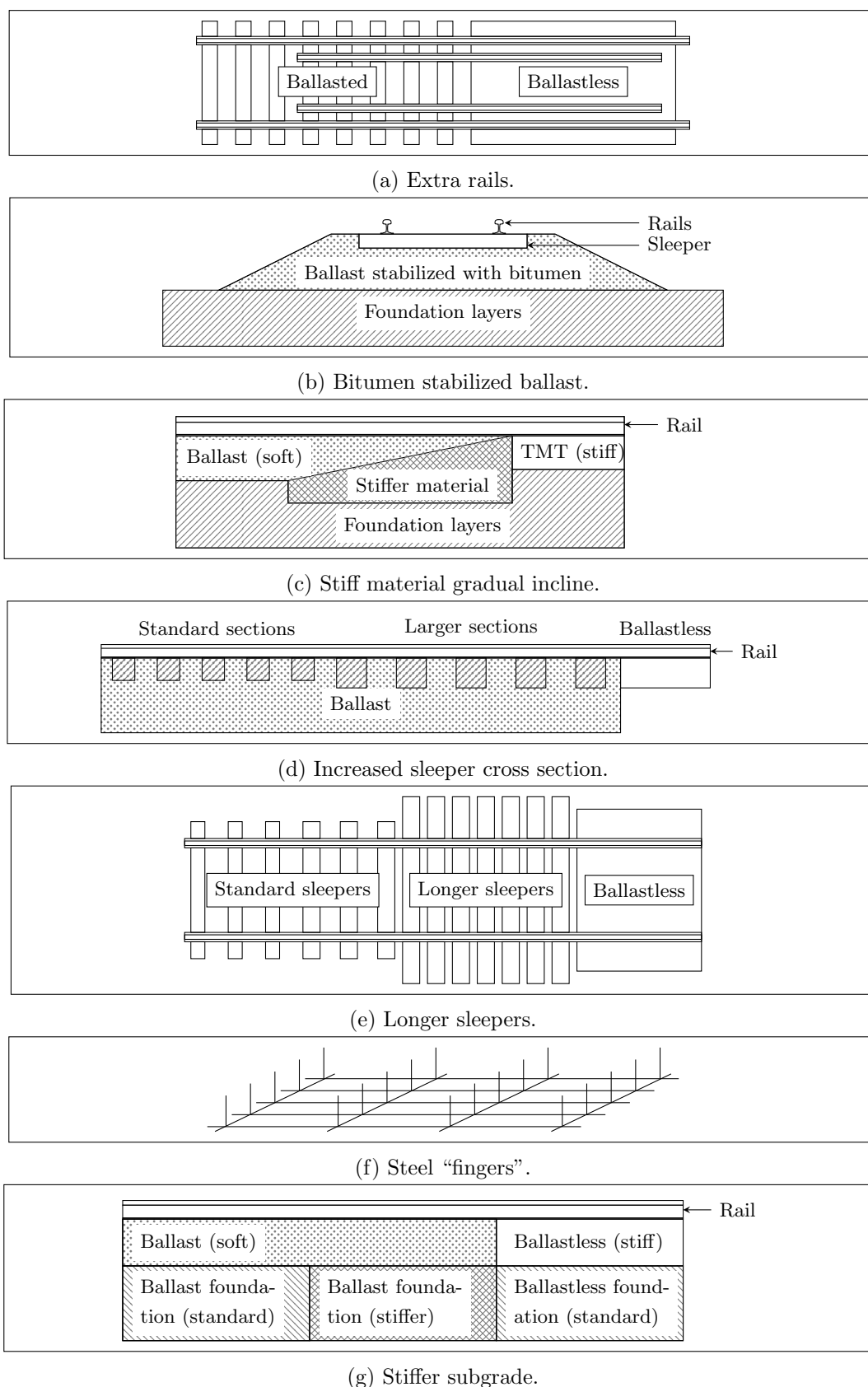
Figure 2.8: Transition zone examples.

Typical transition configurations used are:

- additional rails placed parallel to primary rails to increase stiffness Figure 2.8a;

- bitumen added to ballast for stabilization Figure 2.8b;

- gradual incline of stiffer material from underneath ballast Figure 2.8c;

- increase of sleeper cross section Figure 2.8d;

- longer sleepers at a reduced spacing Figure 2.8e;

- steel rods ("fingers") underneath ballast preventing lateral displacement of ballast Figure 2.8f;

- stiffer subgrade designs Figure 2.8g; and

- bituminous ballast as a sub ballast layer.

### 2.3.1  Transition zone length

Shan et al. [43] conducted research on a transition zone with a similar approach to the method shown in Figure 2.8g where the subgrade of a ballasted section is adapted. With a simulated train speed of 250 km/h it was suggested that the transition zone be 30 m long. Increases in the length of the transition zone showed minimal differences in the change of dynamic response of the structure. The reference train used for this study has a maximum speed of 160 km/h; however, for safety reasons, it travels at slower speeds when traversing a curve or when crossing a transition, which is why a train speed of 94 km/h is used in all subsequent models. These lower speeds could justify the shorter transition zone of 6 m which is used in the reference rail. The reference rail is the rail which is used to calibrate the ballast-TMT transition model in Chapter 7.

## 2.4  TMT to Ballast Transition

This section describes all components pertaining to the transition between TMT and ballasted rail. The components discussed in this section are:

- Rail

- Subgrade

- Configuration of rail vehicles

- Rail fasteners

### 2.4.1 Rail

Numerous rail types are available with different profiles, materials and characteristics. Each profile is created uniquely to be cost-effective, but also suit specific requirements for different rail vehicle axle loads, train speeds and types of rail use. The different types of rail use include high-speed railways, heavy-duty railways, mixed traffic railways, metro railways, tramway systems and crane rails [48]. The UIC60 rail profile is used for the reference rail of this study. The properties and dimensions of the rail are shown in Figure 2.9 and Table 2.5.
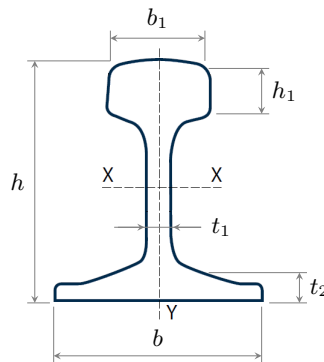


Figure 2.9: UIC60 rail profile.

Table 2.5: UIC60 rail properties and dimensions [48].

| Profile | Weight [kg/m] | Area [mm$^2$] | h [mm] | $b_1$ [mm] | $t_1$ [mm] | $t_2$ [mm] | b [mm] | $I_{xx}$ [mm$^4$] |
|---|---|---|---|---|---|---|---|---|
| UIC 60 | 60.21 | 7670 | 172 | 72 | 16.5 | 27.2 | 150 | $30.383 \times 10^6$ |

### 2.4.2 Subgrade

No subgrade information is available for a constructed transition section between TMT and ballasted rail [46]. The subgrade layers selected are based on information obtained from research done by Shaw [45] on the transition between TMT and ballasted rail. Table 2.6 shows the subgrade material properties as used by, Shaw [45]. The layer thickness values of Table 2.6 are typical thickness values for TMT subgrade design [46].

Table 2.6: Subgrade material properties [45].

| Layer | Young's modulus [MPa] | Poisson's ratio [-] | Density [kg/m$^3$] | Layer thickness [mm] |
|---|---|---|---|---|
| SSB | 250 | 0.3 | 2 100 | 200 |
| SB | 180 | 0.3 | 2 000 | 200 |
| A | 110 | 0.3 | 1 900 | 200 |
| B | 80 | 0.3 | 1 800 | 300 |
| In-situ | 60 | 0.3 | 1 700 | semi-infinite |

### 2.4.3    Configuration of rail vehicles

As discussed the train loads are based on the geometry of the reference rail vehicles. The geometry of the two central vehicles of the train used for the reference rail are shown in Figure 2.10. The wheel spacing of the leading and trailing car are the same as the two central vehicles shown in Figure 2.10. Each vehicle has two bogies with two axles each. This creates a grouping of four wheel loads at the connection between two train vehicles. How these loads are applied on the rail at the wheel-rail interaction is discussed in the following chapter. The weight of the vehicles is 16 tons per axle, which equates to a load of 78.48 kN per wheel. For the dynamic application of these loads a travelling speed of 94 km/h will be used.
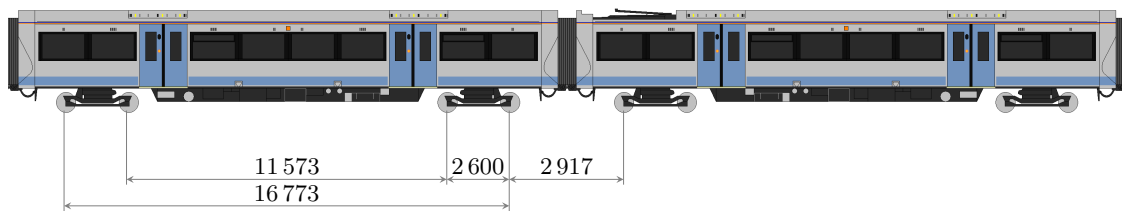
Figure 2.10: Reference rail vehicles wheel spacing.

### 2.4.4    Rail fasteners

The rail fasteners are used to provide lateral restriction and to prevent the rail from lifting from the supporting structure. They do not provide significant stiffness to the bending or shear behaviour of the structure. Figure2.11 shows the Pandrol Fastclip FE fastener, which is used for the reference rail [19].

Figure 2.11: Pandrol Fastclip FE fasterner [51].

## 2.5   Summary

The three principal components of the rail transition structure were discussed.  The ballasted section was described in terms of structural behaviour and the advantages and disadvantages thereof.  The ballast and sleeper components, which are only present in the ballasted section were described with reference to the geometry and material properties taken from the reference rail design.  The structural behaviour of the TMT structure was explained and the advantages of the system were listed and the elastomeric pad, RC beam and grout components of the system were defined.  The transition zone application was explained; some examples of transition zones were listed and a reference to a suggested transition zone length was discussed.

For the TMT to ballast transition structure the components present in all sections were described.  These components are the rail, the subgrade and the rail vehicle geometry used to define the load patterns applied to the rail.

# Chapter 3

# Literature Review

The key aspects of rail behaviour and modelling techniques that were researched and that are necessary to create an accurate model of the transition structure is discussed in this chapter. Based on the literature review done the topics dealt with in this chapter are:

- The interaction between the vehicle wheel and the rail in order to accurately model the wheel-rail contact and avoid excessive stress peaks in the rail at the point of contact between the wheel and the rail.

- The elastic foundation theory is researched, which allows for the replacement of a solid soil foundation with an elastic foundation.

- Static and dynamic loads applied to the structure are investigated.

- DEM which is used to model the discrete particles of the ballasted railway section.

## 3.1   Wheel-Rail Interaction

The interaction between the train vehicles and supporting rail is an important aspect of a railway system. Wheel and rail interaction does not only act as a method to transfer forces from the train to the subgrade, but also as guidance for the wheels. Interaction between the train vehicle and rail structure involve the wheel tread and flanges and the railhead. These components of the railway guidance system are shown in Figure 3.1.

There are multiple aspects of train behaviour that have an impact on the interaction between the wheels and the rails. Some of these aspects include dynamic behaviour of the train, the shape of the rail profile and the wheel, hunting, worn rails and wheels and the area of contact between the wheel and the rail.

This section investigates the wheel-rail guidance and Hertz contact theory to allow accurate modelling of the application of loads to the railway structure. Guidance of the rail-wheel interaction determines the type of contact occurring between the rail and wheel and whether

18
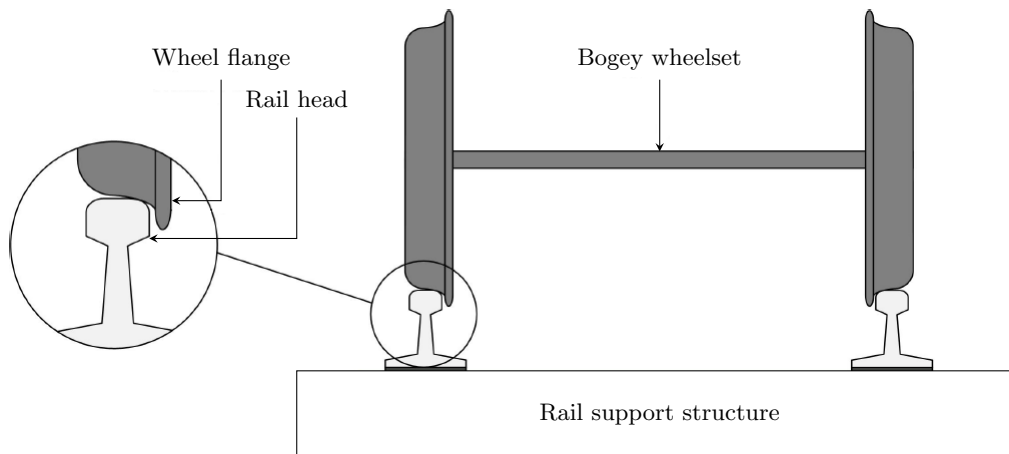
Figure 3.1: Wheel-rail guidance system.

other loads are introduced to the system, such as lateral loads.  The physical contact area between the wheel and rail needs to be given due consideration as an incorrect assumption could lead to high contact stress peaks in the rail. Hertz contact theory is used to calculate an accurate contact area between the wheel and the rail.

### 3.1.1    Wheel-rail guidance

If lateral forces are introduced to a wheelset (e.g. wind blowing on the side of the train vehicle) lateral displacement of the train vehicles occur between the rails, which is counteracted by the different radii of the wheels and the rail - the effect of the wheel-rail guidance. When this occurs a periodical movement of the wheelset ensues. This theory was described by Klingel in 1883 and is known as the Klingel movement, Figure 3.2 [16]. When the transverse periodical movement of the train vehicle increases to such an extent where flanging (interaction of the wheel flanges with the side of the rail head) occurs the movement is no longer described as Klingel movement, but as hunting.
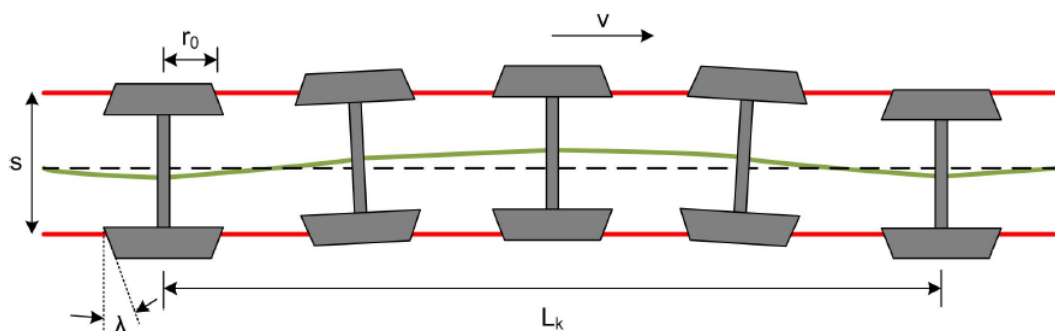


Figure 3.2: Klingel movement [16].

During Klingel movement the wheelset displaces a distance $y$ from the centreline of the rails creating a sinusoidal movement with an amplitude of $y_0$ and a wavelength of $L_k$, shown in

Figure 3.3. The value of $L_k$ can be calculated with the following equation [16]:

$$L_k = 2\pi \sqrt{\frac{r_0 s}{2\lambda}}$$
(3.1)

where
$r_0$ = wheel radius [m]
$s$ = gauge width [m]
$\lambda$ = wheel conicity (angle between wheel tread
and horizontal axis of axle) [rad]



fwc = flangeway clearance
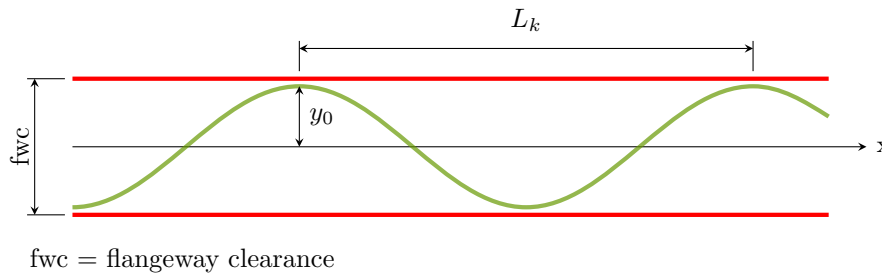
Figure 3.3: Lateral movement of wheelset.

The excitation frequency of the lateral, periodical movement can be calculated using [16]:

$$f = \frac{v}{L_k}$$
(3.2)

and the maximum lateral acceleration can be calculated with:

$$\ddot{y}_{max} = 4\pi^2 y_0 \frac{v^2}{L_k^2}$$
(3.3)

where
$v$ = train speed [m/s]

Due to slip occurring between the wheels and rails the amplitude of the transverse motion of the wheelset $y_0$ will increase until it is equal to half of the flangeway clearance (fwc). When this value of $y_0$ is achieved flanging occurs and the wheelsets start rebounding between the rails. This phenomenon, shown in Figure 3.4, is known as hunting.
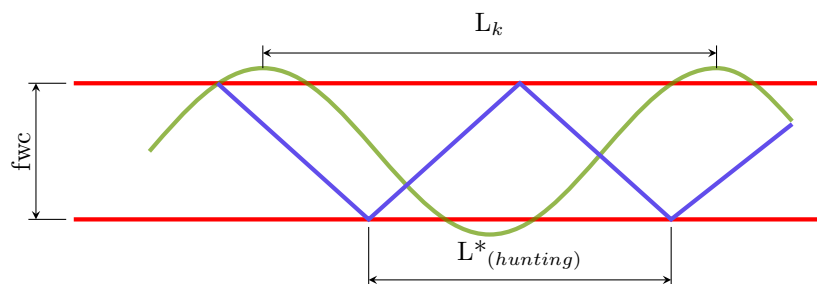


Figure 3.4: Influence of flanging on lateral movement of wheelset (hunting movement).

When hunting occurs the harmonic, lateral movement changes to a zig-zag movement, the wavelength becomes shorter, the frequency increases rapidly and reaches the critical range for

the rail vehicles and resonance occurs [16]. The critical speed at which hunting occurs is mainly determined by the stiffness and damping provided by the undercarriage of the train vehicles as well as the wheel profiles. Hunting will not be investigated, because the design of the vehicles is outside of the scope of this study and vehicle design dictates the critical speed, which is usually higher than the 94 km/h travelling speeds used for this study [10].

### 3.1.2  Hertz Contact

Wheel loads that are applied to a rail cannot be modelled with point loads since this will lead to an over-estimation of the stresses at the contact zone between the rail and the wheel. The contact force will typically act over an area, as per the Hertz contact theory.

The Hertz contact theory is commonly used to define the contact between the rail and the train wheel. The theory states that the contact area between two elastic non-conforming bodies is elliptical in shape, having a major semi-axis ($a$) and a minor semi-axis ($b$). Figure 3.5 shows this elliptical contact area. In this elliptical area the contact pressure distribution is represented by a semi-ellipsoid [59]. The ellipsoidal representation is subject to the following assumptions [28, 42]:

- all elements should have constant curvatures;

- the contact area should be small compared with characteristic dimensions;

- the significant dimensions of the ellipse must be small when compared to the dimensions of each body and the relative radii of the surfaces; and

- surfaces should be frictionless to ensure that only normal stresses arise in the contact area.

If the initial point of contact, when there is no force applied to the bodies and the initial contact area is a point, is taken as the origin of the ellipse then the surface of the contact region can be approximated by the expression

$$z_1 = A_1 x^2 + B_1 y^2 + C_1 xy + ... \tag{3.4}$$

Higher order terms of $x$ and $y$ can be neglected for this equation. Through the correct orientation of axes the $xy$ term vanishes and an equation can be written for the first surface, the surface of the first body:

$$z_1 = \frac{1}{2R_1'} x_1^2 + \frac{1}{2R_1''} y_1^2 \tag{3.5}$$

where $R_1'$ and $R_1''$ are the principal radii of curvature of the surface at the origin. The second surface, the surface of the second body, has a similar expression:

$$z_2 = -\left( \frac{1}{2R_2'} x_2^2 + \frac{1}{2R_2''} y_2^2 \right) \tag{3.6}$$

The separation between the surfaces is taken as $h = z_1 - z_2$. By modifying Equation 3.4 and
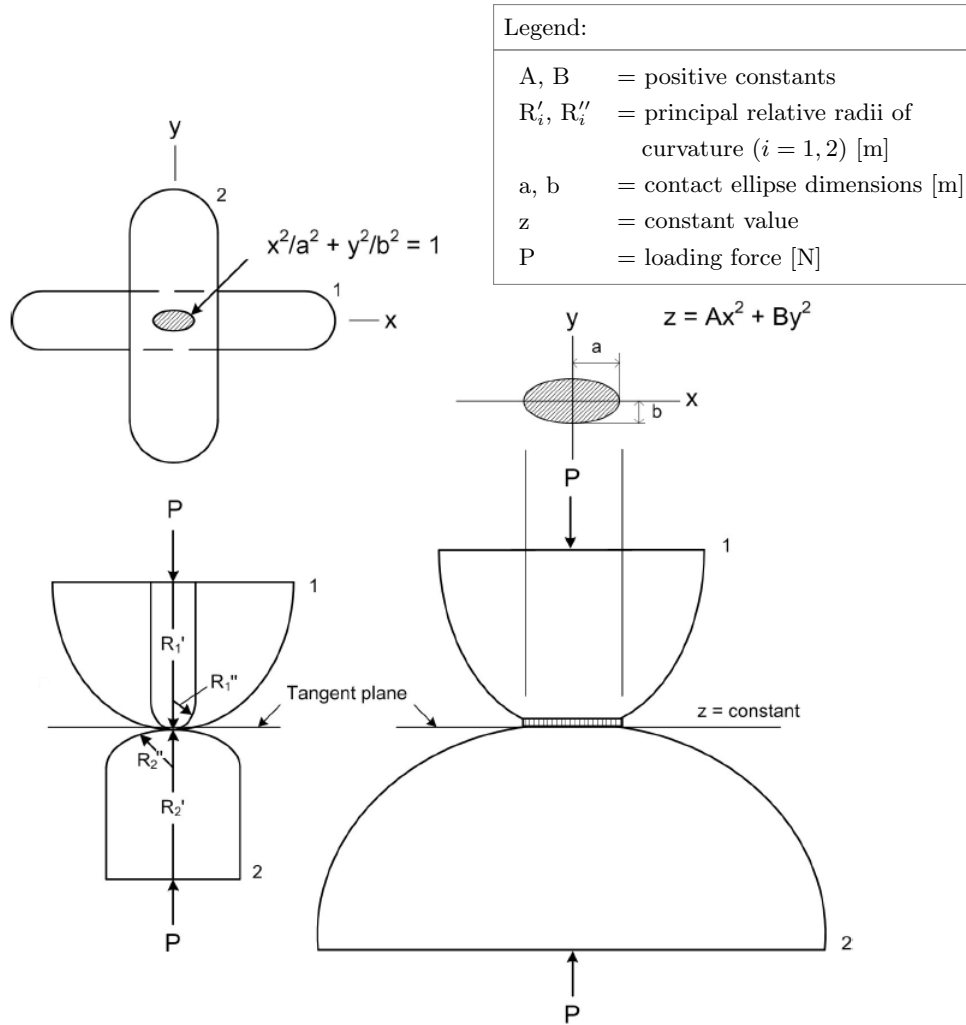
Figure 3.5: Hertz contact between elastic non-conforming bodies [58].

making a suitable choice of axes the following equation is obtained:

$$h = Ax^2 + By^2 = \frac{1}{2R'}x^2 + \frac{1}{2R''}y^2 \tag{3.7}$$

where $A$ and $B$ are positive constants and $R'$ and $R''$ are the principal relative radii of curvature. When a constant value for z is taken the contact area becomes an ellipse and the equation of this ellipse is:

$$1 = \frac{x^2}{a^2} + \frac{y^2}{b^2} \tag{3.8}$$

while the following is true for the constants $A$ and $B$ [28]:

$$|B - A| = \frac{1}{2}\left(\frac{1}{R_1'} - \frac{1}{R_1''}\right)^2 + \left(\frac{1}{R_2'} - \frac{1}{R_2''}\right)^2$$

$$+ 2\left(\frac{1}{R_1'} - \frac{1}{R_1''}\right)\left(\frac{1}{R_2'} - \frac{1}{R_2''}\right)\cos 2\theta^{\frac{1}{2}} \tag{3.9}$$

$$A + B = \frac{1}{2}\left(\frac{1}{R_1'} + \frac{1}{R_1''} + \frac{1}{R_2'} + \frac{1}{R_2''}\right) \tag{3.10}$$

To obtain the principal stresses the complete elliptical integrals $K(k')$ and $E(k')$:

$$K(k') = F(\frac{\pi}{2}, k') = \int_0^{\frac{\pi}{2}} \frac{d\theta}{\sqrt{1 - k'^2 \sin^2 \theta}} \tag{3.11}$$

$$E(k') = H(\frac{\pi}{2}, k') = \int_0^{\frac{\pi}{2}} \sqrt{1 - k'^2 \sin^2 \theta} d\theta \tag{3.12}$$

are used, where:

$$
\begin{aligned}
k &= & \frac{b}{a} = \cos \theta \\
k' &= & \sqrt{1 - k^2}
\end{aligned}
$$

Each body in contact has its own local axis which is orientated to coincide with the principal curvatures of that body. The variable $\theta$ defines the angle between these two local axes. To determine the $k$-value used in Equations 3.11 and 3.12 the following equation is used:

$$\frac{B}{A} = \frac{(\frac{1}{k^2})E(k') - K(k')}{K(k') - E(k')} \tag{3.13}$$

To obtain the values for semi-minor axis, $a$ and semi-minor axis, $b$ of the contact ellipse the equation

$$\sqrt[3]{\frac{3kE(k')}{2\pi}P(\Delta)} = ka \tag{3.14}$$

is used, where

$$\Delta = \frac{1}{A+B}\left(\frac{1 - v_1^2}{E_1} + \frac{1 - v_2^2}{E_2}\right) \tag{3.15}$$

with $E_i$ and $v_i$ ($i = 1, 2$) representing the values of the Young's modulus and Poisson's ratio for the two bodies in contact, respectively. Finally the maximum pressure at the center of contact can be calculated with [58]:

$$p_0 = \frac{3P}{2\pi ab} \tag{3.16}$$

These equations can now be used to define the contact area between two bodies as well as the maximum pressure between the two bodies in a 3D FEM package. An application has been written in Java by, Winkler [38] that performs all these calculations. The application requires:

- material properties, $E$ and $v$;

- normal force acting on bodies, $P$; and

- radii $R'$ and $R''$ of the bodies in contact

and computes:

- semi-minor axis values, $a$ and $b$;

- maximum pressure at the center of contact, $p_0$; and

- any pressure within the contact area, $p(x, y)$.

## 3.2   Foundation Behaviour

This section investigates techniques and methods to decrease the size and complexity of the FEM model by replacing the solid foundation formations with a set of springs modelling the stiffness of the foundation. This is achieved by the elastic foundation theory which is described below. In order to apply the elastic foundation theory the stiffness of the springs which will model the foundation stiffness needs to be determined. The plate bearing test (PBT) is investigated as a method of calculating the stiffness of these springs.

### 3.2.1   Elastic foundation theory

The rail structure is supported by the foundation which consists of different layers, each contributing to the vertical stiffness of the rail system. Modelling the layers in a FEM package will result in models containing too many elements which will make the analyses time expensive and complex. To simplify this complexity of the foundation a foundation model is used which is based on the elastic foundation theory. The elastic foundation theory allows the the simplification of the foundation as shown in Figure 3.6. It consists of:

- Beam with bending properties $E$ and $I$

- Elastic foundation modelled by springs with a foundation coefficient $k$

- Rigid support
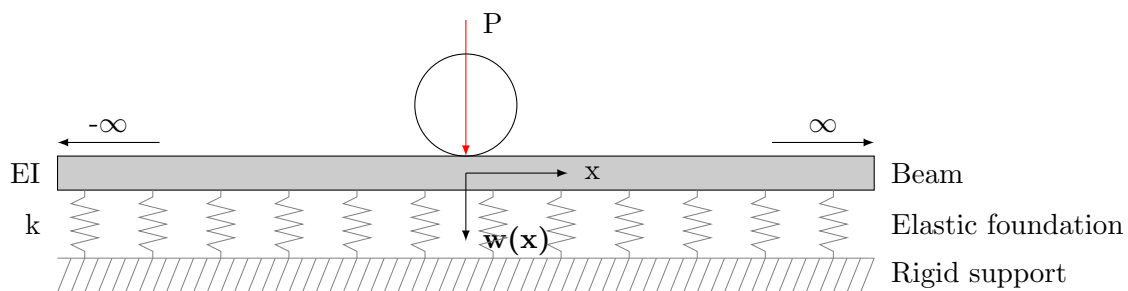


Figure 3.6: Beam on elastic foundation.

The differential equation for this configuration of the rail is

$$EI\frac{d^4w}{dw^4} + kw = q(x) \tag{3.17}$$

where

|        |   |                                |
|--------|---|--------------------------------|
| $EI$   | = | bending stiffness [N$m^2$]     |
| $k$    | = | foundation coefficient [N/$m^2$] |
| $q(x)$ | = | distributed load [N/m]         |
| $w$    | = | displacement [m]               |

Because the point loads applied to the rail are much higher than the own weight of the beam modelling the rail it is assumed that the distributed load, $q(x)$ is negligibly small. This yields

$$EI\frac{d^4w}{dx^4} = -kw \tag{3.18}$$

By integrating Equation 3.18 the shear forces, bending moments, rotations and displacements can be derived with use of suitable boundary conditions. If symmetry is applied to the model at $x = 0$ the following boundary conditions apply:

$$w(\infty) = 0; \ \frac{dw}{dx}(0) = 0; \ \frac{d^3w}{dw^3}(0) = \frac{P}{2}$$

Many models are available for the modelling of a railway substructure. Some of these models are: beam on elastic foundation (BOEF), beam on discrete supports, discretely supported beam including ballast mass, tensionless BOEF according to Kjell Arne Skoglund and Pasternak foundation [17]. The BOEF (or Winkler) and Pasternak models will be studied for the modelling of the railway foundation due to their simplicity and ease of application.

### 3.2.2   Winkler foundation

The Winkler foundation model provides the simplest representation of the continuous elastic foundation where it is assumed that the base consists of closely spaced, independent linear springs. The Winkler support hypothesis states that at each point of support the compressive stress is proportional to the local compression. This relation can be written as $\sigma = kw$ where $\sigma$ is the local compressive stress on the support, $w$ is the local displacement of the support and $k$ is the foundation coefficient [16]. Figure 3.7 shows the beam element model for the Winkler foundation. The Winkler foundation model is the model which was used to derive the differential equation shown in Equation 3.17.
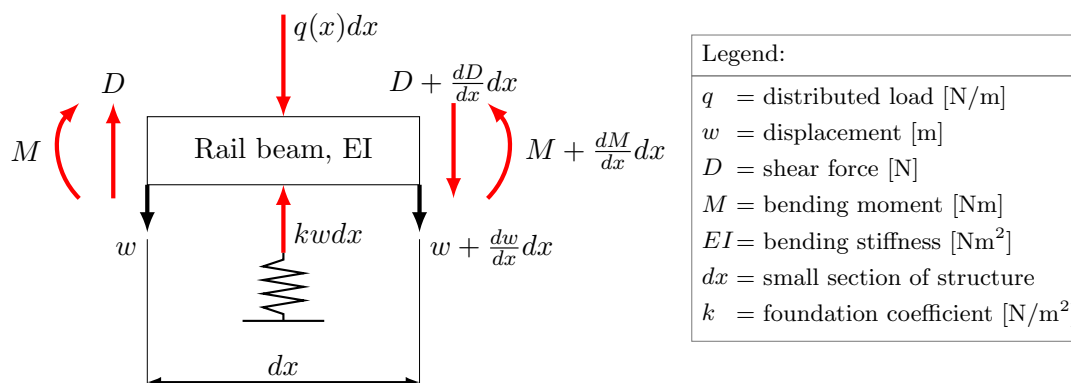


Figure 3.7: Winkler foundation model.

### 3.2.3 Pasternak foundation

The Pasternak foundation model assumes the existence of shear interactions between the spring elements that are used in the Winkler model. This shear interaction may be accomplished by connecting the ends of the springs to a beam consisting of incompressible vertical elements which only deform by transverse shear [16, 17]. This model is shown in Figure 3.8.
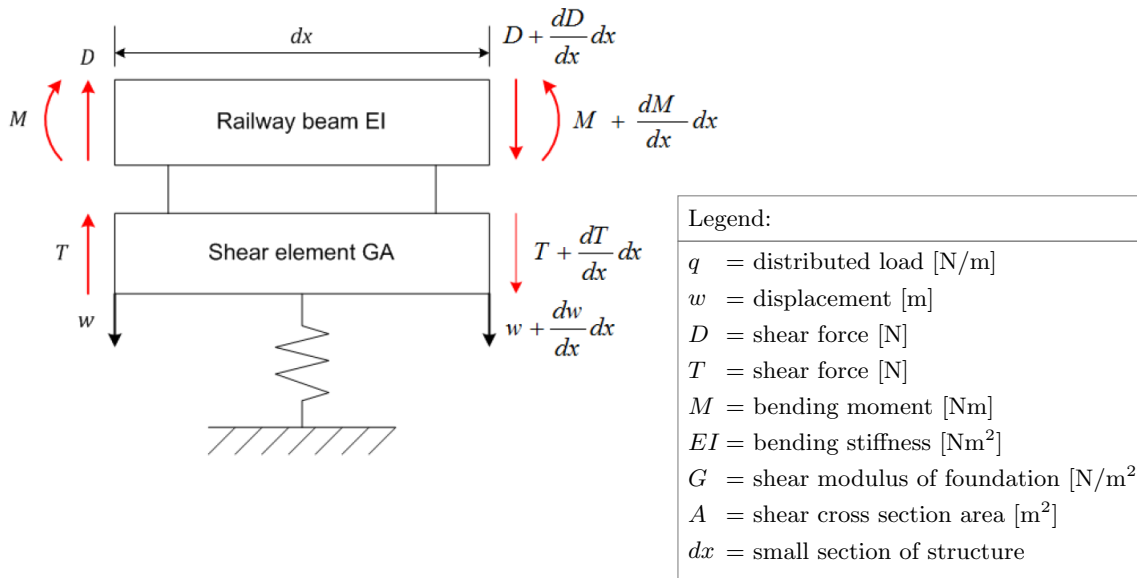


Figure 3.8: Pasternak foundation model [58].

However, this model requires the Young's modulus and Poisson's ratio of the foundation. According to Bowles [5] the methods of obtaining the Young's modulus and Poisson's ratio do not yet provide accurate enough results and other methods which require less computational complexity are preferred. This is discussed in the following section on PBTs.

### 3.2.4 Plate bearing test

The PBT is one of the available tests which can be used to test the bearing capacity of a foundation. During this test the foundation is loaded by a square steel plate of at least 300 mm squared and measurements of load and settlement are taken until failure of the soil or up to at least 1.5 times the estimated bearing capacity [8].

The modulus of subgrade reaction is used as a relationship between soil pressure and deflection and is used in structural analysis of foundation members like continuous footings, mats, and pilings. The PBT is used to determine the modulus of subgrade reaction, which is calculated as follows:

$$k_1 = \frac{q}{\delta} \tag{3.19}$$

where $q$ is the pressure applied by the plate and $\delta$ is the deflection of the plate due to the pressure applied.

The PBT is difficult to perform when plates are used that are not small in size (300 mm or

smaller). Plates larger than 450 mm tend to be less rigid than smaller plates and do not give a constant uniform deflection over the whole region of the plate. To increase the stiffness of the plate, smaller plates can be stacked concentrically on top of larger plates, but in any case the average deflection of the plate is used to create the force-displacement plot for the modulus of subgrade reaction [5].

The plot of the soil pressure versus deflection is typically a non-linear curve which can be assumed to increase linearly up to a constant deflection of $X_{max}$, where after the soil pressure can be assumed as a constant value defined by

$$q_{con} = k_1(X_{max}) \tag{3.20}$$

where $q_{con}$ is the soil pressure, $k_1$ the modulus of subgrade reaction for a square PBT and $X_{max}$ a constant deflection value.

According to Bowles [5] there is some dispute over whether the modulus of subgrade reaction should be used instead of modelling a material with $E$ and $\upsilon$ in a FEM package. In Bowles's experience using both methods he suggests that the modulus of subgrade reaction be used due to its ease of use and savings on analysis computing time at least until methods improve so that accurate values of $E$ and $\upsilon$ can be obtained.

Since the square PBT results are only accurate for small square foundations the results need to be extrapolated for use with an infinitely long foundation as used in TMT. An equation has been defined by, Terzaghi [53] to extrapolate the results for a rectangular footing:

$$k_s = k_1 \frac{m + 0.5}{1.5m} \tag{3.21}$$

where   $k_s$   =   modulus of subgrade reaction for the rectangular foundation;
        $k_1$   =   value obtained from the square PBT; and
        $m$   =   $L/B$ - the ratio of the dimensions of the rectangular footing.

Since an infinite length will be the best representation of a TMT rail line and a ballasted rail line, Verlinde [58] adapted the above equation with L'hôspital's rule to achieve the following relation between the square and rectangular modulus of subgrade reaction values:

$$k_s = k_1 \frac{1}{1.5} = 0.67k_1 \tag{3.22}$$

Bowles [5] mentions that Equation 3.21 has become outdated and does not recommend the general use thereof. To test the validity of Equations 3.21 and 3.22, Verlinde [58] compared the results of two FEM analyses. One of the analyses simulated the square PBT while the other simulated a rectangular PBT where the length of the plate was taken as the characteristic length of an infinitely long beam, calculated with

$$L_c = \sqrt[4]{\frac{4EI}{k_1}} \tag{3.23}$$

where $\quad E \quad = \quad$ Young's modulus of beam [MPa];

$\quad\quad\quad\quad I \quad = \quad$ moment of inertia of beam $[mm^4]$

Where the values of $E$ and $I$ are that of the long beam or footing placed on the foundation. The Transformed-Section Method can be used to determine $E$ and $I$ if the beam or footing consists of different material sections. Verlinde [58] calculated the characteristic length for his rectangular PBT as $6.7\,\mathrm{m}$.

## 3.3 Model Loading

To develop a strength and durability specification for a rail structure information on axle load, annual tonnage and running speed is required. These parameters will determine the static load applied, the amount of cycles applied to the railway and the dynamic amplification of static loads, respectively. Loads that are applied to the railway can generally be divided into three main directions, namely vertical, horizontal and transverse (lateral) to the track and horizontal and parallel (longitudinal) to the track. These can be divided into quasi-static and dynamic loads, which are investigated in this section.

### 3.3.1 Static Loading

Figure 3.9 shows all the possible load components of the system while the train is traversing a curve.

**Vertical rail forces**

The total vertical load on the rail can be divided into the following components, shown in Equation 3.24 [16]:

$$Q_{tot} = (Q_{stat} + Q_{centr} + Q_{wind}) + Q_{dyn} \tag{3.24}$$

where:

$Q_{stat} \quad = \quad$ the static wheel load, which is half the axle load, when measured on
$\quad\quad\quad\quad\quad$ straight, horizontal track;

$Q_{centr} \quad = \quad$ increase in outer wheel load in curves due to centrifugal force;

$Q_{wind} \quad = \quad$ increase in outer wheel load due to cross winds; and

$Q_{dyn} \quad = \quad$ dynamic wheel load components.

The maximum load on a wheel generally occurs at the outer rail, being equal to:

$$Q_{e,max} \approx 0.5G + G\frac{p_c h_d}{s^2} + H_w \frac{p_w}{s} \tag{3.25}$$

where:
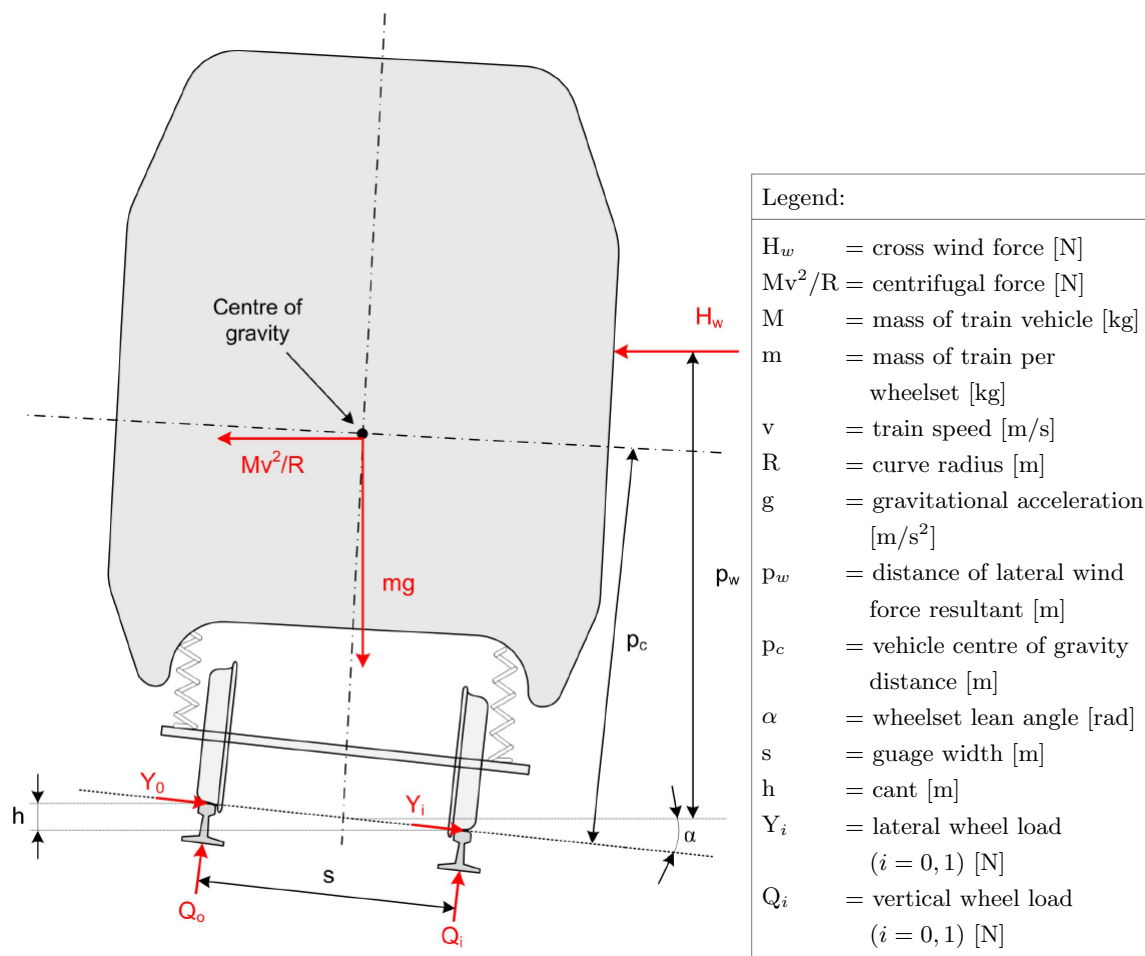
Figure 3.9: Quasi-static vehicle forces in a curve [58].

$$G \quad = \quad \text{weight of the vehicle per wheelset [N];}$$
$$h_d \quad = \quad \frac{sv^2}{gR} - h \text{ (cant deficiency) [m].}$$

**Lateral rail forces**

The total lateral force that is exerted by the wheel on the outer rail is equal to [16]:

$$Y_{tot} = (Y_{flange} + Y_{centr} + Y_{wind}) + Y_{dyn} \tag{3.26}$$

in which:

$$Y_{flange} \quad = \quad \text{lateral force exerted on outer rail due to flanging in curve;}$$
$$Y_{centr} \quad = \quad \text{lateral force due to centrifugal force;}$$
$$Y_{wind} \quad = \quad \text{lateral force due to cross winds; and}$$
$$Y_{dyn} \quad = \quad \text{dynamic lateral force components.}$$

If it is assumed that the forces created by wind and centrifugal forces act entirely on the outer rail then the maximum lateral force can be taken as:

$$Y_{e,max} \approx G\frac{h_d}{s} + H_w \tag{3.27}$$

This is only an approximation and the actual force exerted by a wheel is much more complex due to the various positions of the vehicle, several coupled wheelsets and adhesion forces between the rail and the wheel. The total lateral wheel force is therefore not predicted very accurately [16].

The ratio between the vertical forces and the lateral forces ($Y/Q$) is very important, because the increase of this ratio could lead to derailment of the rail vehicle experiencing these vertical and lateral forces. Tests have shown that the maximum value for, $Y/Q$ should be 1.2. This gives the following criterion for safety against derailment:

$$\frac{Y}{Q} \leq 1.2 \tag{3.28}$$

**Longitudinal rail forces**

Longitudinal forces are created in the rails as a result of the following [16]:

- forces induced in fixed rails due to temperature gradients;

- acceleration and braking of rail vehicles on the track;

- stresses caused by shrinkage strains due to welding of rails; and

- track creep due to track slope or train braking and acceleration.

These forces are assumed to be negligibly small when compared to the vertical and lateral forces [58]. However, they should be considered in extreme cases for example, track creep becomes noticeable in inclined rails or one direction traffic lines.

### 3.3.2 Dynamic Wheel-Rail Interaction and Loading

Rail vehicles have several springs and dampers which allow the vehicle to move relative to the bogeys and wheels. The primary suspension system is the system connected to the wheels and the bogey and the secondary suspension system connects the train body and the bogey, as shown in Figure 3.10. A dynamic model is typically required to model rail vehicle behaviour and allow for dynamic impacts that are created when the train vehicles cross over the transition in the railway.
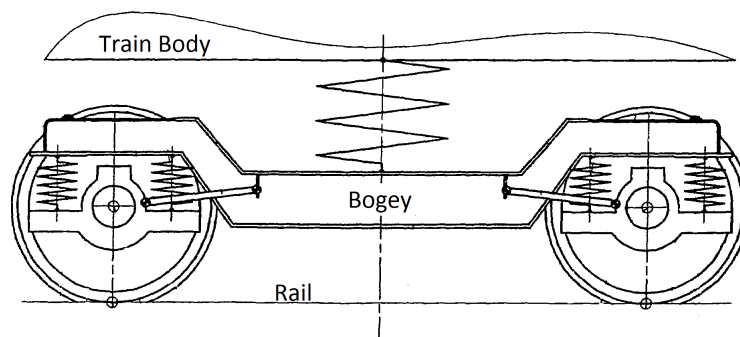


Figure 3.10: Train vehicle undercarriage [3].

Some studies model the dynamic interaction between the train and the supporting structure explicitly. This method, shown in Figure 3.11, allows for vertical acceleration of the train mass which creates dynamic impacts when travelling along the railway and when crossing a rail transition section. This method is more common where the system is modelled in a mechanical modelling package as used by, Antolin et al. [2] and Lei and Mao [30].

Lei and Mao [30] defined a vehicle model with ten degrees of freedom, these included seven vertical displacements and three pitch motions. The seven vertical displacements are that of the vehicle, the two bogies and the four wheels and the three pitch motions of the vehicle and the motions of the two bogies. Using a mechanical model of a vehicle with nodal loads and displacements defined as vector quantities with mass, stiffness and damping matrices deduced from the model the system equations can be solved for displacements, velocities and accelerations.

The model that Antolin et al. [2] used has 31 degrees of freedom for each train car. This is due to lateral displacements and rotations that are taken into account, but these are only needed when considering earthquakes or severe lateral winds, which are outside the scope of this study.

For the dynamic modelling of the railway track a similar approach to that of the rail vehicle was used. The rails are connected to the sleepers (modelled as point masses) by springs and dampers. The ballast mass is also simplified to a point mass and added to the sleeper mass, which is then connected to a rigid foundation with springs and dampers. The rail is modelled
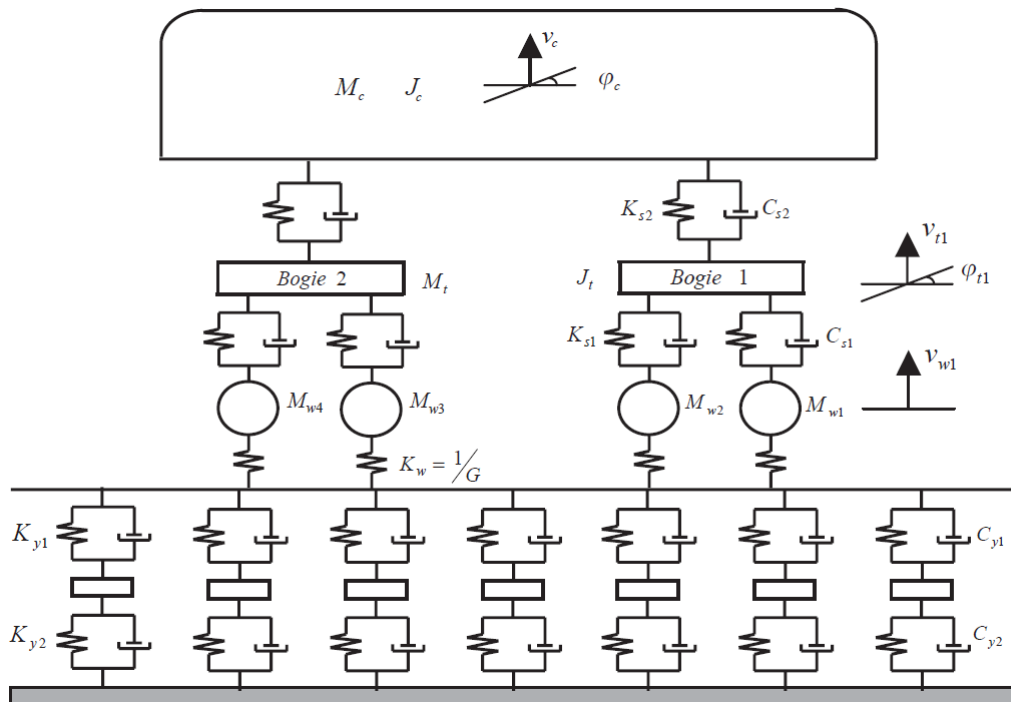
Figure 3.11: Explicit dynamic train vehicle and rail model [30].

as a two-dimensional beam element with end nodes at neighbouring sleepers and the foundation is treated as a double layer continuous elastic material [30].

By using a simplified beam element for the rail the global stiffness matrix can be reduced and the computational time decreased. This 2D beam element is allowed an extra degree of freedom for the vertical displacement of the ballast, the vertical displacement component of the ballast mass is added to the displacement of the beam node. This changes the two variables $(v_i, \theta_i)$ at each node to three variables $(v_i, \theta_i, v_i^*)$ per node. Loading between the element nodes is allowed for this element by extrapolating the load to the end nodes of the element within the load vector [30].

The railway track can also be analysed with a finite element dynamic equation as used for the rail vehicle. The two models for the vehicle and the track allow the separate analysis of the vehicle and track. These two models can then be linked through the use of different methods. The wheel-rail interaction model used by both Antolin et al. [2] and Lei and Mao [30] to link the two models is the Hertz contact model. To solve the non-linear models the Newmark method was used [30].

Lei and Mao's [30] study shows that the forces and accelerations created by an abrupt change in supporting structure stiffness are barely noticeable, especially at low speeds ($\approx 40\,\text{km/h}$) and the conclusion was made that it does not lead to an increase of the dynamic interaction forces between the rail and wheel directly. At a transition section between different rail structures an irregularity angle can occur, creating much higher impact loads, as seen in Figure 3.13. The irregularity angle occurs when there is a difference in elevation between different rail structures and it describes the angle of change in railway elevation between the different rail structures [30].

Figure 3.12 describes the irregularity angle.
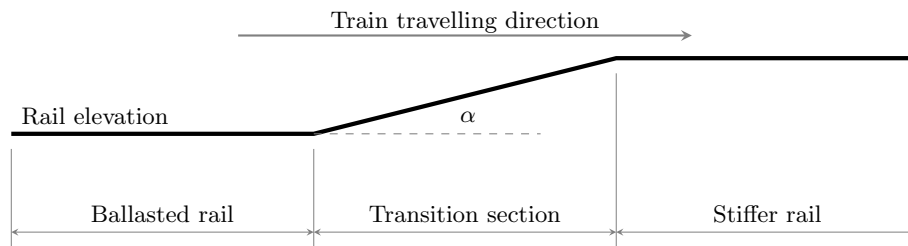


Figure 3.12: Rail transition section with an irregularity angle $\alpha$.

The low dynamic forces created in the system due to abrupt stiffness changes could, however, be enough to lead to an increase in the permanent settlement that is found in ballasted railway, which will create an even larger irregularity angle at a later stage in the lifespan of the rail line leading to higher forces in the rail structure than expected initially. If this occurs, abrupt changes in railway stiffness could pose a threat to the integrity of the structure at later stages in the life of the rail line. The results, shown in Figure 3.13, in Lei and Mao's [30] study supports the fact that low speed trains do not create significant forces at the rail transition.
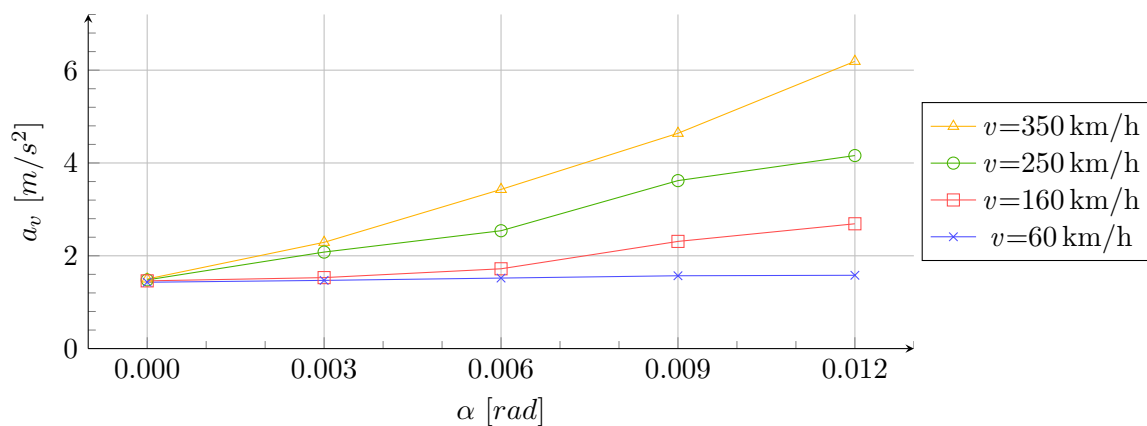


Figure 3.13: Increase in maximum vertical accelerations ($a_v$) of a rail vehicle for different train speeds ($v$) and rail irregularity angles ($\alpha$) [30].

In static loading the load stays constant over time while loading varies with time when a dynamic system is considered. System displacement, velocity and acceleration as well as mass, stiffness and damping need to be accounted for in this case. Using these system characteristics the natural vibration frequencies of the systems can be evaluated. When the dynamic load, which is applied to the structure, has the same frequency as the natural frequency of the structure resonance may occur [6].

To model the dynamic impact loads created by the high-speed train vehicles the static point loads of the train vehicles can be multiplied by the dynamic amplification factor (DAF) to achieve the higher forces that dynamic movement creates. Another approach of applying the train movement is to create multiple point loads on the rail which are loaded individually and consecutively with time increments between the point loads to simulate the train speed and wheel geometry [58]. A simpler approach is to model the wheels explicitly and apply

prescribed loads and displacements to the wheels to simulate the train speed and weight [35]. The approach of modelling the wheels explicitly is, however, only simpler when modelling in 2D since the geometry of a 3D wheel is and the contact interaction between the 3D rail and wheel is more complex. A method of determining the DAF for railway analysis is investigated in the following paragraphs.

There are several formulas which have been proposed to assess dynamic rail stresses. One of the simple formulas accepted by European railway companies was developed by Eisenmann [16] and it is dependent on the train speed, track quality and a chosen factor, $t$.

The DAF is calculated with the following equations [16]:

$$DAF = 1 + t\varphi \qquad if \qquad v < 60\,km/h \tag{3.29}$$

$$DAF = 1 + t\varphi(1 + \frac{v - 60}{140}) \qquad if \qquad 60 \le v \le 200\,km/h \tag{3.30}$$

where $\quad v \quad = \quad$ train speed [km/h]

$\qquad\qquad \varphi \quad = \quad$ track quality factor

$\qquad\qquad t \quad = \quad$ standard deviation multiplication factor dependant on the confidence interval

In Table 3.1 it is recommended that a value of 3 be used for $t$ since the rail is important for the safety and reliability of rail traffic. With a probability of 99.7 % the total area of exceedance is 0.3 %, above the upper bound and below the lower bound, leaving only a 0.15 % chance of exceeding the maximum stresses in the rail. Table 3.2 gives values of $\varphi$ which is based on the condition of the track under investigation.

Table 3.1: Choice of values for t [16].

| Probability | t | Application |
|---|---|---|
| 68.3 % | 1 | Contact stress, subgrade |
| 95.4 % | 2 | Lateral load, ballast bed |
| 99.7 % | 3 | Rail stresses, fastenings, supports |

Table 3.2: Choice of values for $\varphi$ [16].

| Track condition | $\varphi$ |
|---|---|
| Very good | 0.1 |
| Good | 0.2 |
| Bad | 0.3 |

Figures 3.14, 3.15 and 3.16 show a graphical representation of the two equations given above. The DAF is shown as a function of train speed for three track qualities and three probability levels.
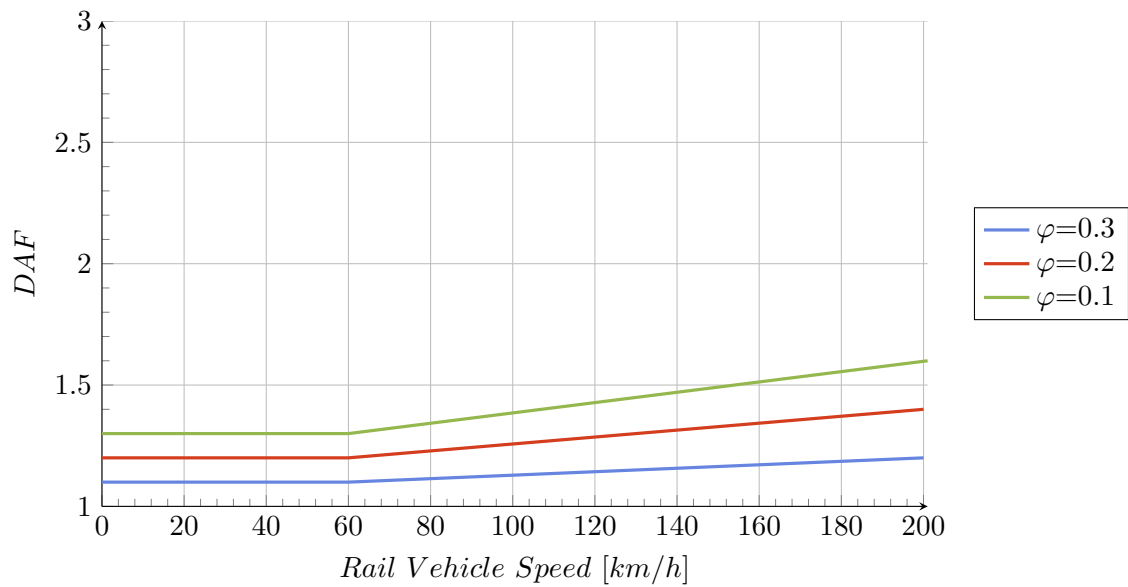
Figure 3.14: DAF as a function of speed for t=1 [16].
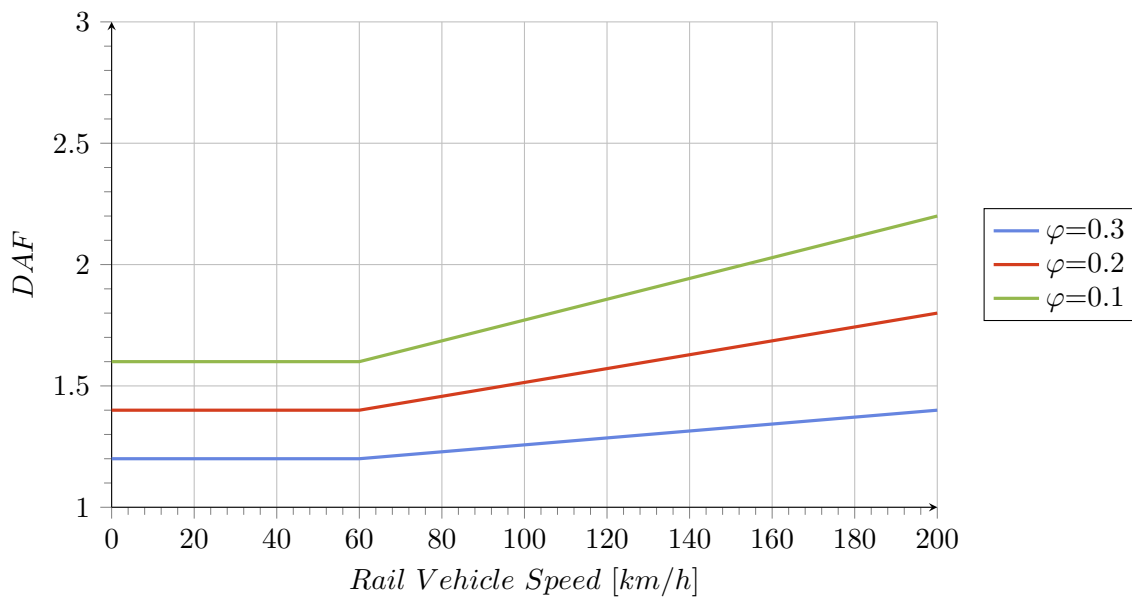


Figure 3.15: DAF as a function of speed for t=2 [16].
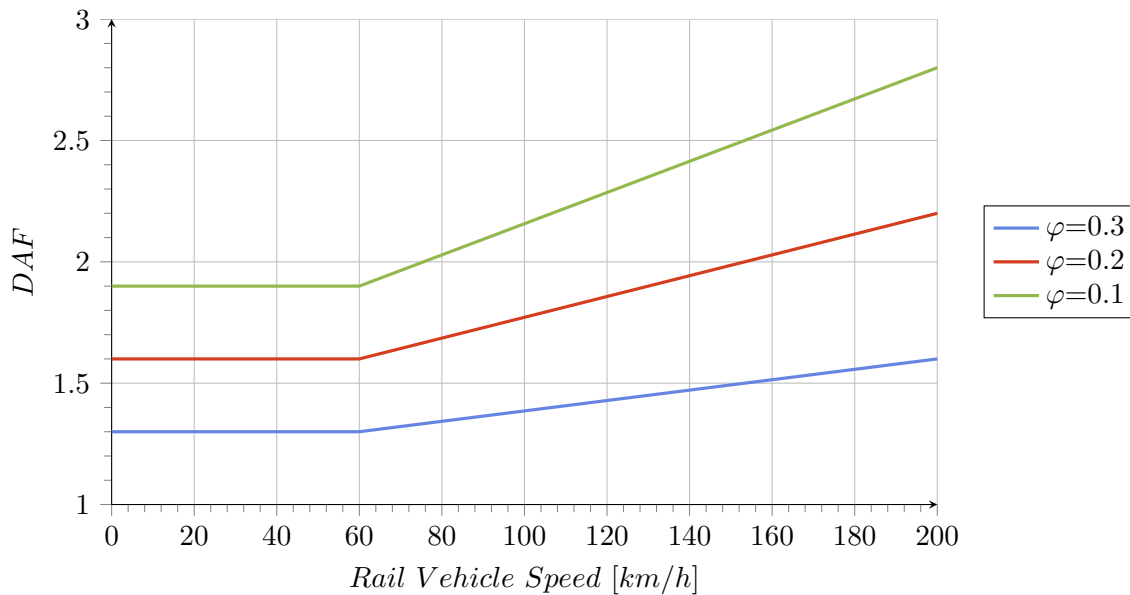
Figure 3.16: DAF as a function of speed for t=3 [16].

## 3.4   Discrete Element Method

DEM was first introduced by Cundall [11] to allow the study of two-dimensional slope stability problems in jointed rock masses. Unlike FEM, which models a fixed continuum, DEM can analyse the mechanical behaviour of a system consisting of a collection of particles, such as the ballast of a railway. It should be noted that the term, particle does not refer here to an infinitely small body, but rather a body that has finite dimensions.

Newton's laws of motion are applied to analyse these discrete systems through numerous iterative steps. The laws provide the relation between the movement of the particle and the forces acting on the particle. The system could either be in static equilibrium where there will be no movement of the particles or the forces and reactions acting on the particles could be such that the particles flow [26].

These particles are allowed to be in contact with each other exhibiting either rigid or deformable behaviour. Assuming that particles are rigid is a good assumption when the behaviour of the modelled physical system does not rely on the deformation of the particles themselves, but on the movement of the particles relative to one another and the forces occurring between them at contact points [27]. Precise modelling of particle deformation is not necessary to obtain good behavioural approximations of such systems [26]. The DEM model can be used as a validation tool for engineering ballasted track designs and addressing critical substructure concerns such as those related to variable track stiffness and track transition zones [56].

Lim and McDowell [31] used a box-test to do laboratory tests and the Particle Flow Code in 3 Dimensions (PFC$^{3D}$) software to do numerical tests on railway ballast. Examples are shown in Figure 3.17. The ballast particles in the box were modelled with uncrushable balls and clumps. Railway ballast is prone to crushing underneath the sleepers, these crushed particles

(a) Laboratory box-test.          (b) PFC$^{3D}$ model.          (c) Different particle shapes.
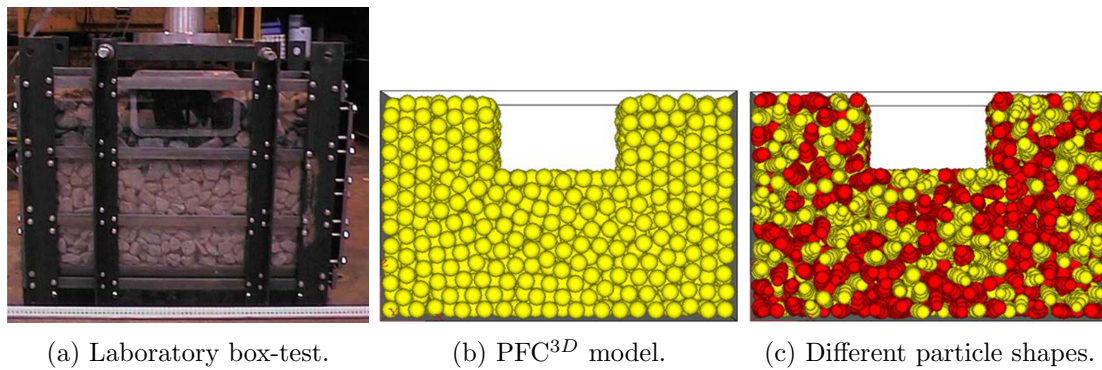
Figure 3.17: Box-test model [33].

increase the track deflection and contaminate the ballast which can affect the functionality of the ballast. The laboratory box-test of McDowell et al. [34] showed that the amount of crushed elements were very small and may justify the use of uncrushable particles. Lobo-Querrero and Vallejo [32] modelled particles that allowed crushing. Even though only a few particles were crushed directly under the sleepers the displacement was found to increase greatly. They highlight that modelling crushable elements is important. However, the modelling of crushable particles is typically computationally expensive [32] and Abaqus [12] does not yet allow the modelling of breakable bonds between particles; therefore, particle crushing is not modelled.

In Lim and McDowell's [31] numerical model, after a box has been created for the box-test and all particles settled to the required density the model was loaded with a repetitive sinusoidal load pulse. This test was done twice, once with spherical particles (Figure 3.17b) and another with 8-ball clumps (Figure 3.17c). The results showed that the clumps yielded a higher stiffness than the balls. The clumps had a higher resilient stiffness and less permanent deformation, which could be attributed to the additional resistance provided by the interlocking of the non-spherical clumps. It was found that the stiffness of the clumps and the balls were much higher than the stiffness of the laboratory ballast. Lim and McDowell [31] states that this is due to the contact between two particles being modelled by an elastic beam joining the centres of two balls. A Hertzian contact model is suggested to yield more realistic results. This will allow the contact forces to vary between the particles during analysis of the model [31].

Lu and McDowell [33] also made use of a box-test and studied the importance of modelling ballast particle shape in DEM. This seems to be important as Lim and McDowell [31] already noticed the difference in results between balls and clumps. The clumps used by Lu and McDowell [33] were defined to represent different shapes of ballast particles, one sample of modelled clumps is shown in Figure 3.18. Modelling with clumps yielded a hysteretic load-deformation response of the ballast which represents a more realistic behaviour. The displacement-force response of the clumps also shows a better representation of the reality and a better degree of homogeneity is achieved with the use of clumps. Lu and McDowell [33] suggest that clumps be used in the modelling of ballast to gain more realistic results.

Saussine et al. [41] created a symmetrical 2D model of the railway structure with a containing wall on one side of the model and the cross-section of the sleeper placed in the top of the ballast,
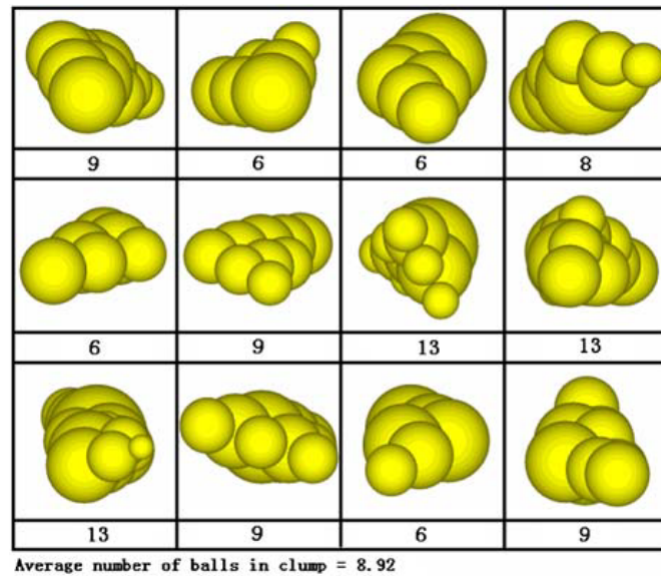
Figure 3.18: Various clumps used in the box-test [33].

this is shown in Figure 3.19. The software package used is called LMGC90 and allows the use of pentagonal particles for modelling the ballast. The study is done to study ballast behaviour under dynamic loading of 20 000 or more cycles. The available computational speed for this study allowed 1 000 cycles of loading in 24 h at a frequency of 20 Hz. This makes this method computationally expensive, but the results found in the test demonstrated the feasibility of modelling the ballast with DEM software to study the settlement of the ballast.
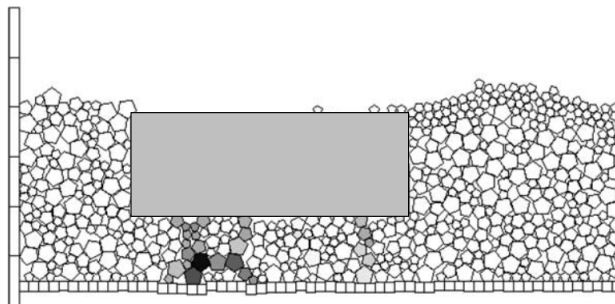


Figure 3.19: 2D DEM using pentagonal particle shapes [41].

### 3.4.1   Discrete Element Modelling using Abaqus

In Abaqus/Explicit (an explicit dynamics finite element program within Abaqus [12]) discrete particles are allowed to displace independent of one another and react with one another at contact points and interfaces. FE can also be incorporated into the model in order to contain the particles or to influence their movement and behaviour. Figure 3.20 shows an example where two types of particles are mixed by use of two FE augers.
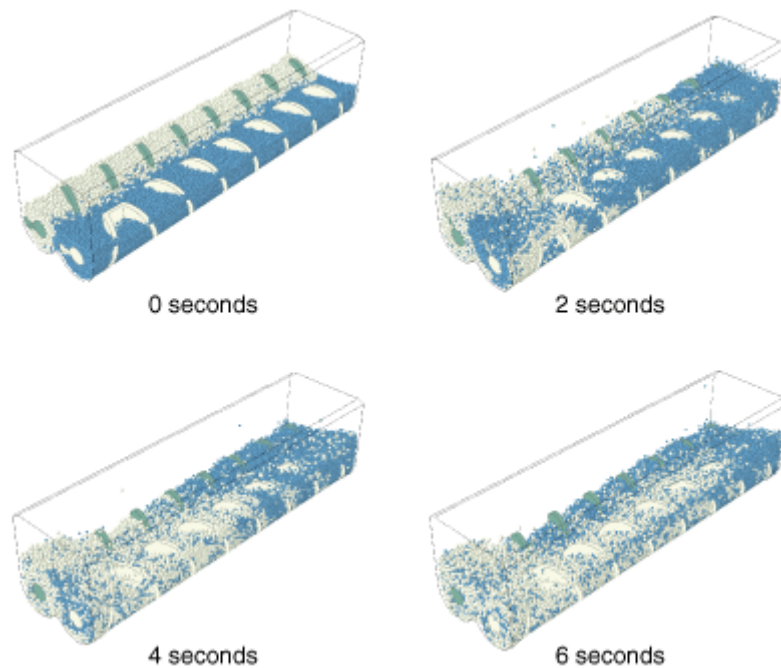
Figure 3.20: Example of particle mixing over time [12].

## DEM elements

In an Abaqus implementation of DEM all particles are modelled with single node elements called PD3D elements. The particle elements are rigid spheres having a given radii and rotational and translational degrees of freedom [12]. Figure 3.21 shows the degrees of freedom and variables of the particles interacting.

## Particle interaction

At the contact points between elements the interaction is modelled with springs, dampers and a friction surface (see Figure 3.21). These are used to model the behaviour of the interaction between neighbouring particles, but also play a big role in the global behaviour of the combined particles, like the stiffness of railway ballast for example. One particle is allowed to have multiple contacts as defined in Figure 3.21 with various particles.

This method of modelling the particle contact introduces some compliance into the particle system, removing complete rigid behaviour. The behaviour of compliant contact in Abaqus is shown in Figure 3.22. The figure on the left describes the case where the particles are just in contact and no contact force is transferred between the particles; the central figure shows a representation of the physical behaviour of particles where deformation occurs when forces are transferred through them; and the figure on the right shows the behaviour as modelled in Abaqus. Due to the particles being rigid they cannot deform and penetration is allowed to model the contact stiffness and deformation. The contact stiffness relationship between the particles is described by a force-penetration (F-$\delta$) relation and can be tuned to reflect the Hertz contact behaviour between particles, which is the preferred method for DEM modelling [12].

Legend:

| | |
|---|---|
| $u$, $\nu$, $\omega$ | = translational and rotational degrees of freedom per particle |
| R | = particle radius |
| $K_n$ | = normal contact direction spring stiffness |
| $C_n$ | = normal contact direction damping |
| $K_t$ | = tangential contact direction spring stiffness |
| $C_t$ | = tangential contact direction damping |
| $\mu$ | = friction coefficient between particles |
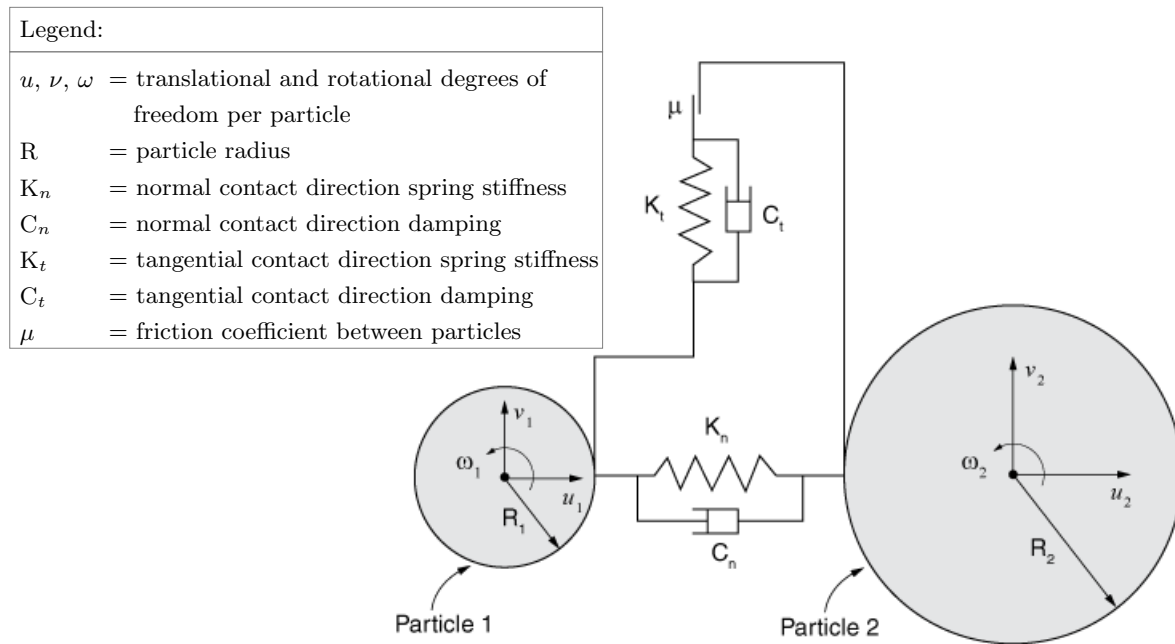
Figure 3.21: Contact interaction between two particles [12].
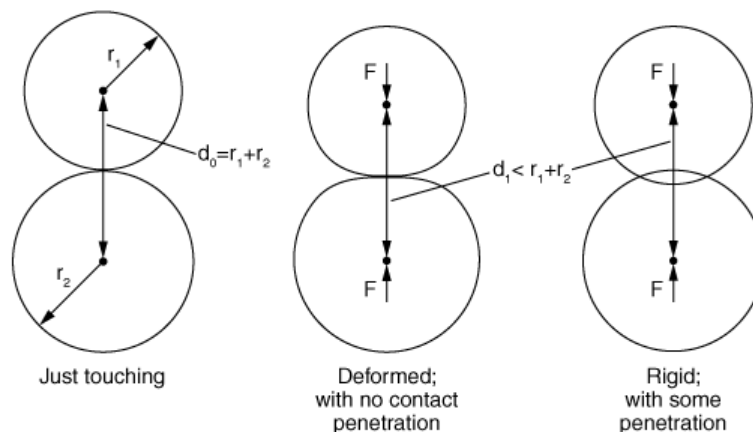


Figure 3.22: Particle contact modelling [12].

**Clumping**

The nodes of PD3D elements are allowed to be used in connector or constraint definitions. This allows the modelling of more complex shapes, other than spheres, by clumping the rigid spheres together as shown in Figure 3.18. To define these clumps the particles usually overlap each other and contact forces exist between the particles pushing the particles apart, unless contact exclusions are defined for the particles in a clump. When creating a particle with rigid connections between elements this is not a problem, but can be problematic when compliant connections are used.

Figure 3.23 shows an example of a clump and how it would be created in Abaqus. The clump may not represent the accurate shape of the ellipsoid as it is wished to, but this approximation gives more accurate results than the simple spherical shape would. A more accurate shape
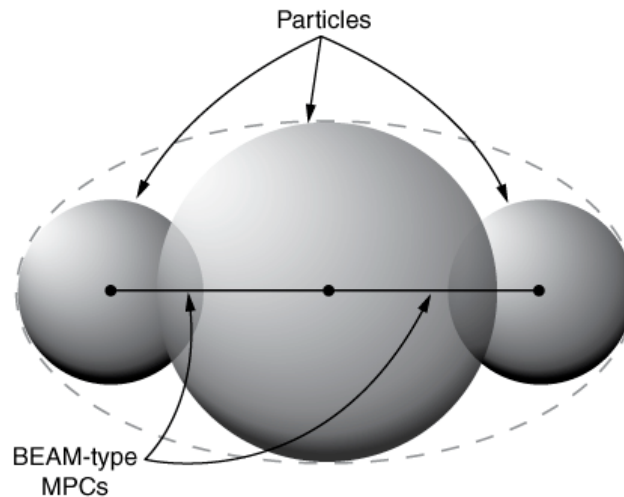
Figure 3.23: Rigid clump of particles [12].

can be created through the inclusion of more particles; however, this becomes a time expensive procedure and the amount of effort needed could exceed the advantages of modelling a precise shape.

## 3.5   Summary

Since modelling the train loads as point loads on the rail would result in high stress peaks at the contact between the train wheels and rail head the Hertz contact theory is used to provide a more realistic representation of the wheel-rail contact and prevents over- or under-estimation of forces in the rail. The contact area is modelled as an elliptical shape and the pressure distribution on this area represents a semi-ellipsoid. A Java application is available that predicts the contact area and the pressure distribution.

A method of simplifying the foundation supporting the rail structure was discussed. The elastic foundation theory simplifies the foundation to a set of springs with stiffness values representing the combined stiffness of the foundation formation layers. The PBT is a method of calculating the stiffness of the springs replacing the foundation. A PBT relates the pressure applied to the foundation by a rigid plate to the displacement of the plate, this relation is known as the modulus of subgrade reaction and is used to determine the spring stiffness.

Possible load combinations that could be applied to a railway structure were reviewed. These loads include static vertical, transverse and longitudinal loads. Only vertical loads are given due consideration since the assumption is made that no lateral or longitudinal forces will be apparent in the railway. The dynamic behaviour of trains was discussed, investigating possible methods of applying the dynamic loading behaviour of the rail vehicles to the rail structures. The method of using the DAF is suggested and methods of determining the DAF for specific cases was reviewed.

DEM is a useful modelling technique to model discrete particles which can act independent or

interact with each other, such as the ballast of a railway line. As a background into the use of DEM some previous research and the methods used therein was investigated. The contact behaviour between the particles and the methods used to model contact behaviour was explained as well as the method of creating clumped particles which can better represent the true shape and behaviour of the material. The Abaqus functionality for DEM was also reviewed.

# Chapter 4

# Research methodology

This chapter describes the research methodology followed to investigate the TMT and ballasted rail structures and the transition between them with the use of FEM and DEM models. The chapter presents the scope and limitations of the thesis as well as the analysis methodology used for the aforementioned models.

## 4.1   Scope of research

This study investigates the impacts of a moving load of 94 km/h on the displacements, bending moments and shear forces of a TMT structure and a ballasted rail structure and investigates different methods of analysing these structures. The study also investigates the sensitivity of the TMT structure RC beam to different variables at the transition from ballasted rail to TMT, which is the main objective of the study. The scope of the analysis methods performed in Abaqus to determine these impacts includes the following:

- TMT 2D and 3D finite element analysis (FEA)

- Ballasted rail 3D discrete element analysis (DEA) and 2D FEA

- Ballasted rail to TMT transition 2D model FEA

- Sensitivity analysis of TMT to rail transition

An in-depth investigation into the foundation of the railway systems is excluded from this thesis to allow more consideration for the modelling of the railway system itself. The foundation is, however, modelled according to a typical foundation suggested for a TMT system and should provide acceptable behaviour in the FEM model.

The purpose of this research is to investigate different methods of analysing the TMT, ballasted rail and ballast-TMT transition structures and determine the effects of the transition on the TMT structure. A simplified diagram of the process followed to investigate the transition structure is showed in Figure 4.1.

43
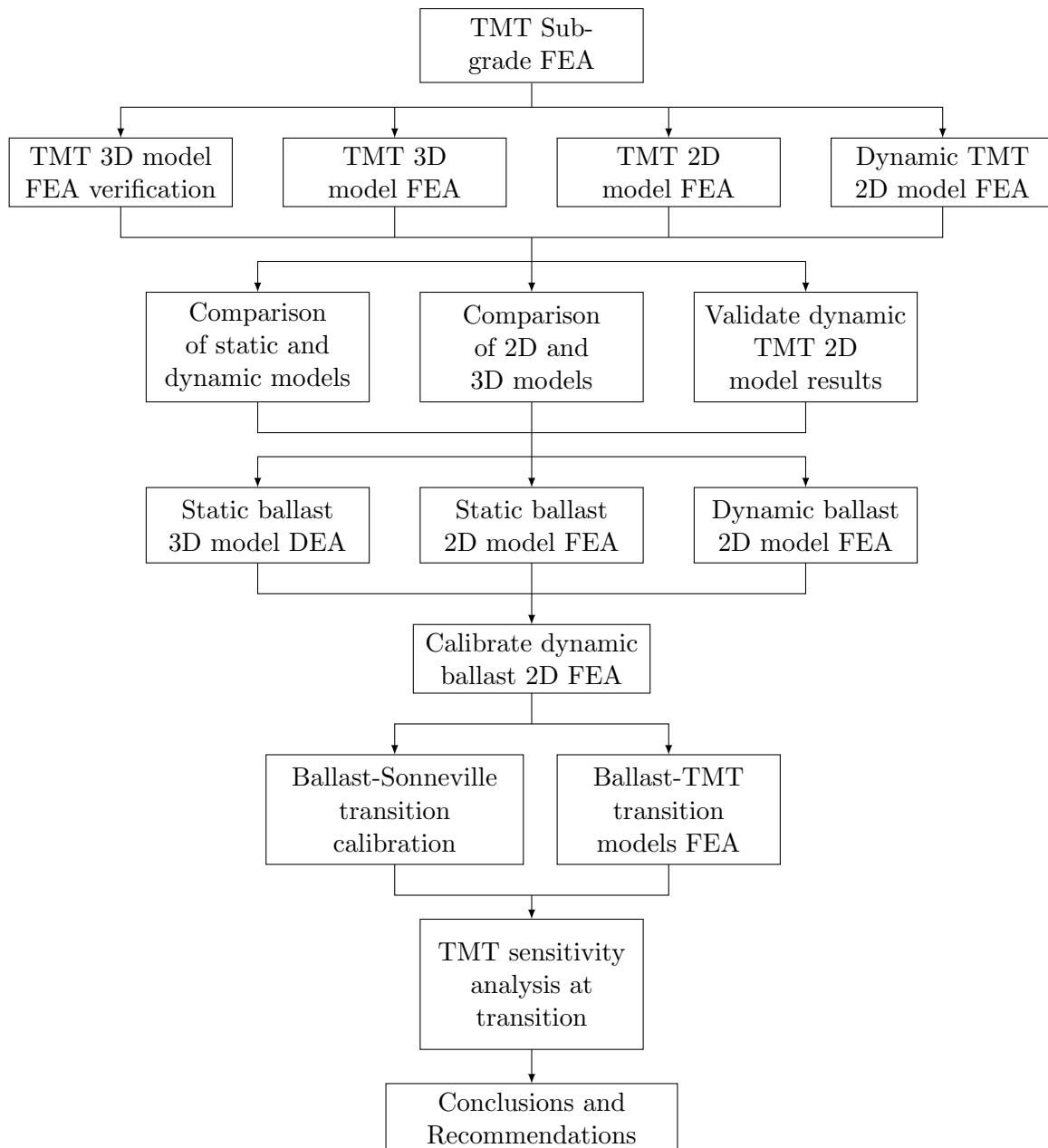
Figure 4.1: Investigation methodology for rail transition.

## 4.2   Methodology

This study makes use of previous research models, named reference models, to verify FEM models of the TMT subgrade and structure and uses reference measurements, performed on an existing rail line, to calibrate the FEM and DEM models created of the ballast and transition structures. Models by Verlinde [58] are used as reference models to verify the TMT and subgrade 3D models created in Chapter 5. A verification model is created in such a manner that its results resemble that of the reference model. After the verification model is verified by comparison to the reference model the analysis techniques are assumed as correct and the model is adapted to represent the parameters of this study; meaning, different train loads and speeds and different cross-sections of the rails and reinforced concrete (RC) beams are applied.

To calibrate the ballasted rail models site displacement measurements of a reference rail, which were performed by P.J. Gräbe of the University of Pretoria, are used. All measurements were performed for a train speed of 94 km/h and, therefore, all models created in this study are loaded with moving loads of 94 km/h. The results of the various models created for the ballasted rail are compared to the reference rail measurements. If the results compare to the reference measurements the models can be assumed to provide an adequate representation of the displacement behaviour of the ballasted rail system. No reference measurements are available for a ballast to TMT transition structure with the parameters of this study. To calibrate the methods used to create the 2D ballast to TMT transition model a different reference structure is used. Measurements, also performed by P.J. Gräbe, are available for a ballast to Sonneville track [47] transition and are used to calibrate a 2D model of a ballast to Sonneville track transition. With the transition calibrated the Sonneville track is replaced with the already verified TMT model to create the ballast to TMT transition model. Details of the ballasted and ballast-Sonneville transition reference rails used in this study are confidential and more detail than discussed here may not be provided.

Ballast is subjected to permanent settlement during initial load application cycles. Since this initial settlement occurs continuously over the whole railway it poses no threat to the integrity of the ballasted rail system, if further settlement occurs maintenance is required. When a transition between ballasted rail and ballastless rail is introduced the ballast settlement creates a difference in rail elevation between the two structures. This differential settlement should be considered during the analysis of the transition model, because of the higher stresses that occur in the structure due to the dynamic impact loads of the train vehicles passing over the irregularity. Initial settlement typically ranges between 5 mm and 15 mm depending on how many load cycles have already been applied; when last the ballast was tamped; and what type of traffic the rail has to support [22, 23, 34, 41, 56]. Compared to the settlement of ballasted rail, TMT exhibits a typical settlement of 3 mm [18].

In the TMT structure the steel reinforcement in the concrete and the PVC duct pipe (for placement of services) in the centre of the RC beam are excluded from the model. Including the details of the reinforcement and PVC duct pipe in the analyses of the track will lead to complex models, increasing the analysis time significantly [58]. The exclusion of the hole for

the PVC duct pipe will increase the strength of the beam marginally and negate some of the effects of excluding the steel reinforcement [58].

Since none of the lateral load cases are considered due to the wind action on and hunting of rail vehicles and the assumption that the transition is placed on a straight section of the rail line the gauge bars and rail fasteners will not be modelled. The scope of this thesis is contained to the structural response of the structure at the transition and does not include detailed modelling of independent components which do not contribute to the structural response. Excluding the gauge bars and rail fasteners will greatly simplify the TMT model and reduce the time and computational cost needed to analyse the structure. The restrictions imposed by the fasteners are however implemented in the contact definitions modelled between the rail and supporting structural elements.

Modelling the train wheel will make the FE model complex and modelling the wheel load as a point load will create an inaccurate representation of the contact between the wheel and the rail. The Hertz theory, discussed in the previous chapter, is used to estimate the contact area between the wheel and the rail so that a distributed pressure may be applied over the area. Since the analysis of the train components is outside the scope of this thesis the Hertz theory is deemed to be adequate to represent the wheel. In the 2D models the wheel is modelled as a circle and Hertz theory is not applied. The simplified shape of the 2D wheel makes modelling easier than for a 3D wheel and supports the use of a physically modelled wheel instead of using the Hertz contact theory and concentrated pressure loads — the 2D wheel automatically applies the wheel load as a pressure on the rail 2D beam elements.

After the ballast, TMT and transition models have been created, analysed and verified a sensitivity analysis is done for the TMT structure. The RC beam is the main component of the TMT structure and is the least researched component for rail transitions, much of research focusses on the behaviour of the rail, ballast and sleepers or other support type structures at a transition. For this reason the sensitivity analysis focusses on the displacements, shear forces and bending moments of the RC beam. The sensitivity analysis gives insight into the behaviour of the TMT structure, with focus on the RC beam, and suggests limits to train speeds and rail irregularity angles.

## 4.3   Limitations

The following assumptions are made and limitations apply for the various analyses of this study:

- The results investigated for the various models are limited to the displacements, shear forces and bending moments of the individual components and shock loading results, such as velocity and acceleration, are not presented.

- This study only performs the analyses of the ballasted structure, TMT structure and transition structure, and does not focus on specific design of any of the structures.

- No ballast disintegration (crushing) or particle clumping (grouping of particles to create a shape other than a sphere) is modelled. This allows a decrease in the computational time of the analyses and reduces the complexity of the model. Modelling particle clumping is a very involved procedure and breakable bonds, which are required for modelling crushing, are not available in Abaqus.

- Ballast settlement has a minimal effect on rail behaviour for ballasted rail alone, but does have an effect at a transition where it creates an irregularity angle. The vertical rail geometry of the reference transition structure is used in the verification transition model to include the effects of permanent ballast settlement.

- In the ballast to TMT transition model the vertical rail geometry changes linearly over the length of the transition zone from the settled, ballasted rail to the TMT rail.

- For a transition with no varying vertical geometry the difference in supporting structure stiffness has minimal effect on the behaviour of the rail — the transition zone will not have an adapted stiffness, but will have the same stiffness as the ballasted rail.

- The transition is modelled as a straight rail section, because it is assumed poor design practice to place a transition in a curve where the stability of the train can be disrupted by the sudden change in rail stiffness or rail settlement.

- Without transverse forces that arise when a train negotiates a horizontally curved section of track the loading in the structure is symmetrical and only half of the structure needs to be modelled, with the correct symmetry boundary conditions applied. This symmetry is applied to all models created in this study.

- Only vertical loads are applied due to the assumption of symmetry along the centreline of the rail and rail vehicle induced actions due to wind, earthquakes, braking and acceleration forces will not be considered.

- Fatigue behaviour at the transition is not investigated in this study.

- The mass of the train vehicles and participating soil and ballast masses are not included in the models investigated in this study. These are both very difficult to include due to the sprung nature of the train vehicles and the semi-infinite nature of the soil.

- The specific transition zone design cannot be specified, since any transition zone model would merely be a speculative design because it has not been verified. However, suggestions can be made for train speed and maximum irregularity angle and the behaviour of the rail structure under various loading conditions can be predicted.

# Chapter 5

# Tubular Modular Track Finite Element Analysis

This chapter discusses the analyses of the:

- 3D supporting subgrade,

- static 3D TMT structure,

- static 2D TMT structure and

- dynamic 2D TMT structure.

To allow accurate modelling of the TMT structure and subgrade different element types available are investigated. The investigated linear and quadratic element types are:

- Hexahedral

- Tetrahedral

- Wedge

- Beam

- Bilinear and biquadratic plane stress

The application of these elements in the TMT model are discussed and thereafter the mesh sensitivity of the 2D model is evaluated. In order for the model of the TMT structure to function properly there has to be accurate modelling of the contact behaviour between the separate components. Contact methods and contact properties are investigated to ensure accurate contact modelling. The supporting subgrade is an integral part of the TMT structure. To define the subgrade characteristics PBT analyses are performed to obtain the modulus of subgrade reaction. The modulus of subgrade reaction is used to apply the stiffness of the elastic foundation to the TMT model with the elastic foundation option.

The models which are created are described in terms of

- components,

- geometry,

- boundary conditions,

- load applications,

- type of analysis performed and

- the results obtained.

For the static 2D and 3D and the dynamic 2D models the following results are discussed:

- Modal response

- Displacements

- Dynamic amplification factor

- Shear forces

- Bending moments

## 5.1   FEM Elements

This section discusses the different finite element types available in Abaqus for modelling the TMT structure.  Continuum 3D finite elements used for modelling the TMT structure are hexahedral, tetrahedral and wedge elements. Following the investigation of the different element types available for modelling the TMT 3D model the beam and plane stress structural finite element types used to create the TMT 2D model are investigated.  The application of these elements are then discussed.

**Hexahedral Elements**



(a) Linear brick.          (b) Quadratic brick.
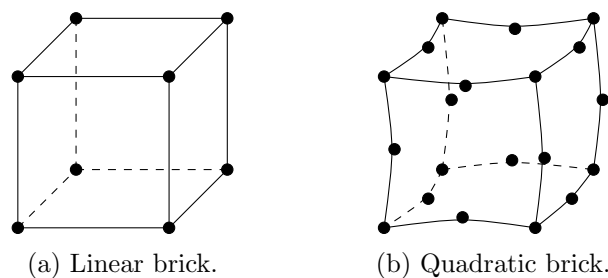
Figure 5.1: 3D solid hexahedral elements.

Hexahedra are commonly used in the modelling of simple 3D shapes. Linear displacement interpolation based hexahedral elements, Figure 5.1a, have eight nodes with a node on each corner of the element and make use of linear interpolation over the volume of the element. The single-point integration scheme is used for linear reduced integration hexahedra and is based on the "uniform strain formulation" where the strains are not obtained at the first-order Gauss point but are obtained as an average strain over the element volume. A flaw of this element is that shear locking occurs when bending is applied to the element. To overcome this flaw a quadratic hexahedral element is provided. The quadratic displacement interpolation based element, shown in Figure 5.1b, has 20 nodes with a node on each corner and nodes on the edges between corners and makes use of the "serendipity" interpolation method [12] and the Gauss integration scheme is always used for quadratic hexahedral elements. Hexahedral elements have a better convergence rate than wedges and tetrahedra, but unlike wedges and tetrahedra the element shape regularity is important for accuracy [12].

**Tetrahedral Elements**



(a) Linear tetrahedron.          (b) Quadratic tetrahedron.
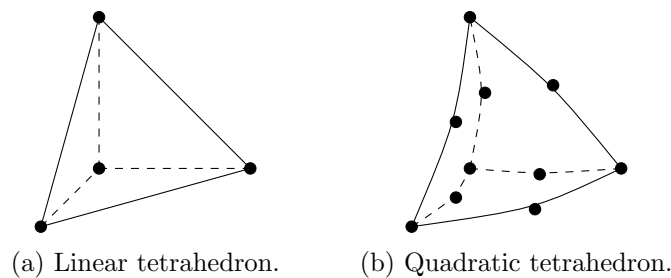
Figure 5.2: 3D solid tetrahedral elements.

Tetrahedral elements are used to model complex shapes, such as the rail, which cannot be accurately meshed by simpler elements. The linear tetrahedral element in Figure 5.2a has four nodes, one on each corner, and uses linear interpolation across the volume of the element. The linear elements are constant stress elements using only one integration point. Linear tetrahedra are not accurate for stress and displacement analyses. Quadratic tetrahedral elements shown in Figure 5.2b have ten nodes placed on the corners and edges of the element and use quadratic interpolation [12]. The numerical integration scheme used for quadratic tetrahedral elements is available in Stroud [50].

**Wedge Elements**

The wedge elements in Figure 5.3 are similar to tetrahedral elements in terms of interpolation and integration methods, but have different shapes. The linear wedge, Figure 5.3a, has six nodes with a node on each corner and two integration points for the stiffness matrix. The quadratic wedge in Figure 5.3b has fifteen nodes with nodes on the corners and edges between corners [12]. The integration scheme of the quadratic wedge is discussed in Stroud [50]. Wedges are useful when modelling a shape with a complex cross-section, but a uniform shape out of the

(a) Linear wedge.              (b) Quadratic wedge.
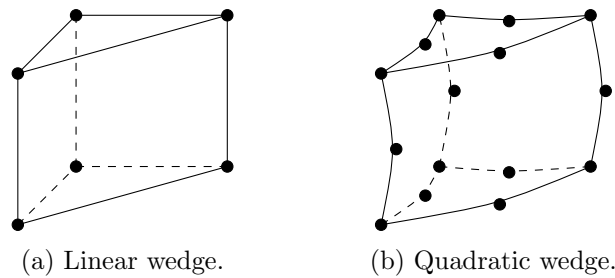
Figure 5.3: 3D solid wedge elements.

section plane, such as the RC beam.

**Beam Elements**

When 3D objects become very slender they can be approximated by beam elements. These beam elements are represented by lines in a 3D space or in a 2D X-Y plane and the stiffness of the physical 3D beam is assigned to the deformation of the line. The deformation of the line allows axial stretch, bending and torsion (in space only). The elements can either be linear, quadratic or cubic elements. Cubic, 2-node elements represent the Euler beam theory while linear 2-node and quadratic 3-node elements represent the Timoshenko beam theory. Beam elements use three Gauss points for integration [12].

**Plane Stress Elements**



(a) Bilinear quadrilateral.     (b) Biquadratic quadrilateral.
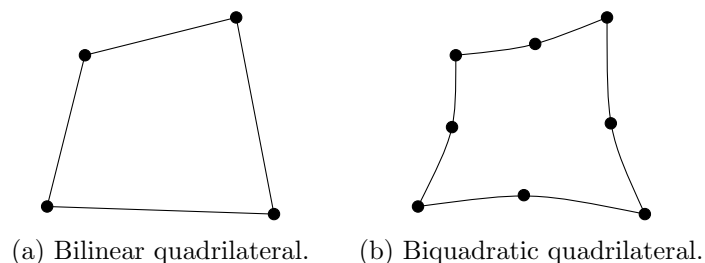
Figure 5.4: 2D plane stress quadrilateral elements.

The plane stress approach is generally applied to thin, flat bodies where the body is not thick enough to constrain its own strains in the thickness direction. With the plane stress assumption the normal and shear stresses in the out-of-plane direction are equal to zero and strains are allowed in the same direction, which allows the material to deform in the thickness direction [12]. During meshing the elements can be defined as either linear or quadratic quadrilateral elements with options for reduced integration and incompatible modes. The linear element has four integration points and the quadratic element has nine integration points. The linear and quadratic elements are shown in Figures 5.4a and 5.4b [12].

**Rail Element Type**

The elements used in the TMT 3D model rail are modified, tetrahedral elements which are quadratic displacement interpolation based. Tetrahedral elements allow meshing of the complex shape of the rail and the wheel-rail contact points. Quadratic elements are used since linear elements show overly stiff results and need extremely fine meshes. Modified elements work well in contact analyses and show minimal shear and volumetric locking.

Shear forces play a significant role in the behaviour of the TMT rail. To accommodate the shear forces in the 2D TMT model the Timoshenko beam theory, which allows transverse shear strain, needs to be applied to the beam elements. To implement the Timoshenko beam theory three-noded, quadratic elements are used.

**Elastomeric Pad Element Type**

The elastomeric pad element type for this study is a linear displacement interpolation based hexahedral element. Hexahedral elements can mesh the simple shape of the pad easily and linear hexahedral elements have constant volumetric strain over the element which prevents mesh locking when the material response is nearly incompressible. Hourglass control is applied to the elements to avoid hourglassing. Hourglassing is a problem which can occur with first-order, reduced integration elements in stress/displacement analyses — elements with only one integration point. Hourglass modes are non-physical response modes where the elements distort in such a way that the calculated strains at the integration point are all zero, leading to a distortion of the element that can become excessive unless the hourglass modes are properly controlled. Reduced integration is applied to prevent shear and volumetric locking which causes the elements to be too stiff. Even though the elements include hourglass control the mesh should still be reasonably fine to prevent hourglassing from occurring.

In the 2D model the elastomeric pad is modelled as a plane stress component, because using spring elements, as in the double beam theory in Chapter 3, will accurately model the stiffness and compression of the pad, but the shear force distribution is not accurate in the RC beam. This is due to the springs transferring loads from the rail to the RC beam as point loads rather than the distributed force which the elastomeric pad should provide. The plane stress elements are bilinear quadrilateral elements with incompatible modes applied.

**RC Beam and Grout Element Type**

The grout and RC beam element type is a hexahedral element which uses a linear displacement interpolation scheme with incompatible modes selected. Hexahedral elements mesh the shapes of the grout and the RC beam with a simplified cross-section easily. Incompatible modes enhance the linear elements to improve their bending behaviour; its primary effect is to eliminate parasitic shear which makes the linear elements too stiff. Parasitic shear is seen in fully integrated elements that are subjected to bending. The numerical formulation of the element creates shear

strains that do not exist (parasitic shear) which causes the element to be too stiff in bending. Incompatible mode elements are more expensive than the linear elements, but are significantly more economical than quadratic elements. Full integration is used so there are no hourglass modes. If the elements are near rectangular they perform almost as well as quadratic elements, but if the shape is a parallelogram the performance is reduced considerably.

In the 2D model of the TMT structure the RC beam is modelled with linear beam elements. The grout has bilinear quadrilateral elements and is modelled as a plane stress element even though a beam element approach would also be viable. This is because the elastic foundation function in Abaqus cannot be applied to beam elements, but can be applied to plane stress elements. The elastic foundation is applied to the bottom edge of the grout with a force per area stiffness value.

### Foundation Element Type

The foundation analysis uses hexahedral shape elements which easily mesh the simple shape of the square foundation sample created for the PBT analyses. These elements are defined as linear elements, since only small displacements need to be considered and no significant bending of the elements occurs it is not necessary for quadratic elements. The reference model by Verlinde [58] makes use of reduced integration which leads to some degree of hourglassing. To avoid the problem of hourglassing reduced integration can be switched off, but this creates the problem of mesh locking which may overestimate the stiffness of the foundation. The analysis is performed with reduced integration and without reduced integration to compare with the reference model.

### Mesh Sensitivity

The mesh sensitivity of the 2D TMT model, discussed later in Section 5.4.4, is investigated to determine the most effective mesh size with regard to analysis time and accuracy of results. Considerations for meshing are the aspect ratio of the 2D plane strain elements and the length of the 1D beam elements. The 2D elements should typically not have an aspect ratio greater than 1:5. The elastomeric pad with a thickness of 5 mm can therefore not have a mesh with an element size larger than 25 mm. Bending moments and flexural stress results for beams with distributed loads become more accurate as the beam element size decreases [12]. When multiple verification analyses are performed on, for example, a cantilever beam with decreasing element sizes the analysis results converge to a certain value. The element size where the results stop showing significant change is the element size which should be used, further mesh refinement will be unnecessary. A mesh sensitivity analysis was performed to determine at what element size the results would converge to a certain value.

Table 5.1 below contains the results for different analyses performed on the static TMT model with mesh sizes ranging from 5 mm to 50 mm. The results include vertical displacements, shear forces and bending moments. The elapsed application program runtime for the computation of each model is also included to allow a comparison between analysis time and result accuracy.

From the results in Table 5.1 it is seen that the displacements, shear forces and bending moments of the rail and RC beam, except for rail shear forces, are not sensitive to the mesh size within the range of mesh sizes chosen. Shear forces in the rail converge for mesh sizes 25 mm and smaller while all other results remain similar for different mesh sizes. The comparison of runtime shows an exponential increase in analysis time, which makes unnecessary small mesh sizes uneconomical. A mesh size of 25 mm will be used for further analyses performed on the TMT structure.

Table 5.1: Mesh sensitivity analysis results.

| Mesh Size | Runtime | Rail | | | RC Beam | | |
|---|---|---|---|---|---|---|---|
| | | $w$ | Bending Moment | Shear Force | $w$ | Bending Moment | Shear Force |
| [mm] | [s] | [mm] | [kN.m] | [kN] | [mm] | [kN.m] | [kN] |
| 50 | 4.4 | 0.6612 | 7.15 | 35.35 | 0.6225 | 11.38 | 22.33 |
| 25 | 15.4 | 0.6616 | 7.08 | 42.40 | 0.6226 | 11.37 | 22.29 |
| 10 | 32.3 | 0.6619 | 7.32 | 42.04 | 0.6224 | 11.35 | 22.26 |
| 5 | 91.5 | 0.6617 | 7.30 | 43.77 | 0.6221 | 11.35 | 22.26 |

## 5.2  Interaction and Contact Modelling

Contact interactions are defined in Abaqus by selecting contact surface pairs or with general contact between all surfaces. These contact interactions can be assigned contact properties. By default the contact property does not allow penetration of components in contact. Abaqus allows modelling of the contact between components with normal and tangential contact behaviour. Modelling of the interaction between components is important in order to achieve accurate results. Incorrect modelling of the contact between the components could create a system which acts too stiff or not stiff enough.

Contact between the TMT components is defined as hard contact, allowing no penetration between the elements in contact and no separation of components is allowed after contact has been initiated. Because the rail clip fasteners prevent the rail, elastomeric pad and RC beam from separating and the contact between the RC beam and grout does not allow separation the model does not need to allow separation. In the 2D models the contact incorporates the height of the beam elements and the resulting eccentricities between the centroidal axes of the beams and other elements. These eccentricities can be seen in Figure 5.18. The tangential interaction between surfaces is applied with the penalty method, which applies a friction coefficient to the interaction between two surfaces. The friction coefficients between components has been taken from Verlinde [58] and are shown in Table 5.2.

Instead of modelling the subgrade as a continuum, contact interaction between its layers needs to be considered for more accurate modelling of the compression behaviour of the subgrade. Modelling the subgrade with several layers will give a less stiff, more conservative (with regard to displacements) value for the modulus of subgrade reaction. The normal contact behaviour between the layers has a hard contact definition which does not allow any penetration between

Table 5.2: Coefficient of friction values between components [58].

| Interaction | Friction coefficient |
|---|---|
| Rail-Pad | 0.6 |
| Pad-Beam | 0.6 |
| Beam-Grout | 0.6 |

the layers. The tangential contact behaviour uses the penalty friction formulation which makes use of a basic Coulomb friction model where the friction coefficient remains constant over the entire period of contact. It is difficult to determine an accurate value for the friction coefficient between the soil layers; therefore, a general friction value of 0.6 is used [1]. The small vertical displacement results obtained from the analysis results indicates that the model is not sensitive to friction between layers, which permits the use of a general friction formulation [58].

## 5.3   Supporting Subgrade

The supporting subgrade is an integral part of the TMT structure. To define its characteristics accurately a finite element PBT analysis is performed in order to obtain the modulus of subgrade reaction. Explicitly modelling the subgrade layers in the analysis of the whole rail structure will increase the computation time and complexity of the model. Using the modulus of subgrade reaction allows the calculation of a stiffness for the elastic foundation option of Abaqus which supports the TMT model components during the analysis. This section describes:

- how the modulus of subgrade reaction is calculated with the PBT;

- the comparison between the reference subgrade model and the verification subgrade model; and

- the analysis used for the calculation of the modulus of subgrade reaction for this study.

### 5.3.1   Plate Bearing Test

The PBT, as described in Chapter 3, is required to simplify the modelling of the TMT subgrade in an accurate manner. With the use of this test Hooke's law can be applied to relate the displacements of the foundation to the pressure applied to the $600\,\text{mm} \times 600\,\text{mm}$ plate. This is known as the modulus of subgrade reaction and is defined as,

$$k_1 = \frac{p}{w} \tag{5.1}$$

where  $k_1$  =  modulus of subgrade reaction for a square PBT, which has a unit
of pressure per unit of displacement [N/mm$^3$]

$p$  =  ground bearing pressure at a point below the plate [N/mm$^2$]

$w$  =  vertical displacement at the same point [mm]

PBTs are usually done in-situ, but can also be done with a FEM model. When modelling a PBT with a FEM package it is good practice to compare the results with in-situ tests to verify whether the model is created correctly. Verlinde [58] created two models, namely a square PBT and a rectangular PBT and compared the results to known values of in-situ foundations. To verify the results of the PBT for this study the PBT results obtained by Verlinde [58] are used as reference and a verification model is created in such a way that results similar to the reference results are achieved. If the results of the verification model, which copies Verlinde's [58] model, agree with the reference model results, Verlinde's model results, the verification model is assumed accurate and the same technique is used to model the PBT for this study.

### 5.3.2   Reference Model

The reference subgrade model, created by Verlinde [58], is decribed here. The reference subgrade model layer properties used to create the verification model, are shown in Table 5.3.

Table 5.3: Reference subgrade layer properties [58].

| Material | Young's Modulus [MPa] | Poisson's ratio - | Density [kg/$m^3$] | Stratum Thickness [mm] |
|---|---|---|---|---|
| Top crusher run | 220 | 0.3 | 2 200 | 200 |
| Bottom crusher run | 141 | 0.3 | 2 100 | 200 |
| Rock fill | 200 | 0.3 | 2 300 | 900 |
| Clay | 38 | 0.35 | 1 700 | 420 |
| In-situ Norite | 1 000 | 0.25 | 2 500 | semi-infinite |

**Square PBT reference model results**

In the square PBT reference model the boundaries of the subgrade, which are $3\,000\,\text{mm} \times 3\,000\,\text{mm}$ in plan, are restrained in their respective normal directions and the $600\,\text{mm} \times 600\,\text{mm}$ loaded area is defined as a rigid surface simulating the stiff plate used in the PBT. In literature [8] a plate size of at least 300 mm is suggested and it is mentioned that it is difficult to maintain rigidity for larger plates. The 600 mm size plate size used in this study is used to activate the weaker sub-strata, for a smaller plate size only the stronger top subgrade layers will support the plate load, leading to a higher assumed subgrade stiffness. By applying a pressure to the surface of the plate that yields a unit displacement of 1 mm, Hooke's law yields a modulus of subgrade reaction, $k_1 = 0.345\,\text{N/mm}^3$.

**Rectangular PBT reference model results**

The rectangular PBT is similar to the square PBT, except for the length of the model which is defined by the characteristic length of the beam. The characteristic length is a section of an infinitely long beam which is affected by an applied point load. The width of the loaded area is 600 mm. The boundary conditions remain the same as for the square PBT model and

the loaded area is still a rigid surface, but the load stretches the whole length of the model. The same method of loading as used for the square PBT is used for the rectangular PBT. The calculated modulus of subgrade reaction for a rectangular PBT with a characteristic length is, $k_s = 0.169 \, \text{N/mm}^3$.

After Verlinde [58] had obtained the square and rectangular PBT results for different subgrade sections investigated, the $k_1$ and $k_s$ values were compared to define an equation for the relation between them. The relation is:

$$k_s = 0.5 \times k_1 \tag{5.2}$$

Since this relation will give a lower estimation of the foundation stiffness, as proposed by Equations 3.21 and 3.22, this equation is used to provide more conservative (with regard to displacements) and realistic values for $k_s$.

### 5.3.3 Verification Model

A good correlation between the modulus of subgrade reaction of the reference model and the verification model will allow the adoption of assumptions made and methods used to create the verification model. The verification model can then be adapted to create a similar model for the subgrade used in this study. The comparison between the reference results and the verification model results is shown in Table 5.4.

Taking some modelling differences into account the errors between the values for the modulus of subgrade reaction for the reference model and the verification model (with reduced integration) are small. This allows the assumption that the same methods used to create the verification model can be used to create the subgrade model for this study.

Table 5.4: Modulus of subgrade reaction comparison.

| | Square PBT, $k_1$ [N/mm$^3$] | Rectangular PBT, $k_s$ [N/mm$^3$] |
|---|---|---|
| Reference model | 0.345 | 0.169 |
| Verification model | 0.369 | 0.185 |
| Error | 6.9 % | 8.64 % |
| Verification model* | 0.342 | 0.171 |
| Error | -0.87 % | 1.18 % |

*Reduced integration applied

### 5.3.4 Supporting Subgrade Analysis and Results

The PBT model created for the analysis of the subgrade in this study can be seen in Figure 5.5. All modelling methods are the same as described above for the reference and verification models to ensure a similar model and accurate results. The only difference between the models are the different material properties and layer thicknesses, as shown in Table 5.5.

The vertical displacement results of the square PBT analysis is shown in Figure 5.6a together with the vertical stress results in Figure 5.6b. The square PBT analysis yields a $k_1$ value of $0.2086 \, \text{N/mm}^3$. When substituting this into Equation 5.2 the $k_s$ value for the foundation is $0.1043 \, \text{N/mm}^3$. The value of $k_s$ will be used in the TMT model as well as following ballasted and transition models for the application of the elastic foundation contact option.
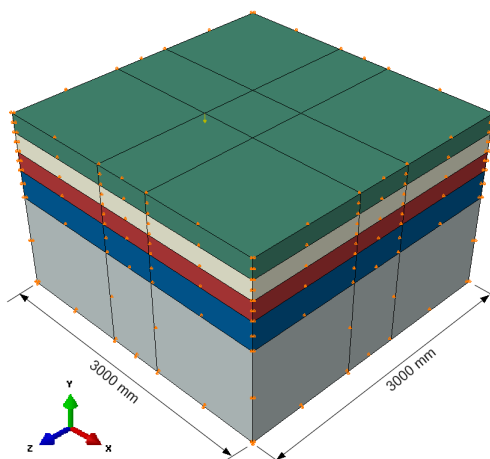


Figure 5.5: Square PBT model.
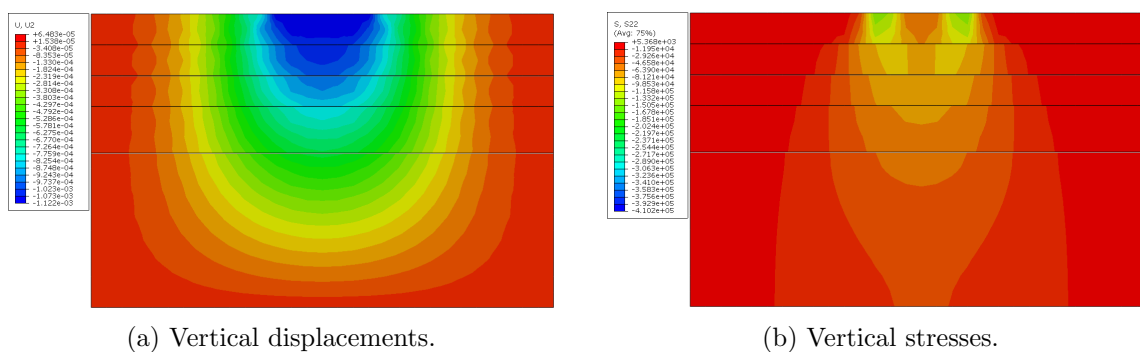


(a) Vertical displacements.

(b) Vertical stresses.

Figure 5.6: Square PBT analysis results.

Table 5.5: Subgrade model material properties [45].

| Layer | Young's modulus [MPa] | Poisson's ratio [-] | Density [kg/m³] | Layer thickness [mm] |
|---|---|---|---|---|
| SSB | 250 | 0.3 | 2 100 | 200 |
| SB | 180 | 0.3 | 2 000 | 200 |
| A | 110 | 0.3 | 1 900 | 200 |
| B | 80 | 0.3 | 1 800 | 300 |
| In-situ | 60 | 0.3 | 1 700 | semi-infinite |

## 5.4 TMT Static Analysis

This section contains a similar approach to the previous section which verified and analysed the subgrade. A TMT reference model, created by [58], is replicated in this study by a TMT

verification model with the aim to achieve similar results between the two models. If the models show similar results the methods used to create the verification model are assumed as accurate and are adopted for the TMT model of this study. A 3D model of the TMT structure is created for this study with the verified methods and the results of the model analysis are discussed. To decrease the computational time of the TMT structure the model is simplified to a 2D model in following analyses. The results of the 2D model are discussed and compared to the 3D model.

### 5.4.1   Verification 3D Model

The verification model replicates the reference model (the TMT model created by Verlinde [58]) and verifies modelling techniques such as meshing, loading, boundary conditions and contact used as well as the simplified geometry used for the rail and RC beam profiles. The simplified model geometry allows easier meshing with larger elements, reducing computational cost and allowing easier extraction of results. All TMT models created in this study are assumed to have a continuous length. In actual fact, the beams consist of 5.9 m pre-cast elements. Including the discontinuity in the beams would lead to some localised deflections in the rail. This could be considered in future research. The verification model is set up according to the train load geometry used in the reference model as shown in Figure 5.7.
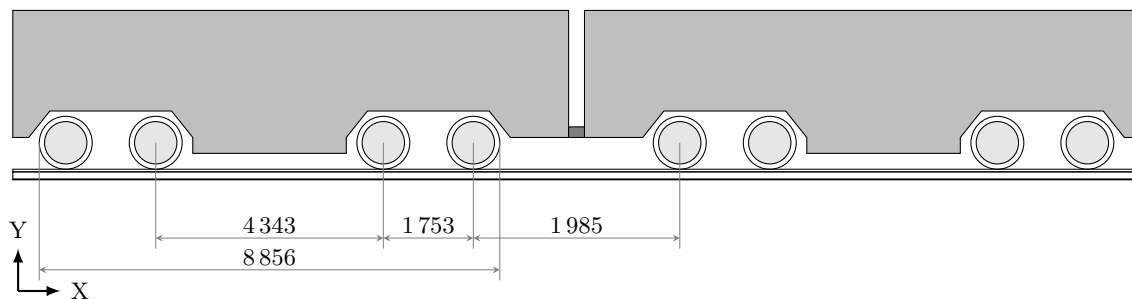


Figure 5.7: Train wheel spacing.

Longitudinal symmetry can be applied to the structure in the middle of the two inner wheels of the first rail vehicle in Figure 5.7 and in the middle of the two vehicles in Figure 5.7 [58]. This gives the model length and load positions shown in Figure 5.8.
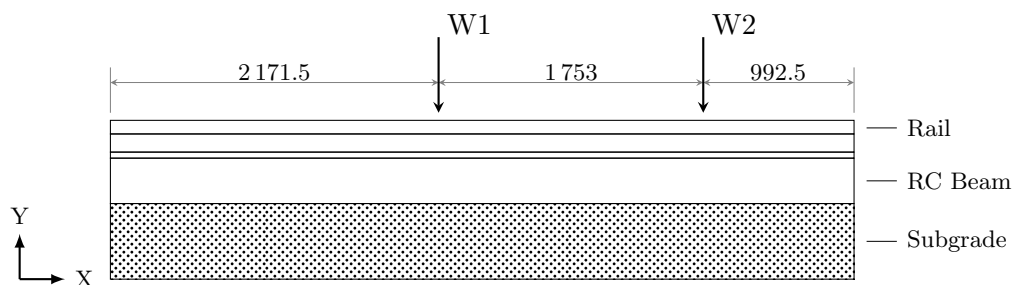


Figure 5.8: Rail section bound by symmetry conditions.

Furthermore the model is loaded with wheel loads of 125 kN applied over an elliptical area derived by the Hertz contact Java application [38], as discussed in Section 3.1.2. The subgrade

is modelled as an elastic foundation with a stiffness of $0.126\,\mathrm{N/mm^3}$, a modulus of subgrade reaction result taken from the PBT results obtained by Verlinde [58]. The UIC48 rail profile and the RC beam are simplified for use in the verification model to simplify the analysis procedure. The rail and RC beam component simplifications are performed in such a manner that the moment of inertia and the cross-sectional areas of the components remain similar, with less than $5\,\%$ deviation from the real cross-sectional properties. The simplified profiles can be seen in Figure 5.12. The RC beam is further simplified by not including the steel reinforcement and PVC duct pipe in the model.

The results of the verification analysis are compared to the results of the reference model in the following figures:

- Figure 5.9 compares displacements;

- Figure 5.10 compares bending moments; and

- Figure 5.11 compares shear forces.

The graphs are identified as reference model or verification model by the (R) and (V) indicators respectively.

The good correspondence between the displacement, bending moment and shear force results allows the adoption of the modelling methods used and the simplification of the cross-sections. The methods can now be implemented in the model of the TMT railway for this study, which is discussed in the following section.
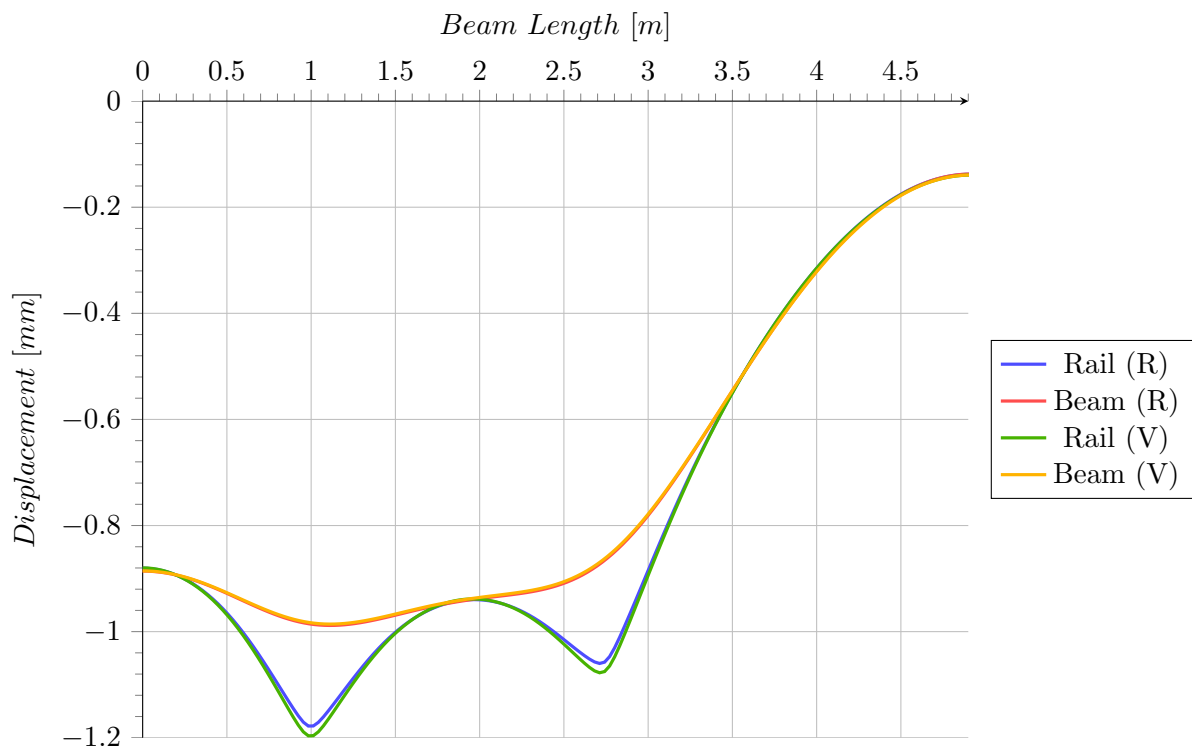


Figure 5.9: Comparison of vertical displacement results.
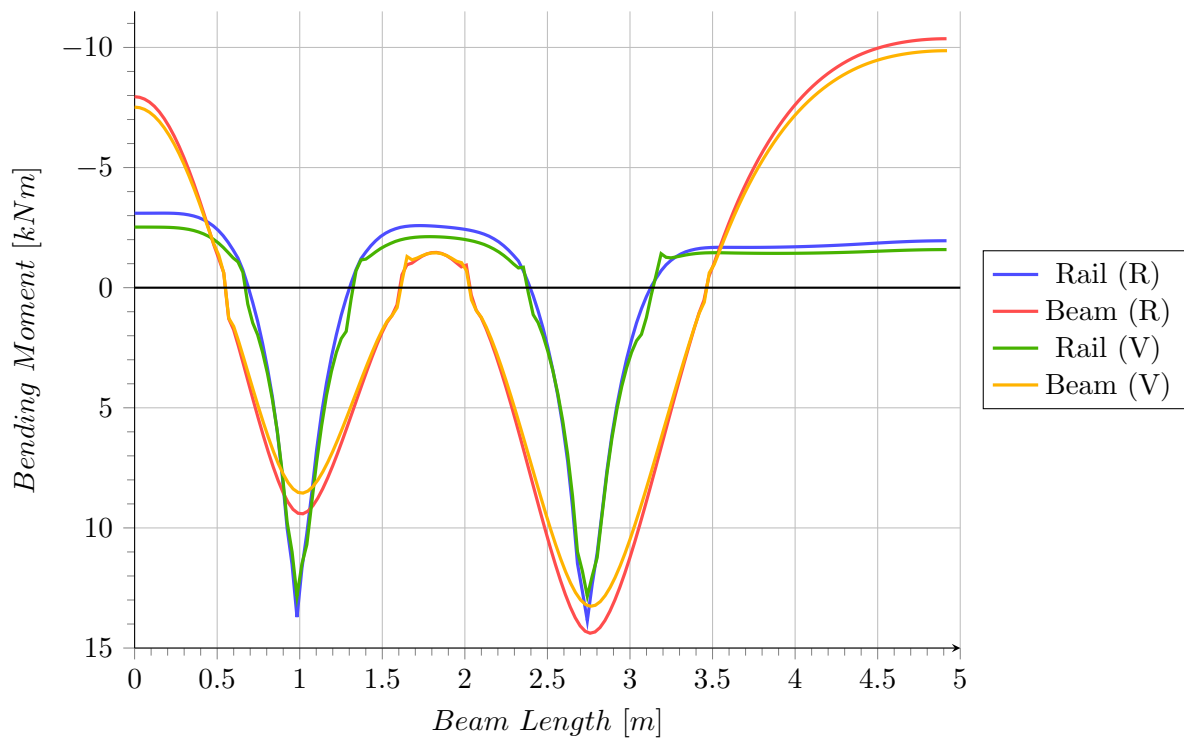
Figure 5.10: Comparison of bending moment results.
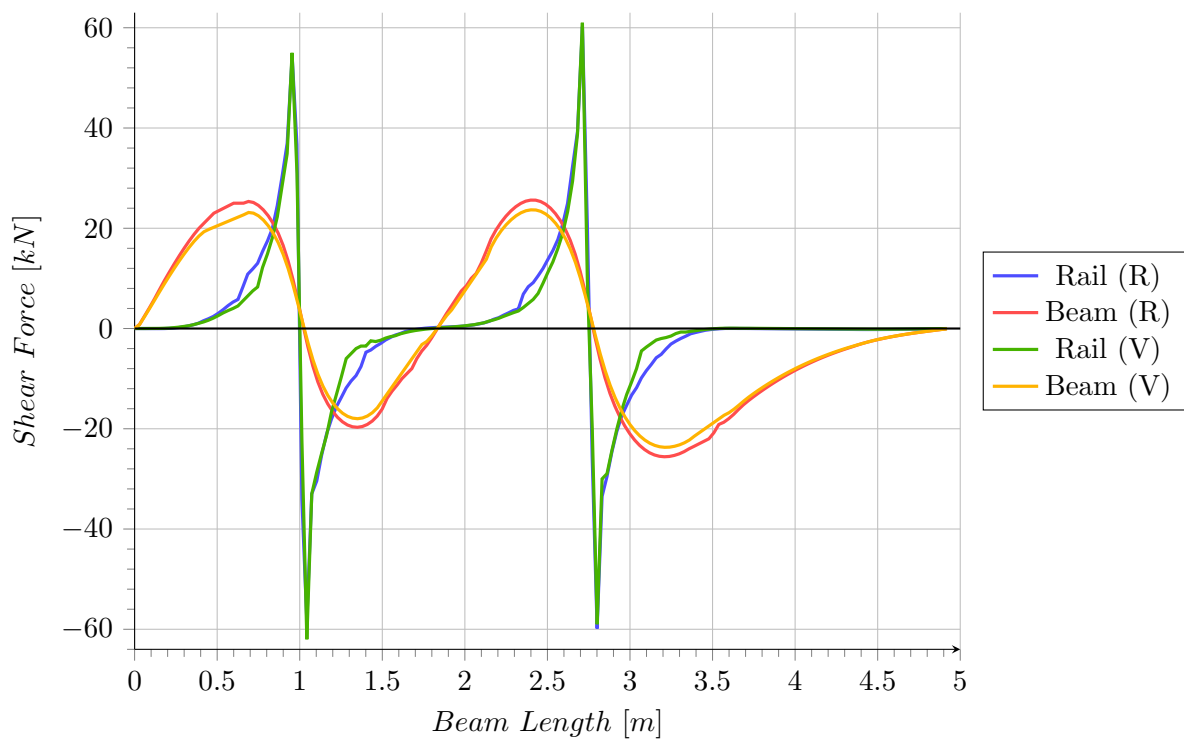


Figure 5.11: Comparison of shear force results.

### 5.4.2  Static TMT 3D Model

To perform the static analysis of the TMT structure the model is set up as specified by the geometry and load conditions described in Section 2.2. The rail and RC beam have been simplified as mentioned in Section 2.2. The rail profile is a UIC60 profile and the dimensions of the RC beam are slightly adapted from the verification model to accommodate for passenger train loading [46]. The symmetrical wheel loads are applied as uniformly distributed loads over two elliptical areas in the middle of the rail head, representing the contact patch between the wheel and rail. The load per wheel is equal to 78.48 kN, which is used to calculate the elliptical contact area and loading pressure with the Hertz contact application [38]. Boundary conditions are applied to the free ends of the components, modelling the symmetry of the loaded structure, restraining longitudinal and lateral (x and z) translation and rotation about the x-axis. An elastic foundation is modelled beneath the grout layer representing the stiffness of the subgrade, which has a stiffness of $0.1043 \text{ N/mm}^3$ according to the results obtained by the PBT analysis in Section 5.3.4. Figure 5.12 shows the mesh used for the TMT model and Figure 5.13 shows the full 3D model with load points and boundary conditions.

The static analysis does not include the inertial effects of the structure or the train vehicles, but it does allow the modelling of linear and non-linear problems. This model will be used to investigate the behaviour of the TMT system under the static load conditions suggested for this study.
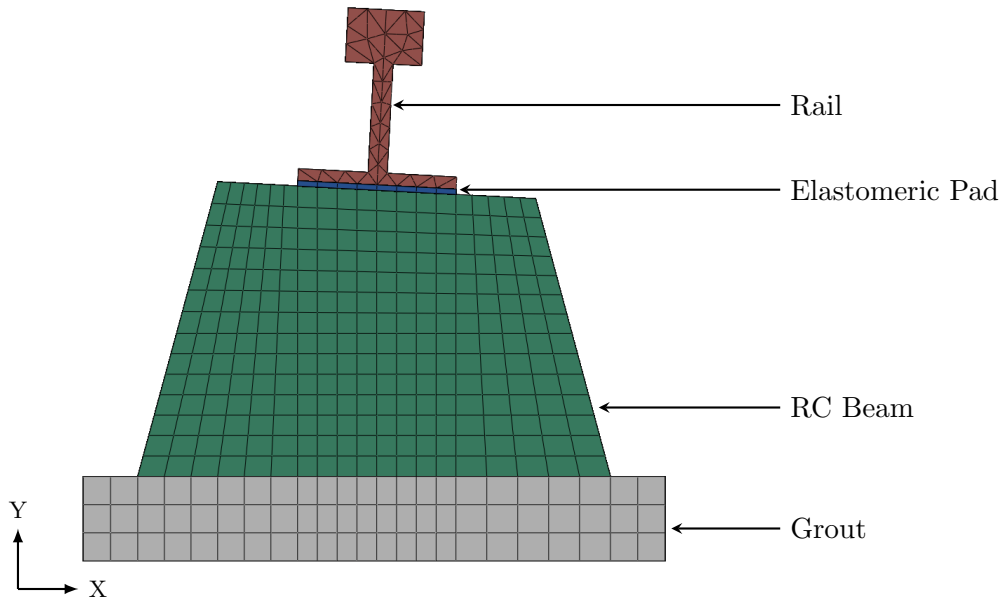


Figure 5.12: TMT model cross-section mesh.

### 5.4.3  Static TMT 3D Model Analysis Results

The results of the static TMT 3D model with geometry and loading according to the conditions for this study are described here. The results contain the displacements, shear forces and
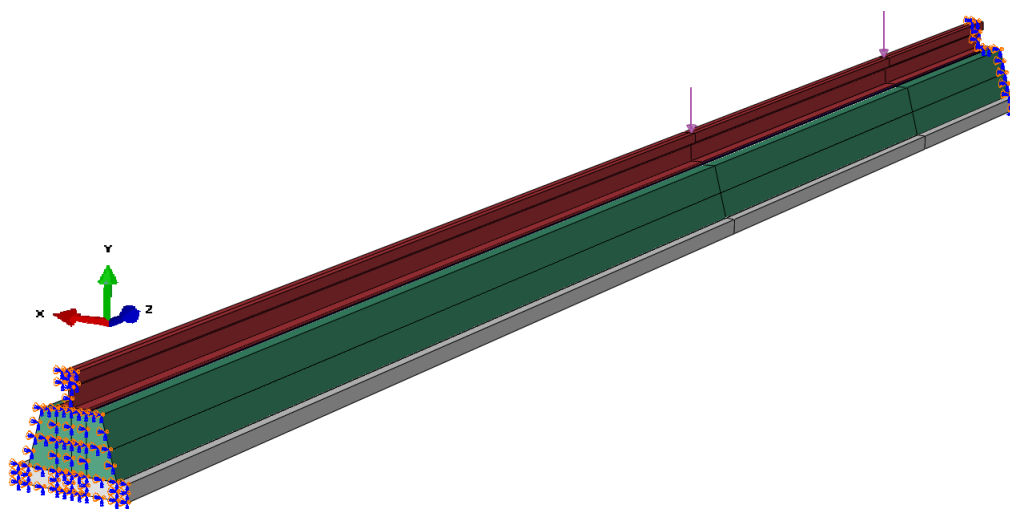
Figure 5.13: TMT model.

bending moments of both the rail and the RC beam.

**Displacements**

Figure 5.15 shows the vertical displacements that occur in the rail and the RC beam when statically loaded. The figure indicates higher, localised deflections in the rail at the points of loading. This difference between the rail and RC beam deflection is created by the elastomeric pad which compresses between the rail and the RC beam. The compression causes a better pressure distribution between the rail and RC beam, decreasing the possibility of damage to the RC beam. The maximum deflection at the centreline of the rail is -0.79 mm and the maximum deflection at the centreline of the RC beam is equal to -0.65 mm. Figure 5.14 shows a visual representation of the 3D model displacements.
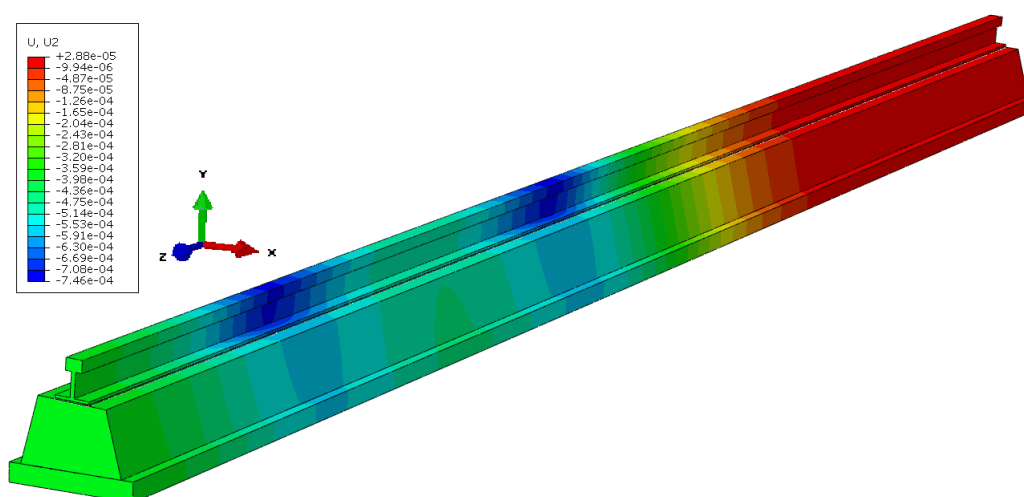


Figure 5.14: 3D TMT model displacements.
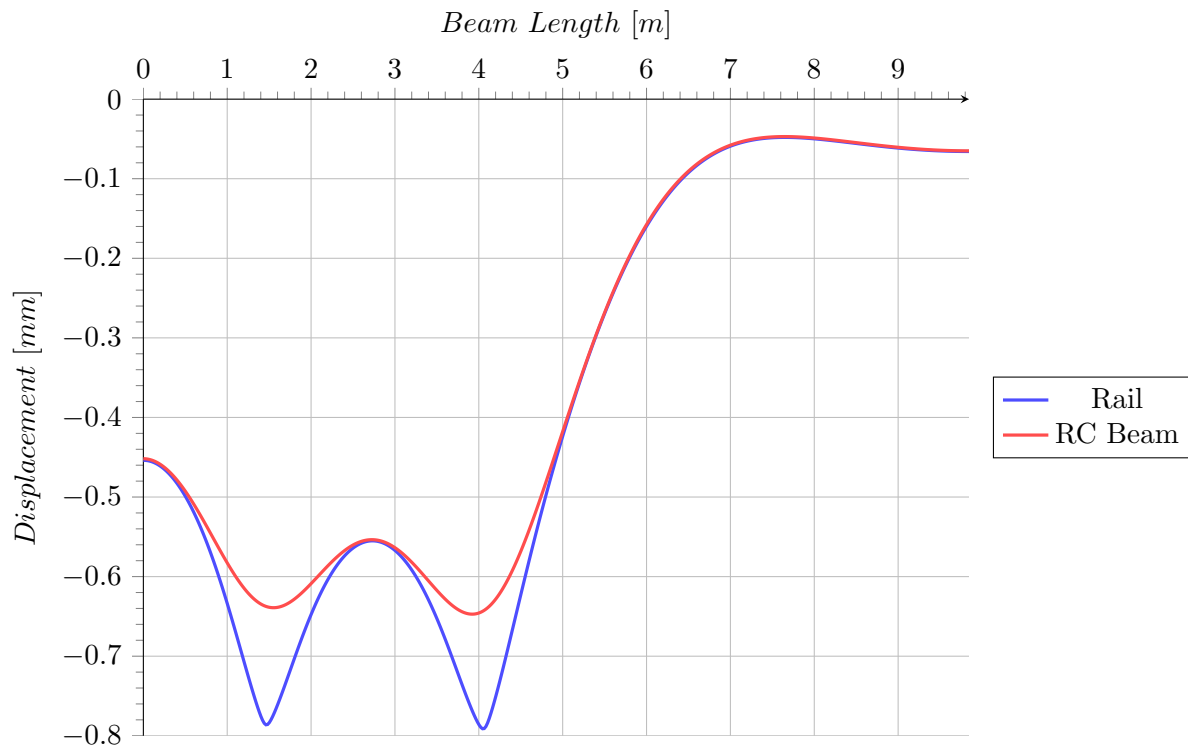
Figure 5.15: 3D model vertical displacement results.

**Bending moments**

Bending moments that occur in the rail and RC beam are shown in Figure 5.16. The maximum bending moments present are 8.53 kN.m and 9.11 kN.m in the rail and RC beam respectively. Minimum bending moments are -1.92 kN.m in the rail and -6.37 kN.m in the RC beam. The tensile and compressive stresses caused by the maximum bending moment in the RC beam are $\sigma_c = 2.15$ MPa and $\sigma_t = 1.89$ MPa, whereas the minimum bending moment causes $\sigma_c = 1.32$ MPa and $\sigma_t = 1.50$ MPa.

**Shear forces**

The maximum shear forces in the rail and RC beam are 43.85 kN and 15.97 kN respectively. The shear force distribution of both the rail and the RC beam are shown in Figure 5.17. The shear forces in the RC beam are represented by a smoother curve, this is due to the effect of the elastomeric pad between the rail and RC beam which increases the contact area between the rail and the RC beam. The increased contact area improves the pressure distribution on the RC beam and decreases the shear forces in the RC beam.
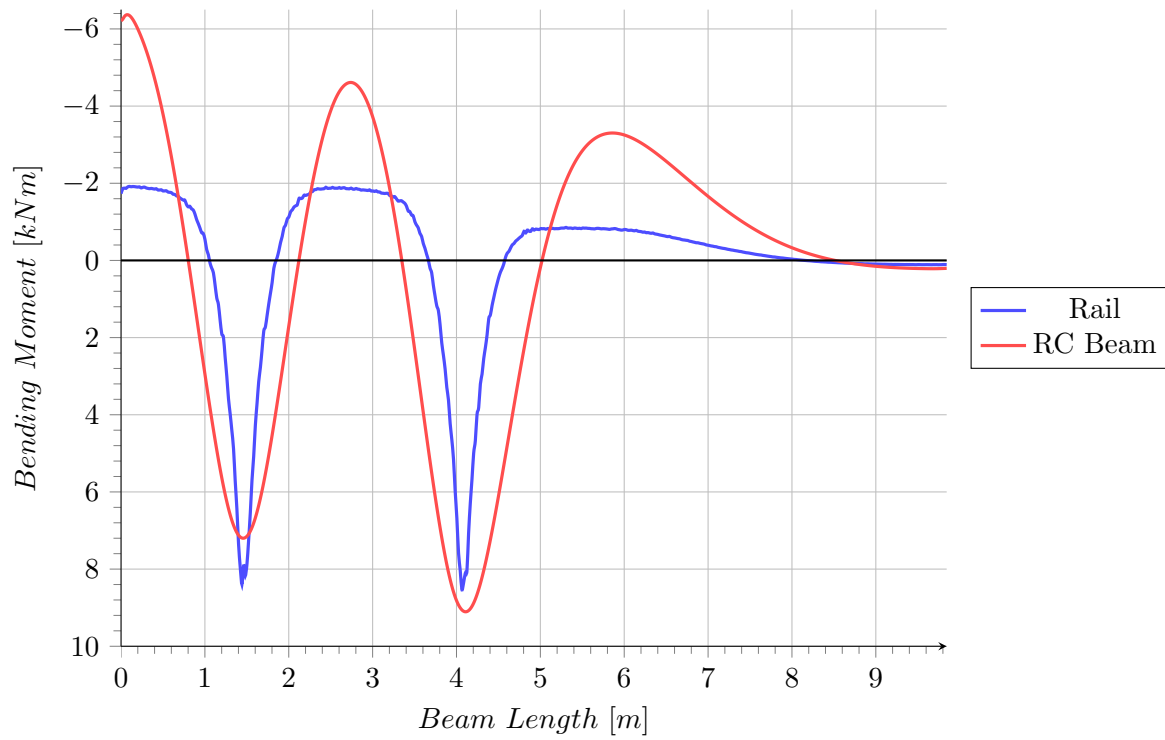
Figure 5.16: 3D model bending moment results.
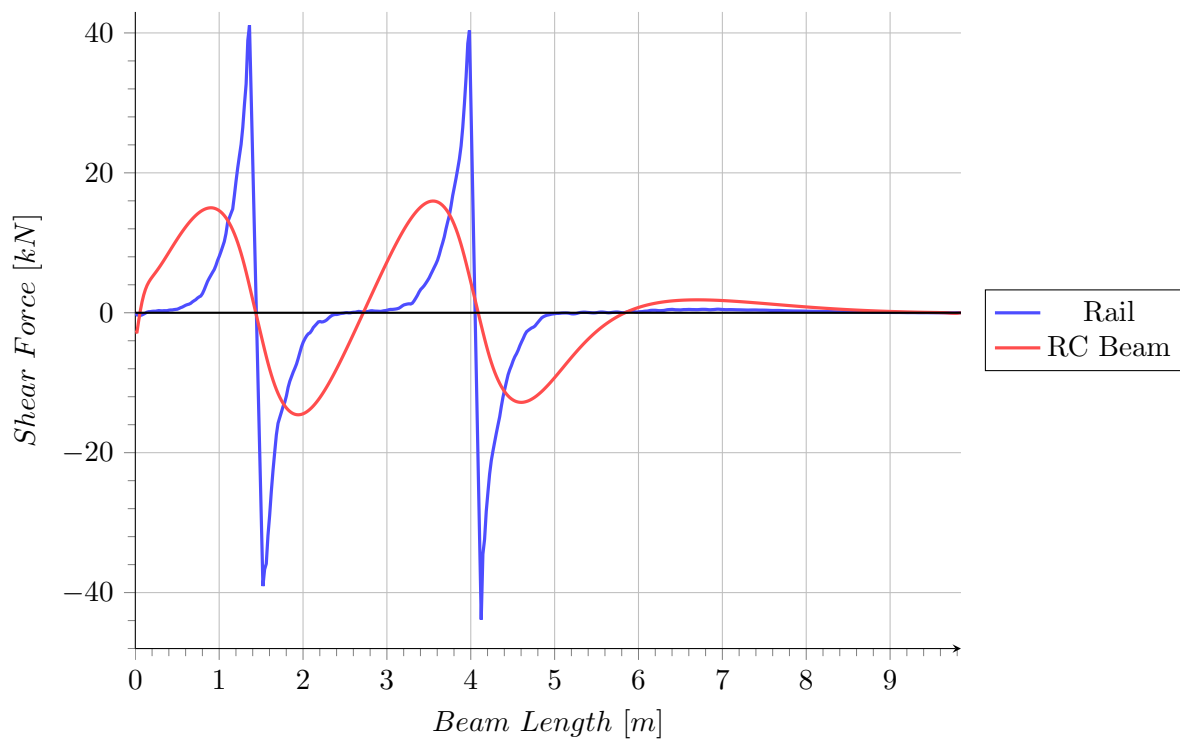


Figure 5.17: 3D model shear force results.

### 5.4.4   Static TMT 2D Model

The computational effort required for the 3D model becomes expensive due to the cross-sections of the components that need fine meshes compared to the length of the model, which creates a large amount of elements in each component. In order to simplify the complexity of the 3D model it is simplified to a 2D model with the use of beam elements which are better suited to mesh slender components. This section describes the element types, geometry, boundary conditions and load applications of the simplified model.

A section of the 2D model is shown in Figure 5.18. The rail and RC beam are modelled by 1D beam elements with profiles representing the 3D cross-sections. To model the elastomeric pad and the grout layer 2D plane stress elements are used. Contact between the components is defined similar to the contact in the 3D model. The normal contact definition allows no penetration of one component into the other, the tangential contact definition is assigned a friction coefficient of 0.6 and no separation of the components is allowed after contact is initiated. The subgrade is modelled similar to the 3D model, with the elastic foundation function assigning a stiffness to the bottom edge of the grout layer. The subgrade stiffness is also input as $0.1043\,\mathrm{N/mm^3}$. When comparing the stresses below the grout in both the 2D and 3D models the similar vertical stresses in the grout show that the correct grout width is taken into account when applying the foundation stiffness. In the 2D model the Hertz theory approach is not used to model the train wheel. In the 2D representation a simpler approach is used i.e. the wheel is represented as a disc, which will not increase the computational expense of the model as a 3D model of the wheel would have done. Contact results for the 2D model show that contact occurs over a distributed length, and not a concentrated point, between the discs and the rail. Considering the symmetrical loading of the structure the same symmetry boundary conditions of the 3D model are applied to the ends of the 2D components, constraining movement in the longitudinal direction (x) and rotation about the out-of-plane axis (z). Figure 5.18 shows a wheel modelled as an analytical rigid component, which will apply the wheel loads as distributed loads to the rail and model the movement of the wheel as well as the contact between the wheel and the rail.
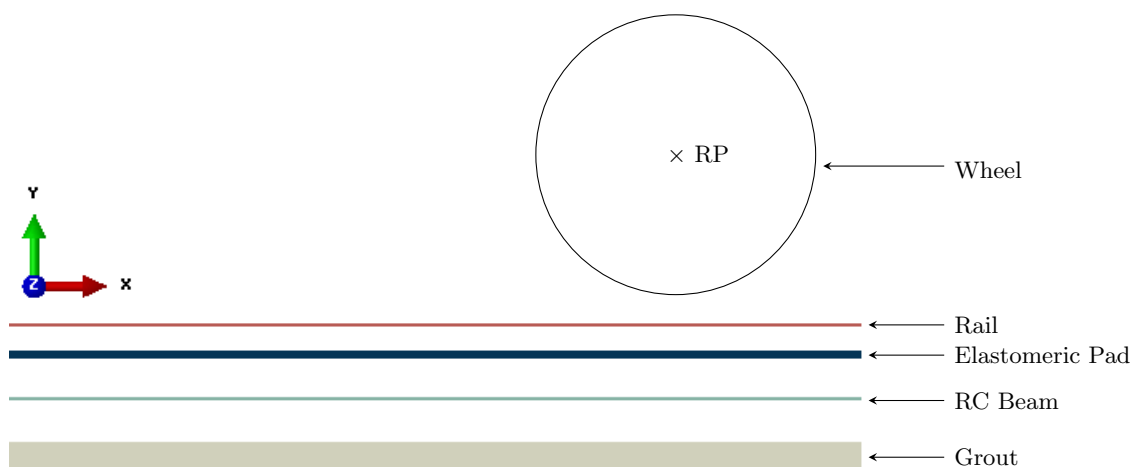


Figure 5.18: 2D TMT model section.

### 5.4.5   Static TMT 2D Model Analysis Results

The results shown below are for the static TMT 2D model created as discussed above. From the results it can be seen that there are only minor differences between the 2D and 3D models with respect to displacements and bending moments. These similar results allow the use of 2D models in following models created for this study.

#### Displacements

Figure 5.19 shows the vertical displacements that occur in the rail and the RC beam of the 2D model when statically loaded. The figure indicates the same localised deflections in the rail at the points of loading due to the elastomeric pad compressing. The maximum deflection at the centreline of the rail is -0.78 mm and the maximum deflection at the centreline of the RC beam is equal to -0.68 mm.

#### Bending moments

Bending moments that occur in the 2D rail and RC beam are shown in Figure 5.20. The maximum bending moments present are 8.10 kN.m and 9.72 kN.m in the rail and RC beam respectively. Minimum bending moments are 1.94 kN.m in the rail and 6.69 kN.m in the RC beam. The compressive and tensile stresses caused by the maximum bending moments in the RC beam are $\sigma_c = 2.30$ MPa and $\sigma_t = 2.01$ MPa, whereas the minimum bending moments in the RC beam cause $\sigma_c = 1.39$ MPa and $\sigma_t = 1.58$ MPa stresses.

#### Shear forces

The maximum shear forces in the 2D rail and RC beam are 39.06 kN and 18.28 kN respectively. The shear force distribution of both the rail and the RC beam are shown in Figure 5.21. The same smoother curve for the RC beam, as seen in the results of the verification model and the 3D model, due to the effects of the elastomeric pad is seen here.

### 5.4.6   2D and 3D results comparison

Table 5.6 shows a comparison between the 2D and 3D model results.
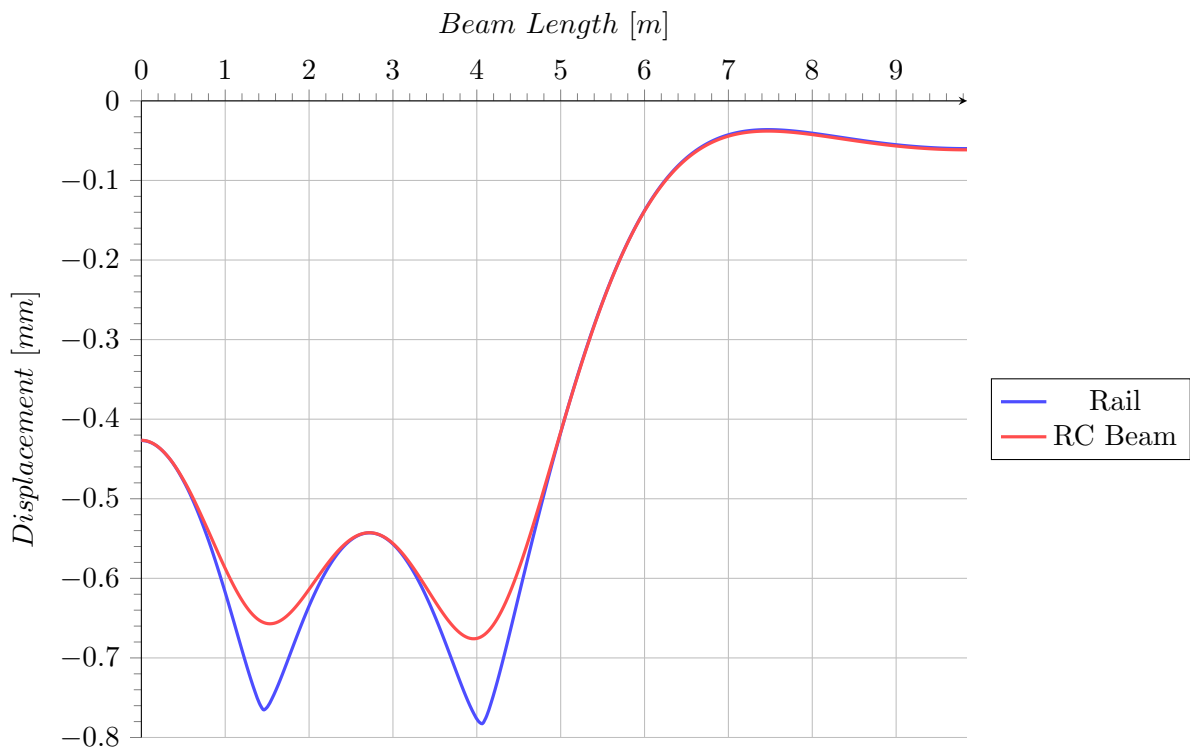
Figure 5.19: 2D model vertical displacement results.
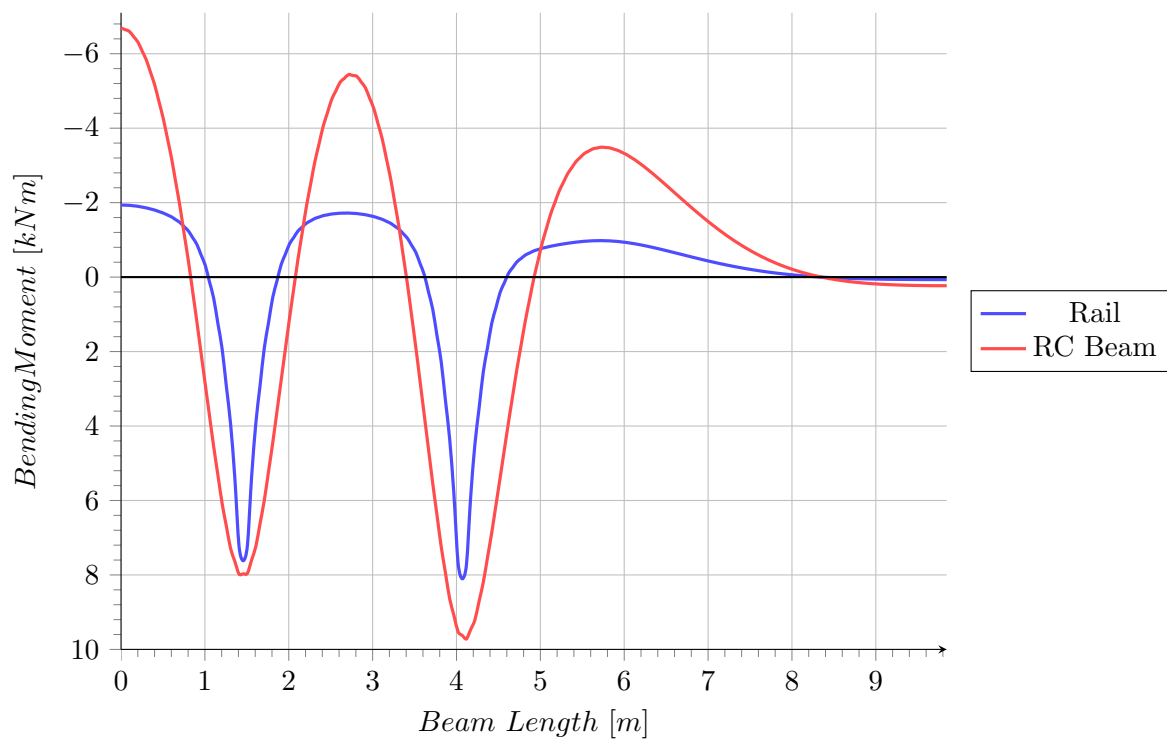


Figure 5.20: 2D model bending moment results.
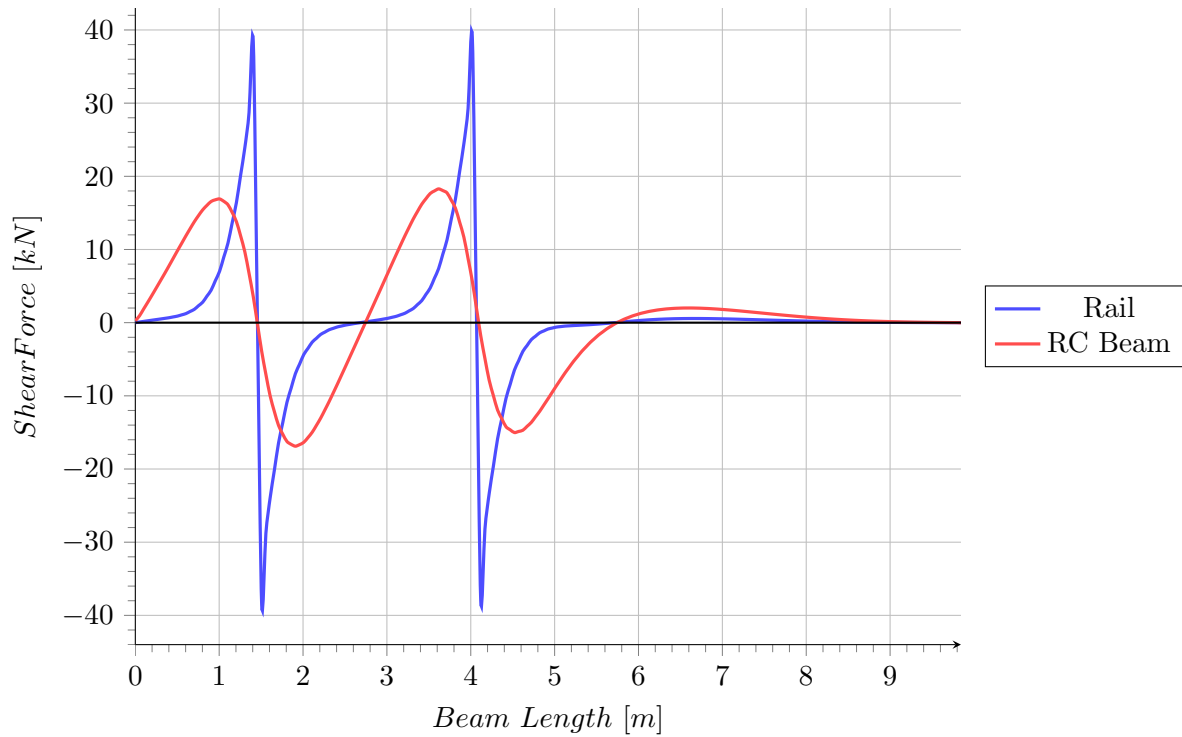
Figure 5.21: 2D model shear force results.

Table 5.6: 2D and 3D results summary.

| | Rail | | | RC Beam | | |
|---|---|---|---|---|---|---|
| Dimension | $w$ | Bending Moment | Shear Force | $w$ | Bending Moment | Shear Force |
| | [mm] | [kN.m] | [kN] | [mm] | [kN.m] | [kN] |
| 2D | 0.78 | 8.10 | 39.06 | 0.68 | 9.72 | 18.28 |
| 3D | 0.79 | 8.53 | 43.85 | 0.65 | 9.11 | 15.97 |
| Difference [%] | -1.27 | -5.04 | -10.92 | 4.62 | 6.70 | 14.28 |

## 5.5   TMT Dynamic Analysis

This section investigates the dynamic behaviour of the TMT 2D model discussed in Section 5.4. To determine the dynamic behaviour of the structure an implicit, dynamic analysis is performed with the applied 94 km/h load conditions which is the same as the train speed during the displacement measurements on the reference ballasted and transition rail sections. The dynamic behaviour that is investigated for the TMT structure includes:

- maximum displacement,

- bending moment distribution,

- shear force distribution,

- modal response to high frequency loading and

- dynamic amplification factor.

Abaqus is designed to analyse structural components, which implies that the overall dynamic response of the structure is sought. Dynamic problems are seen as inertial problems, excluding wave effects such as focusing, reflection and diffraction, which are deemed unimportant for structural analysis. The structural problems are considered as inertial since the response time is long compared to the time required for waves to traverse the structure. To perform a dynamic analysis Abaqus provides the ability to analyse both linear and non-linear problems. Pure linear systems are often the desired option for dynamic analyses, due to the analysis being more cost effective than the direct-integration methods used for non-linear problems and for the provision of information on the dynamic behaviour of the structure through extraction of the eigenvalues of the system. This can be used to obtain natural frequencies of vibration or possible bifurcations that may be associated with kinematic instabilities. For slightly non-linear problems the modal projection method is provided for which the basis is the eigenmodes of the linear system and the eigenmodes are used as a set of global Ritz functions (a set of global interpolation functions) whose amplitude define the response of the structure. For more severe non-linear models Abaqus makes use of direct time integration of all the degrees of freedom of the finite element model to obtain the dynamic response [14]. The method of analysing such a non-linear problem is discussed here.

By making use of an implicit, dynamic scheme the dynamic quantities are not only solved at time $t$, but also at time $t + \Delta t$. Therefore, non-linear equations need to be solved, because the dynamic quantities are implicit. When choosing an appropriate time increment three factors need to be considered [14]

- the rate of variation of the applied loading;

- the complexity of the non-linear damping and stiffness properties; and

- the typical period of vibration of the structure.

Generally an increment versus period ratio $\Delta t/T < 1/10$ is a good assumption for reliable results. $T$ is the period of a mode of the structure and $\Delta t$ is the time step used in the analysis.

Abaqus provides two implicit operators for time integration of a dynamic problem, the operator defined by Hilber, Hughes and Taylor [21] and the backward Euler operator. The Hilber-Hughes-Taylor operator is a generalized form of the Newmark operator with controllable numerical damping. The main appeal of the Hilber-Hughes-Taylor operator is its controllable numerical damping, slowly increasing at low frequencies with more rapid growth in damping at high frequencies. The numerical damping is controlled by the $\alpha$–parameter. If $\alpha$ is equal to zero there is no damping and the operator is the trapezoidal rule (for the Newmark $\beta$-method, $\beta = 0.25$), while $\alpha = $ -1/3 provides significant damping. A value of $\alpha$ equal to -0.05 is a good choice to remove the high-frequency noise which enters the solution when a time step change occurs when automatic time stepping is used [14].

Application of structural damping is done with the Rayleigh damping method. Two other methods of damping are mass proportional damping ($\mathbf{C} = \alpha\mathbf{M}$) and stiffness proportional damping ($\mathbf{C} = \beta\mathbf{K}$). Rayleigh damping is a more general case where the damping matrix is defined by a linear combination of the mass and stiffness matrices [24], giving

$$\mathbf{C} = \alpha\mathbf{M} + \beta\mathbf{K} \tag{5.3}$$

where | $\mathbf{C}$ | = | Damping matrix
--- | --- | --- | ---
| $\mathbf{M}$ | = | Mass matrix
| $\mathbf{K}$ | = | Stiffness matrix
| $\alpha$ | = | Mass proportionality constant
| $\beta$ | = | Stiffness proportionality constant

The damping ratio, $\xi_n$, for the $n^{th}$ mode of a system as defined in Equation 5.3 is

$$\xi_n = \frac{\alpha}{2\omega_n} + \frac{\beta\omega_n}{2}, \tag{5.4}$$

with $\omega_n$ being the natural frequency of that mode [7]. From this it is seen that the damping matrix is proportional to a linear combination of the mass matrix and the stiffness matrix. This makes Rayleigh damping easy to define by choosing $\xi$ for two modes and calculating the corresponding $\alpha$ and $\beta$ values. The two values for $\xi$ are typically chosen for the first mode and one of the last modes in the considered frequency range. This allows one to use Equation 5.4 to provide damping values for the modes in-between the chosen modes and monotonically increase the damping ratio after the highest chosen mode [7]. In Equation 5.4 $\alpha$ contributes to $\xi_n$ with an inverse proportionality to $\omega_n$ while $\beta$ leads to a contribution to $\xi_n$ which increases linearly with $\omega_n$. When combined, $\alpha$ controls for low frequencies and $\beta$ for high frequencies in the Rayleigh damping definition [9]. The following section discusses the creation of the dynamic TMT 2D model with the use of the methods investigated above.

### 5.5.1  Dynamic TMT 2D Model

Analysing the TMT structure with the implicit, dynamic procedure is done by creating four analytical rigid wheels that pass over the same TMT 2D model used in Section 5.4.4. The simulated wheel loads, travelling at 94 km/h, are the four wheels closest to each other at the connection between two vehicles. The effects of the wheels quickly dissipate and do not affect following wheel loads, allowing only the four wheels to be modelled and not all the wheels of the train. The wheels are loaded vertically with 78.48 kN each and are then displaced horizontally over the length of the rail. The horizontal displacement is applied over a specified time to simulate the 94 km/h speed of the wheel, adjacent wheels have the same speed and displacement, but are out of phase with the first wheel, their displacements are applied at a delayed time in the analysis, in order to simulate the loading effect of the geometrical position of the four consecutive wheels passing over the rail. Elastic foundation stiffness and contact definitions remain the same as for the static 2D model. Boundary conditions are only applied to the ends of the model for analysis stability. The $\Delta t/T < 1/10$ guideline in the previous section, where $T = 1/62.48$ s from Figure 5.22, suggests that a time step smaller than 0.0016 s should be used. A time step of 0.001 s was used for the analysis of the dynamic TMT 2D model.

To define the Rayleigh damping of the TMT structure different values of $\alpha$ and $\beta$ need to be investigated to determine the impact the constants have on the displacement, bending moment and shear force behaviour of the structure. Table 5.9 contains a summary of the results obtained for a model using a stiffness proportionality constant of 0.0008. No mass proportional damping is considered since $\alpha$ has negligible contribution to the system damping, because of the high natural frequencies of the TMT structure, shown in Table 5.7 . Table 5.8 shows the resulting damping ratios for each mode of the structure due to $\beta = 0.0008$. The damping ratios are calculated with Equation 5.4. The value of $\beta$ was chosen to result in a damping ratio between 15 and 30 %.

Table 5.7: Response angular frequencies for the first five modes of the TMT system.

| Response angular frequencies [rad/s] | | | | |
|---|---|---|---|---|
| $\omega_1$ | $\omega_2$ | $\omega_3$ | $\omega_4$ | $\omega_5$ |
| 392.57 | 403.70 | 448.78 | 550.71 | 716.22 |

Table 5.8: Damping ratios for the first five modes of the TMT system.

| $\alpha$ | $\beta$ | Damping ratios [-/-] | | | | |
|---|---|---|---|---|---|---|
| | | $\xi_1$ | $\xi_2$ | $\xi_3$ | $\xi_4$ | $\xi_5$ |
| 0 | 0.0008 | 0.157 | 0.161 | 0.180 | 0.220 | 0.286 |

Table 5.9 shows that the application of damping to the TMT structure has some effect on the results obtained. The rail displacements, shear forces and bending moments for $\alpha$ and $\beta$ equal to zero are larger than the results of the static analysis, this is as expected due to dynamic amplification. When $\beta$ values are applied a decrease can be seen in displacements, bending moments and shear forces in both the rail and RC beam. All values obtained with $\beta$ equal to 0.0008 remain larger than the static load case, except for rail displacement, which is

lower than the rail displacement in the static case. This could indicate that the system is over damped for a $\beta$-value of 0.0008. Results were also investigated for a $\beta$ value of 0.0005 (10 - 18 % damping ratio), which yielded results similar to those obtained for the 0.0008 $\beta$ value. Because the application of $\beta$ damping to the dynamic analysis seems to over damp the system further analyses will be performed without damping. This is a conservative decision, since the displacements, bending moments and shear forces are larger than those of the damped models and are larger than those of the static model, as expected.

Table 5.9: Damping sensitivity.

|          | $\alpha$ | $\beta$ | Rail | | | RC Beam | | |
|----------|---|---|---|---|---|---|---|---|
|          |   |   | $w$ | Bending Moment | Shear Force | $w$ | Bending Moment | Shear Force |
|          | - | - | [mm] | [kN.m] | [kN] | [mm] | [kN.m] | [kN] |
| Static   | - | - | 0.88 | 7.76 | 38.11 | 0.68 | 7.42 | 17.35 |
|          | 0 | 0 | 1.03 | 10.17 | 49.96 | 0.74 | 12.57 | 20.11 |
| Dynamic  | 0 | 0.0005 | 0.79 | 8.94 | 42.94 | 0.74 | 9.74 | 19.12 |
|          | 0 | 0.0008 | 0.79 | 8.93 | 42.56 | 0.72 | 9.72 | 18.72 |

### 5.5.2   Dynamic TMT 2D Model Analysis Results

Results for the dynamically loaded TMT model are discussed here. The results for bending moments and shear forces are given at time t = 0.1554 s when the load geometry is similar to the static analysis with only two wheels loading the TMT structure in the symmetrical load configuration. The displacement results are plotted over the time it takes all four wheels to cross the midpoint of the rail along the length of the rail.

**Modal response**

The modal response of the TMT structure determines whether the load excitation of the structure will cause it to resonate. According to Verlinde [58] the natural frequencies of the TMT structure are much higher than the excitation frequencies of train loads. This is true for the low speeds of freight train vehicles ($\approx 43$ km/h), but for the maximum possible train speed of 160 km/h of the reference train used in this study the modal response of the structure needs to be considered. Resonance could create excessive displacements, forces and vibrations in the structure which could threaten the integrity of the structure. The excitation frequency varies between 2.257 - 17.094 Hz, depending on whether a single wheel or groups of wheels are considered during the frequency calculation.

The first and fourth mode shapes of the structure have the frequencies 62.48 Hz and 87.65 Hz respectively and are shown in Figure 5.22. They are much higher than the load frequencies applied by the train wheels. This large difference between the load frequencies and mode frequencies implies that resonance will not occur in the TMT structure and will not have a significant effect on the forces or displacements in the structure.

Mode 1 Frequency = 62.48 Hz

Mode 4 Frequency = 87.65 Hz
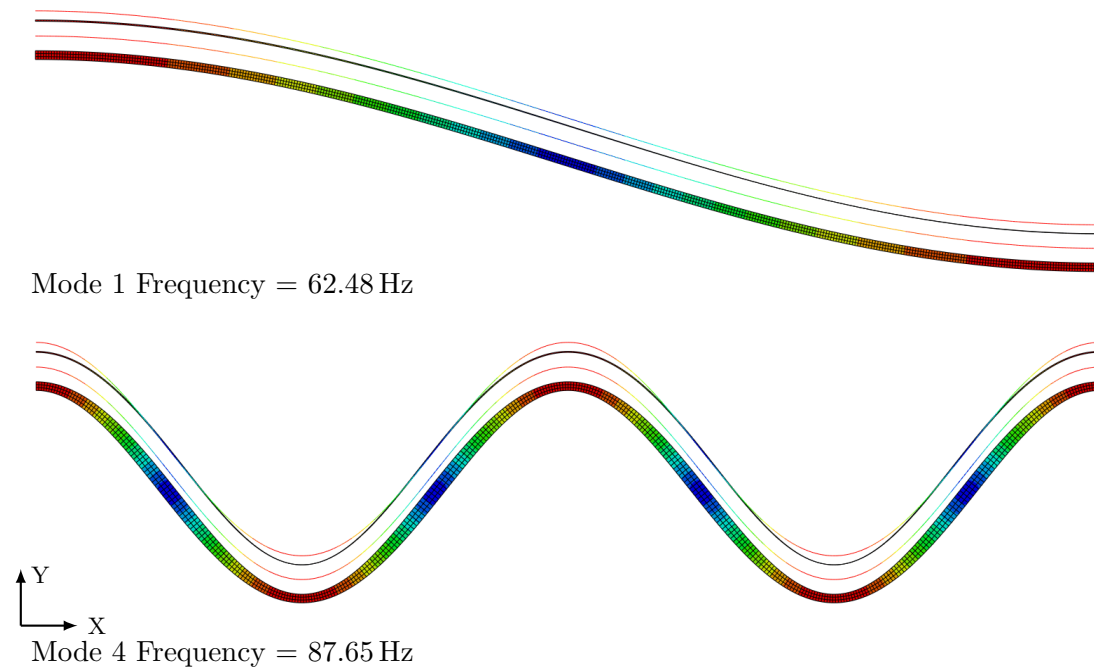
Figure 5.22: Mode shapes.

## Displacements

Figure 5.23 shows the vertical displacements that occur in the rail and the RC beam of the 2D model when dynamically loaded. The displacements are shown after t = 1 s, because the first second of the analysis is only used to initiate contact between the various components. The maximum deflection at the centre of the cross-section, over the length of the rail is -0.81 mm and the maximum deflection at the centre of the cross-section, over the length of the RC beam is equal to -0.75 mm. When comparing the static and dynamic displacement results the dynamic displacements are greater than the static displacements, as expected, due to dynamic amplification occurring. The DAF can be calculated with Equation 5.5:

$$DAF = \frac{u_0}{u_{st}} \tag{5.5}$$

Taking $u_0$, the dynamic displacement, equal to -0.81 mm and $u_{st}$, the static displacement, equal to -0.78 mm a DAF of 1.04 is obtained.

## Bending moments

The bending moments that occur in the 2D rail and RC beam during the dynamic loading are shown in Figure 5.24. The maximum bending moments present are 8.6 kN.m and 9.61 kN.m in the rail and RC beam respectively. Minimum bending moments are -1.86 kN.m in the rail and -7.01 kN.m in the RC beam. The tensile and compressive stresses caused by the maximum bending moments in the RC beam are $\sigma_c = 2.34$ MPa and $\sigma_t = 1.90$ MPa, whereas the minimum bending moments in the RC beam cause $\sigma_c = 1.38$ MPa and $\sigma_t = 1.71$ MPa stresses.  The

dynamic bending moments diagrams are similar to the static bending moment diagrams.

**Shear forces**

The maximum shear forces during the dynamic loading in the 2D rail and RC beam are $42.00\,\mathrm{kN}$ and $18.30\,\mathrm{kN}$ respectively. The shear force distribution of both the rail and the RC beam are shown in Figure 5.21. Shear force results for the dynamic analysis are similar to the static results.
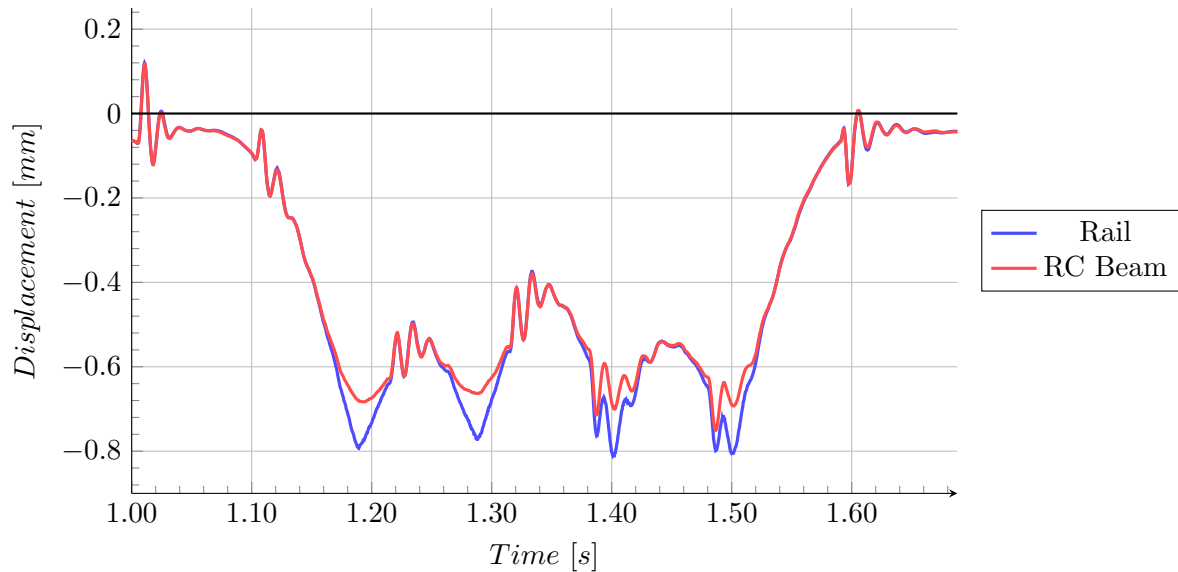


Figure 5.23: Time history of vertical displacement results.
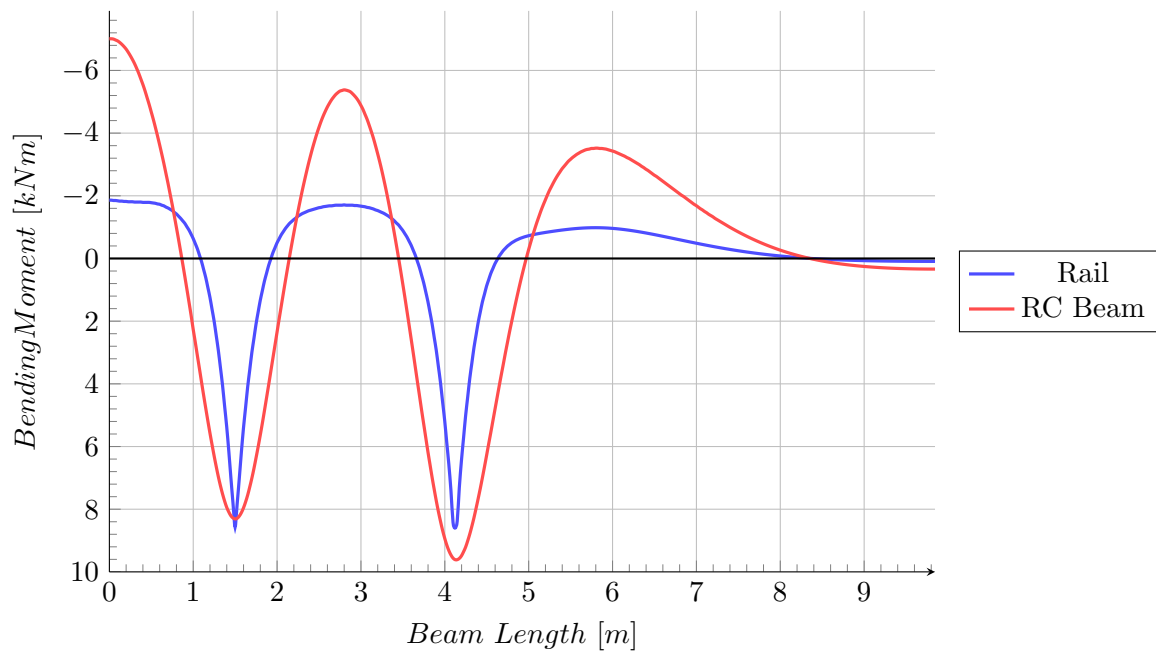


Figure 5.24: t = 0.1554 s Bending moment results.
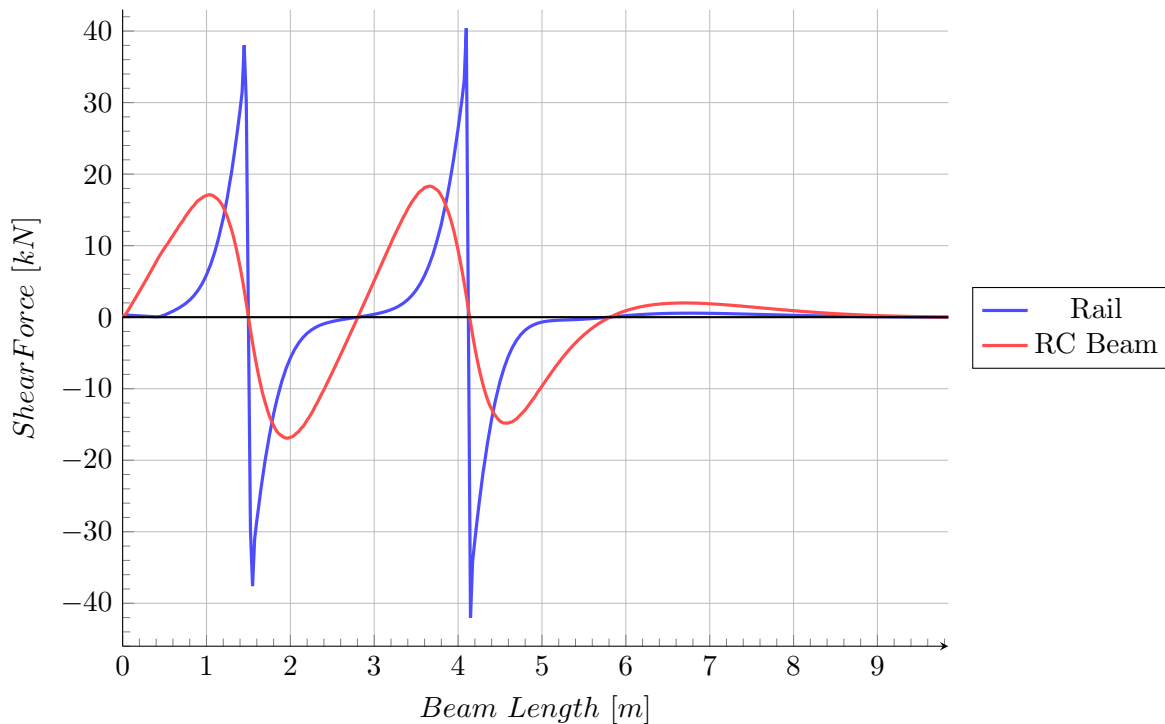
Figure 5.25: t = 0.1554 s Shear force results.

## 5.6   Summary

The objective of this chapter was to research and analyse methods of creating an accurate model of the TMT structure. To achieve this a study of the possible finite elements available for the modelling of the TMT structure and a mesh sensitivity analysis was performed. The mesh sensitivity analysis indicates that an average mesh size of 25 mm is the most effective mesh size. The contact and interaction modelling between the TMT structure components and the subgrade layers were defined as hard contact with no separation after contact initiation and a tangential coefficient of friction of 0.6 was applied. A subgrade model was used to calculate the stiffness of the subgrade with a PBT analysis and yielded a modulus of subgrade reaction of $0.1043 \, \text{N/mm}^3$.

A 3D model of the TMT structure was created to allow verification of modelling techniques such as loading, boundary conditions and meshing. The verified techniques were then used to create a static 3D model of the TMT structure in this study. The results for the 3D model show a good comparison to the verification model results with a difference in maximum values due to the different vehicle loads used in the two models. But the analysis time of the 3D model makes the model inefficient and when combining the TMT model with the ballasted rail model the analysis time will become even greater. To allow for shorter analysis periods the TMT model was simplified to a 2D model.

Both a static and dynamic analysis was performed on the 2D model in order to determine the DAF of the TMT structure. The dynamic 2D model showed results which are comparable to the static model. As expected the peak values for the dynamic model were slightly higher

when compared to the static model, when damping was not considered. When damping was considered the rail displacements were lower than the static rail displacements. The higher values are due to the DAF which was calculated as 1.04. The dynamic results are similar to the static results due to the low masses and no damping included in the models, which result in quasi-static behaviour of the dynamic model. There are waves visible in the displacement results in Figure 5.23. The waves appear every 0.1 s for a few cycles and then damp out, presumably due to numerical damping. These waves are assumed to be some transient waves which occur due to the initial application of a wheel load and the removal of the wheel loads from the track. Table 5.10 shows a summary of the results for the dynamic analysis of the TMT 2D model.

Table 5.10: 2D TMT dynamic results summary.

|  | Maximum Displacement [mm] | Maximum Bending Moment [kN.m] | Minimum Bending Moment [kN.m] | Maximum Shear Force [kN] |
|---|---|---|---|---|
| Rail | -0.81 | 8.60 | -1.86 | 42.00 |
| RC Beam | -0.75 | 9.61 | -7.01 | 18.30 |

# Chapter 6

# Ballasted Rail Discrete Element and Finite Element Analysis

This chapter describes the creation, analyses and results of the DEM 3D and simplified FEM 2D models for the ballasted rail structure. A static analysis is done for the 3D model and the 2D model is analysed statically and dynamically. The aim is to calibrate the behaviour of the models with a reference rail structure and determine whether the simplified 2D model could provide an accurate representation of the ballasted rail behaviour.

To accurately model the ballasted rail structure the modelling aspects and elements used are investigated for the 2D and 3D finite elements and the 3D discrete elements. The modelling aspects include:

- rigid and deformable finite elements,

- subgrade elastic behaviour, and

- discrete element particles and particle interaction.

After the various modelling aspects have been discussed the different models are described in terms of components of the structure, component assembly, boundary conditions, interactions, load applications and type of analysis performed. Results are obtained via an explicit, dynamic analysis for the static DEM 3D model and via an implicit, dynamic analysis for the simplified static and dynamic FEM 2D models. Finally the results of the various models are discussed and compared.

## 6.1   FEM Components

Finite elements used and techniques of implementing these elements in the 3D and 2D models are discussed in this section. In the 3D model the finite elements are used to model the wheels, rail, rail pads, sleepers, containing walls and subgrade and the 2D model uses finite elements

78

to model the rail, rail pads, sleepers and subgrade. No discrete elements are used in the 2D model; the elastic foundation option is used to replace the ballast and subgrade.

### Rail

Both the 3D and 2D models use a beam bending component with the UIC60 profile to model the rail. Modelling the rail as a full 3D displacement FEM component will require a fine mesh to accurately define its geometry, increasing computational cost. Using quadratic interpolation beam elements greatly decreases the number of elements necessary to define the rail and makes it easier to extract section force results along the centreline of the rail.

### Rail pad

Elements used to model the rail pads are the same as used for the elastomeric pads in the TMT model in Chapter 5. The 3D rail pads are modelled with linear, hexahedral elements which use incompatible modes. In the 2D model the pads are modelled with bilinear, quadrilateral, plane stress elements also using incompatible modes.

### Rigid FEM Components

Discrete particles can move freely in the 3D space and therefore have to be contained to the area of interest. Containment of the particles is done with rigid FEM components. Rigid bodies are constrained to the motion of a reference point and the location of all the nodes on the body remain the same relative to the reference point. Rigid bodies have no stress results, only displacements are recorded for these bodies. These rigid bodies are used to model the floor (subgrade), which is represented by multiple rigid plates; the rigid walls used to create a box around the particles to contain them; and the wheels. The wheels are analytical rigid, shell components in the 3D model and rigid, line components in the 2D model.

Deformable elements showed excessive mesh distortion when coming into contact with particle elements. Since the stiffness of the sleepers is high relative to the stiffness of the ballast, subgrade and rail pads the contribution of the sleepers to the rail displacement is negligible. This allows modelling the sleepers as rigid, solid components which removes the difficulty with mesh distortion. In the 2D model the sleepers are modelled as deformable components, because there are no particle interactions. The change from rigid to deformable components will have no significant effect on the displacement results of the 2D model due to the relative stiffness of the sleepers.

### Subgrade

The elastic foundation option used in Chapter 5 for the TMT 2D and 3D models is not available when modelling discrete elements. To create a surface where the stiffness can be applied

(a) 2D example [41].                                    (b) 3D example [22].
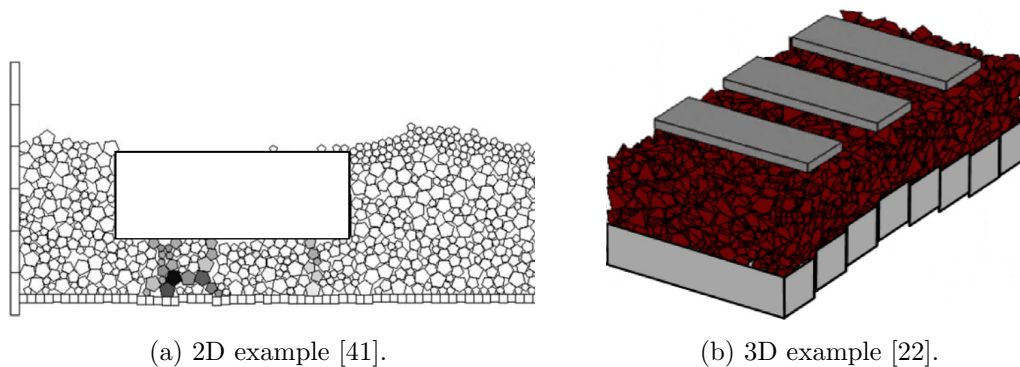
Figure 6.1: Rigid plate subgrade models.

foundation plates are placed below the particles to represent the subgrade surface and to contain the particles. Each plate is a rigid component and only displaces in the vertical direction. A spring stiffness is assigned to the vertical movement of each plate reference point, allowing the subgrade to deform locally. This method has been used in other studies for representing subgrade behaviour [41, 22]. Figure 6.1 shows examples of this subgrade modelling technique.

## 6.2   DEM Particles

Chapter 1 discussed the ballast used in the reference rail structure and in Chapter 3 the element type (PD3D) used during DEM analyses was investigated. This section describes how the ballast behaviour is modelled in Abaqus with PD3D elements. The topics discussed are the interaction and contact between the particle elements which determines the behaviour of the ballasted rail model under loading.

**Particle Interaction and contact**

In Abaqus discrete particles are modelled as rigid elements, but the contact stiffness between the particles can be manipulated to reflect the Hertz contact theory by letting particles overlap each other according to a force-overclosure relation. The following equations are provided to define a force-overclosure relationship between particles [13]:

$$F = \frac{4}{3}E^*\sqrt{R}\sqrt{\delta^3} \tag{6.1}$$

$$R = \frac{R_1 R_2}{R_1 + R_2} \tag{6.2}$$

$$\frac{1}{E^*} = \frac{1 - v_1^2}{E_1} + \frac{1 - v_2^2}{E_2} \tag{6.3}$$

where      $F$  =  contact force [N]

         $\delta$  =  contact overclosure [m]

         $E^*$  =  function of E and $v$
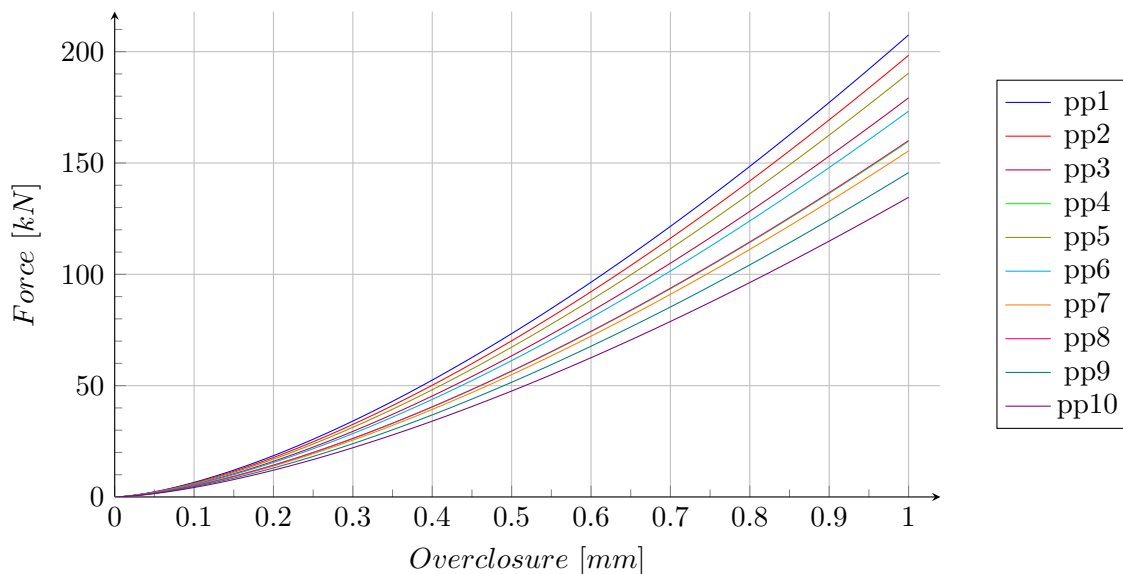
Figure 6.2: Force-overclosure relationships between different particle sizes, 26.5, 37.5, 53 and 63 mm, pp1 - pp10 represent the various relationships between the four different particles sizes.

| | | |
|---|---|---|
| $E_i$ | = | particle Young's modulus (i=1,2) [Pa] |
| $R$ | = | equivalent radius [m] |
| $R_i$ | = | particle radii (i=1,2) [m] |
| $v_i$ | = | particle Poisson's ratio (i=1,2) |

Since the particles are modelled as rigid spheres the contact stiffness, or force-overclosure, in discrete modelling is usually defined to model the physical particle behaviour. Because the contact stiffness is defined in this manner nondefault contact property assignments are commonly used in DEM interactions to achieve the desired physical particle behaviour [12].

When the Young's modulus, Poisson's ratio and particle size values of the ballast used in the reference structure are used in Equations 6.1, 6.2 and 6.3 the force-overclosure relationships shown in Figure 6.2 are obtained for the various particle to particle interactions. Force-overclosure relationship $pp$1 in Figure 6.2 represents the interaction between two particles each with a size of 63 mm, which is the particle size used in the DEM model of the ballasted rail structure.

The coefficient of friction $\mu$ between crushed granite ballast particles is usually between 0.5 and 0.8. A value of 0.6 is a good approximation for general use [1]. In previous research [25, 31] values of 0.5 and 0.8 were used in DEM models of ballast. However, as explained earlier, the particle interaction properties can be adjusted to yield the desired physical behaviour. This is why a reference rail structure is required to calibrate the behaviour of the model. In the following section the ballasted rail model, which is calibrated by comparison to the reference structure, is discussed.

## 6.3  Ballasted Rail Discrete Element Analysis

In this section the DEM 3D model created to analyse the ballasted rail is discussed. The model is described in terms of:

- steps needed to create the model,

- boundary conditions,

- load applications,

- interaction properties,

- modelling simplifications and

- type of analysis performed.

The deformation and deterioration behaviour of ballast is a complex non-linear process. Modelling the full behaviour of the ballast can become time and resource consuming. The aim of this section is to approximate the behaviour of the ballast for only a few (up to four) load cycles, where permanent settlement does not become apparent. This approximation of the ballast behaviour will not include any deterioration or permanent settlement of the ballast. Modelling of the permanent ballast settlement and ballast deterioration is not necessary for a railway section which only consists of a ballasted structure since the rail should have uniform vertical geometry across the section, assuming that subgrade conditions are uniform for the entire section. Figure 6.3 shows the vertical geometry of the reference ballasted structure over a certain distance. The maximum slope of the rail calculated for this geometry is equal to $5.3 \times 10^{-5}$ rad. This is negligibly small when compared to the $0.003$ rad used by Lei and Mao [30], which showed little effect on the vertical accelerations of the rail. However, the uniform vertical geometry assumption at a transition does not represent an accurate representation of the real geometry and will be discussed further in the following chapter. The displacement results of the model are used to calibrate the simplified model used for the ballast behaviour against the reference structure displacement measurements. Results presented for the model are:

- rail and sleeper displacements,

- rail bending moments and

- rail shear forces.

To perform a discrete element analysis on the structure the explicit, dynamic step is used. An implicit, dynamic step will provide the desired results required for this model, as for the TMT model, but particle modelling can only be implemented within the explicit step. Advantages of using the explicit, dynamic analysis is that it [12]:

- is computationally efficient for large models with short dynamic response times and for extremely discontinuous models;
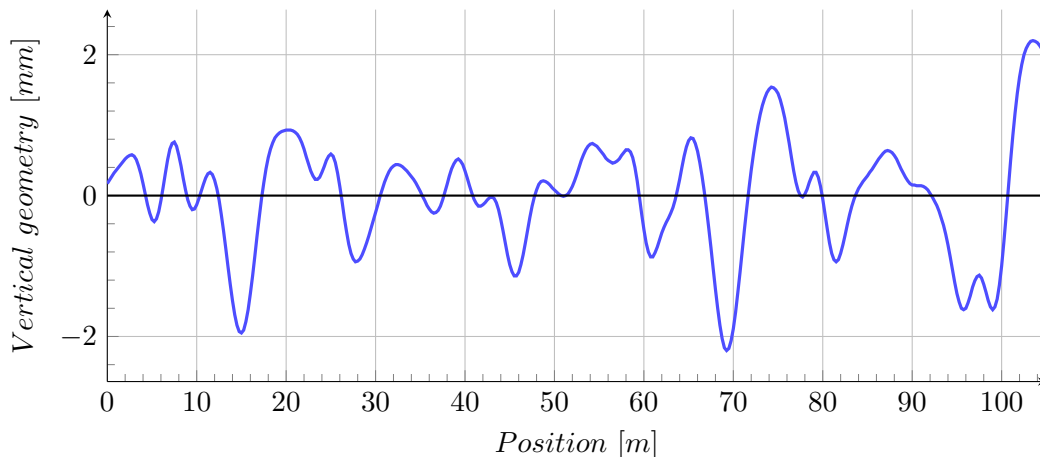
Figure 6.3: Vertical rail geometry of a section of the reference rail.

- allows very general contact definitions such as the interaction between multiple changing contacts between discrete particles; and

- makes use of a consistent, large-deformation theory — large rotations and large deformations are allowed for particle movement.

Abaqus/Explicit uses an explicit central-difference time integration scheme which is computationally inexpensive even for smaller time steps, when compared to the direct-integration dynamic analysis approach used in Abaqus/Standard. This is because there is no solution for the set of simultaneous equations for each increment [12]. The explicit central-difference operator solves the dynamic equilibrium equations at the beginning of the time increment $t$, the accelerations of time $t$ are used to advance the velocity solution to time $t + \Delta t/2$ and the displacement solution to time $t + \Delta t$. The explicit central-difference integration rule is as follows [12]:

$$\dot{u}^N_{(i+\frac{1}{2})} = \dot{u}^N_{(i-\frac{1}{2})} + \frac{\Delta t_{(i+1)} + \Delta t_{(i)}}{2} \ddot{u}^N_{(i)}, \tag{6.4}$$

$$u^N_{(i+1)} = u^N_{(i)} + \Delta t_{(i+1)} \dot{u}^N_{(i+\frac{1}{2})}, \tag{6.5}$$

where $u^N$ is either a displacement or rotation degree of freedom and $i$ refers to the increment number in an explicit dynamics step. $\dot{u}^N$ and $\ddot{u}^N$ are velocity and acceleration values respectively. The central-difference integration operator is explicit because the kinematic state is advanced using known values of $\dot{u}^N_{(i-\frac{1}{2})}$ and $\ddot{u}^N_{(i)}$ from the previous increment [12].

The explicit integration rule is simple, but is not the only aspect that makes the explicit dynamics step such a simple step. Another aspect to the simplicity of the explicit dynamics step is the use of diagonal element mass matrices because the accelerations at the beginning of each increment is calculated by:

$$\ddot{u}^N_{(i)} = (M^{NJ})^{-1}(P^J_{(i)} - I^J_{(i)}), \tag{6.6}$$

where $M^{NJ}$ is the mass matrix, $P^J$ is the applied load vector and $I^J$ is the internal force vector. The reason for using a lumped mass matrix is because of the simplicity of calculating the inverse of the mass matrix of the system and because vector multiplication of the inverse of the mass
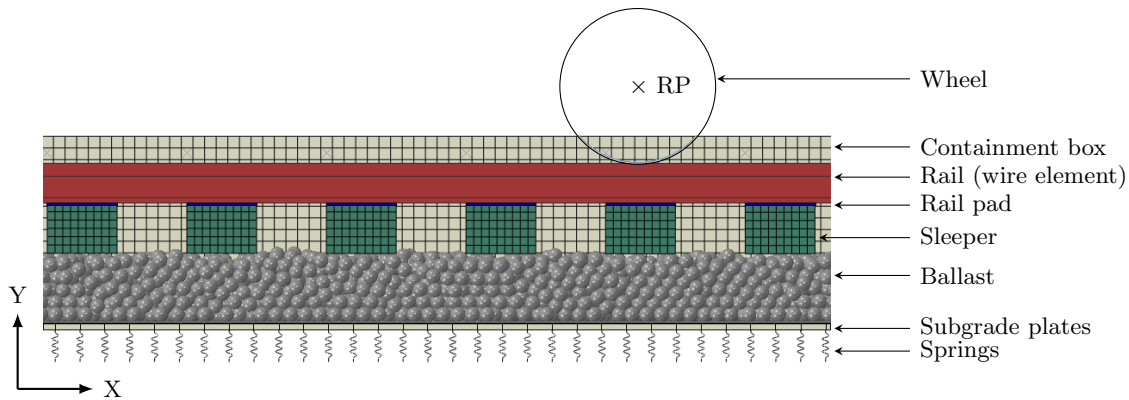
Figure 6.4: Ballast DEM model components.

matrix by the inertial force only requires $n$ operations, with $n$ equal to the number of degrees of freedom in the model. No iterations and no tangent stiffness matrix is required for the explicit step. $I^J$ is assembled from contributions from the individual elements so that a global stiffness matrix is not required [12].

The reason for not using this seemingly inexpensive analysis procedure for the other models analysed in this study is that various modelling techniques that can simplify the model, for example the elastic foundation interaction option, are not available in Abaqus/Explicit and DEM modelling is not available in 2D, preventing the simplification of the DEM 3D model to a DEM 2D model.

### 6.3.1 Static 3D Model

A section of the static ballast DEM 3D model is shown in Figure 6.4 on which all the components of the assembly are shown. In the assembly there are two wheels which are placed in the symmetrical load configuration used for the static loading of the structure, the same load configuration used for the static TMT model. The containment box, which contains the particles in the lateral directions does not have a base or a top. The box has length, height and depth dimensions of $9\,845\,mm$, $800\,mm$ and $1\,600\,mm$ respectively. An Abaqus FEM 2D beam component with the UIC60 rail profile models the rail in the three-dimensional space. Rail pads are placed in-between the rail and sleepers, covering the contact areas between the rail and each sleeper. The sleeper cross-section is simplified from the complex cross-section, as used in the reference structure, to a rectangular shape $300\,mm$ wide and $214\,mm$ high to simplify modelling. The subgrade plates are $1\,600\,mm$ long and $150\,mm$ wide and are connected to springs, with a stiffness of $0.025\times10^6\,N/mm$, that model the subgrade.

Creating a DEM model is more complex than creating a FEM model. DEM elements have to be created manually in the input file because they are not available in Abaqus/CAE modelling software with a graphical user interface. Extra analysis procedure steps need to be performed to let the particles settle to their desired positions. To begin a DEM model a 3D solid part is created in Abaqus/CAE and is meshed to provide the amount of nodes required for the

Table 6.1: Particle interaction properties.

| Particle interaction with | Normal contact stiffness $[\times 10^6 \text{ N/mm}]$ | Friction [-] |
|---|---|---|
| Box | 0.05 | 0.5 |
| Sleepers | 0.05 | 0.5 |
| Particles | 1.00 | 0.8 |
| Subgrade plates | 0.05 | 0.8 |

particles. Each node is equal to a particle and the solid mesh should be coarse enough to ensure that the particles do not overlap when the analysis starts. After the input file has been written for the solid part mesh the input file must be edited to change all solid elements to PD3D particle elements. The particles can only be seen in Abaqus/Viewer after the analysis has been performed.

Since the particles originate from a solid part mesh they are generally created in a grid pattern as shown in Figure 6.5a. After creation the particles have to settle to their desired positions (Figure 6.5b), they settle at no inter-particle friction and a higher gravity load. Without friction and with higher gravity the particles compact under their own weight [31]. After settlement of the particles has been completed the friction is increased and the gravity reduced to normal. The sleepers, rail and wheels can now settle onto the ballast (Figure 6.4), where after a distributed line load is applied to the rail to push the sleepers into the particles (Figure 6.5b) and compact the particles further.

In preliminary DEM models it was found that incorporating the different particle sizes (ballast grading) causes the particles to scatter when interacting with each other and not converge to a static position. To avoid particles scattering only a single particle size is used in the DEM model. The interaction properties in Table 6.1 and the following parameters were used for the particle elements:

- Relative density = 2.83

- Particle diameter = 63 mm

- Mass proportional damping factor = 7.5

- Number of particles = 30 000

The mass proportional damping value of 7.5 was taken from a DEM example in the Abaqus Example Problems Guide [13]. Mass proportional damping helps to minimize particle scattering. The interactions between the finite element components are summarized in Table 6.2. For the wheel-rail interaction separation of contact and no friction allows the wheel to glide smoothly over the rail as if it where rolling and the hard pressure-overclosure definition allows no penetration between the components. The no separation option can only be used if the friction value is set to rough, this combination will not allow separation of the interacting components after contact has been initiated. Since the rail fasteners are not modelled to connect the differ-
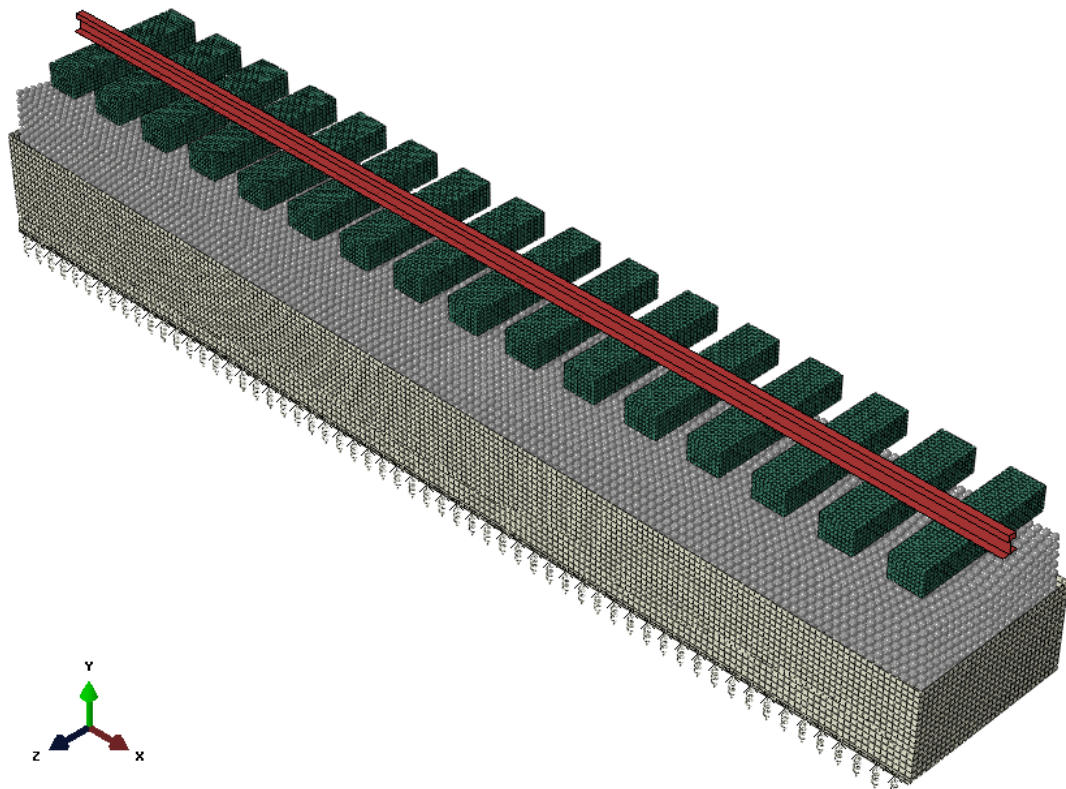
(a) Initial component layout before settlement occurs.
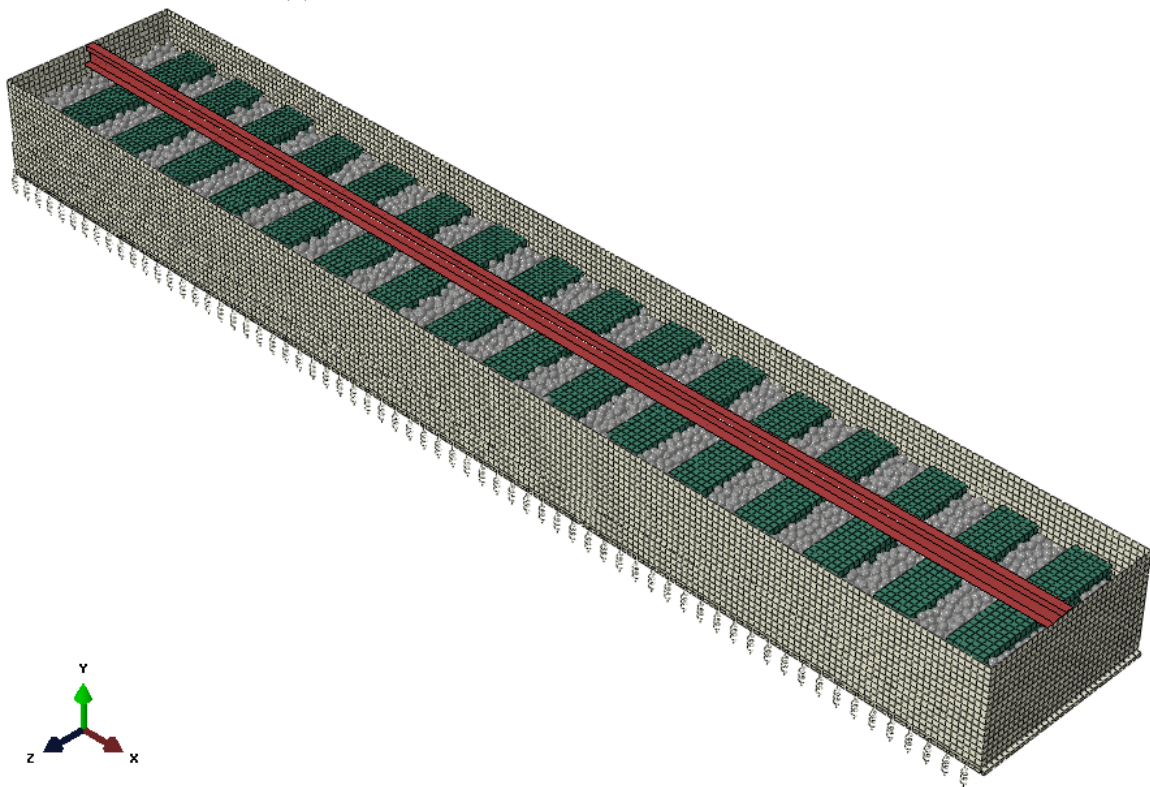


(b) Final component layout, sleepers pushed into particles after load application.

Figure 6.5: Steps followed to create the DEM model of the ballasted rail section.

Table 6.2: Finite element interaction properties.

| Interaction | Friction [-] | Pressure-overclosure | Contact release |
|---|---|---|---|
| Wheel-rail | 0.0 | Hard | Yes |
| Rail-Rubber | Rough | Hard | No |
| Rubber-sleeper | Rough | Hard | No |

ent components to each other the no separation option performs the role of the rail fasteners between the rail and the sleepers.

Boundary conditions are applied to the wheels and only allow vertical ($y$) displacements. The rail is constrained at its ends by longitudinal symmetry boundary conditions ($x - symm$) and the sleepers are constrained by lateral symmetry boundary conditions ($z - symm$) on their symmetry cut ends. The particles have no boundary conditions, they are only constrained by the containment box and subgrade plates. The containment box is constrained in all directions and the subgrade plates are constrained in all directions except the vertical direction ($y$) which is constrained by the springs modelling the subgrade stiffness.

An explicit analysis is performed on the model with a stable time increment of $1.0 \times 10^{-6}$ seconds to provide the results shown in the following section. This small time step is used to prevent particles from excessive penetration and scattering and is well below the recommended time step for finite elements.

### 6.3.2   Static 3D Model Analysis Results

The results of the ballasted rail static DEM 3D model as described above are presented in this section. Results presented here are the rail and sleeper displacements and rail shear forces and bending moments. The results obtained did not show the expected behaviour of the ballasted structure. This could be caused by limitations in the software with respect to the ballast material modelling and the analysis process using DEM behaviour, preventing the analysis process to reach convergence and yield plausible results.
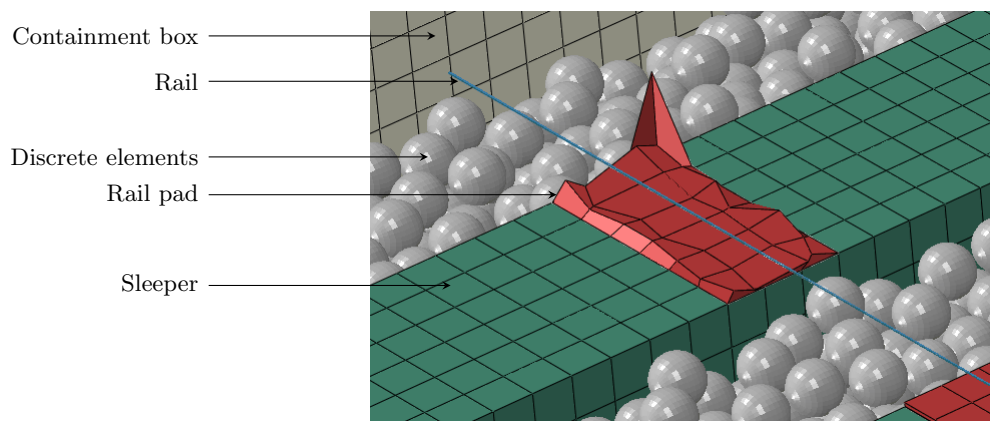


Figure 6.6: Excessively distorted rail pad.

A convergence error within the first rail pad, at $x = 0.3$ m, terminates the analysis procedure and creates excessive distortion in the rail pad and the excessively distorted rail pad applies localised contact forces to the rail, creating irregularities in the rail results. Figure 6.6 shows the distorted rail pad. The Abaqus Example Problems Guide [13] provides an example of a DEM model, but the example does not contain any deformable elements. Limited assistance is available on DEM modelling in Abaqus, because it is a new introduction to the software. Since it falls outside of the scope of this study to resolve issues within the new DEM software the obtained results are merely presented for future reference. A report on this problem area in the software used will be submitted to the vendor in due course.

### Displacements

The displacement results for the sleepers and rail of the static DEM 3D model are shown in Figure 6.7. The maximum deflection at the centreline of the rail is -1.4 mm and the maximum sleeper deflection is -0.925 mm. The spike in rail displacement measurements at $x = 0.3$ m is caused by the distorted rail pad.

### Bending moments

Figure 6.8 shows the bending moments that occur in the rail for the statically loaded model. The maximum and minimum bending moments in the rail are 11.9 kN.m and -6.52 kN.m respectively. The bending moment distribution also shows the influence of the excessively distorted rail pad at $x = 0.3$ m. Because the bending moments are calculated by the second derivative of the displacement ($M = \frac{d^2 w}{dx^2}$) the results are less smooth and the spike is exaggerated.

### Shear forces

The maximum shear force in the rail is 59.4 kN. Figure 6.9 shows the shear force distribution in the rail. Shear forces are calculated by the third derivative of the displacement ($V = \frac{d^3 w}{dx^3}$) showing more "noise" than the bending moment distribution and the spike at $x = 0.3$ m becomes greater.

## 6.4 Simplified Ballasted Rail Finite Element Analysis

Modelling the ballasted rail as a DEM 3D model provides difficulties such as:

- DEM model creation is time consuming and complex due to the involved method of creating particles and particle settling;

- long analysis times — even though the explicit analysis method is effective, DEM analyses require full 3D models which take longer to analyse than simplified 2D models;
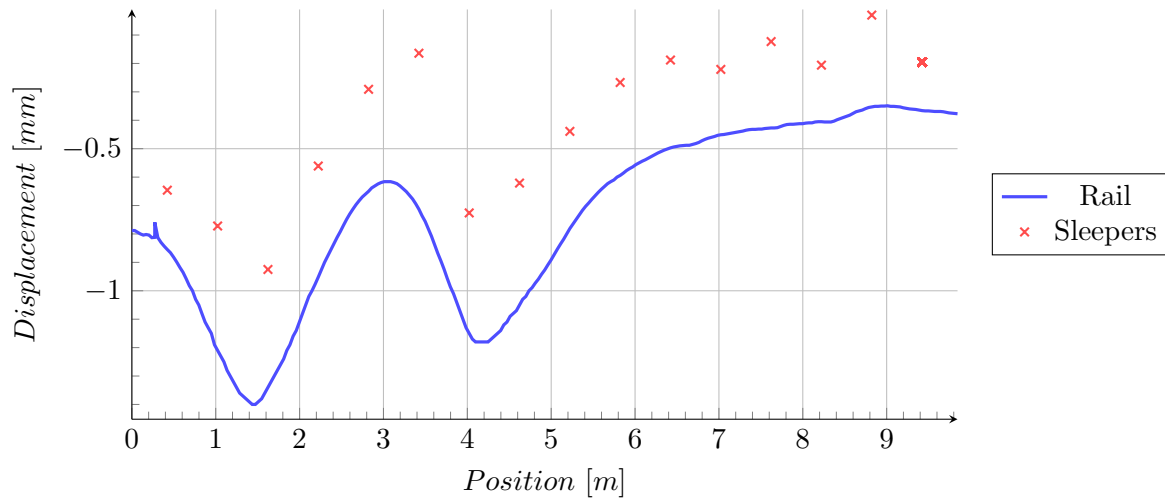
Figure 6.7: Static DEM 3D model vertical displacements.
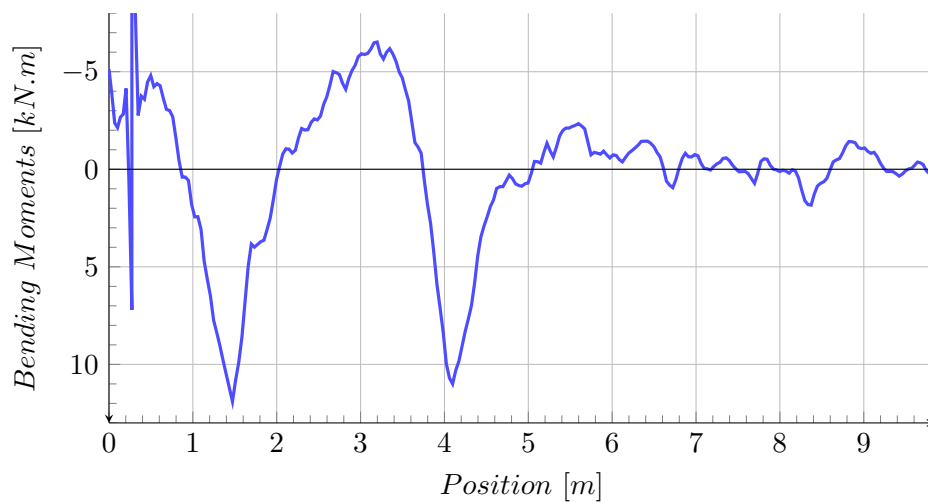


Figure 6.8: Static DEM 3D model bending moment distribution.
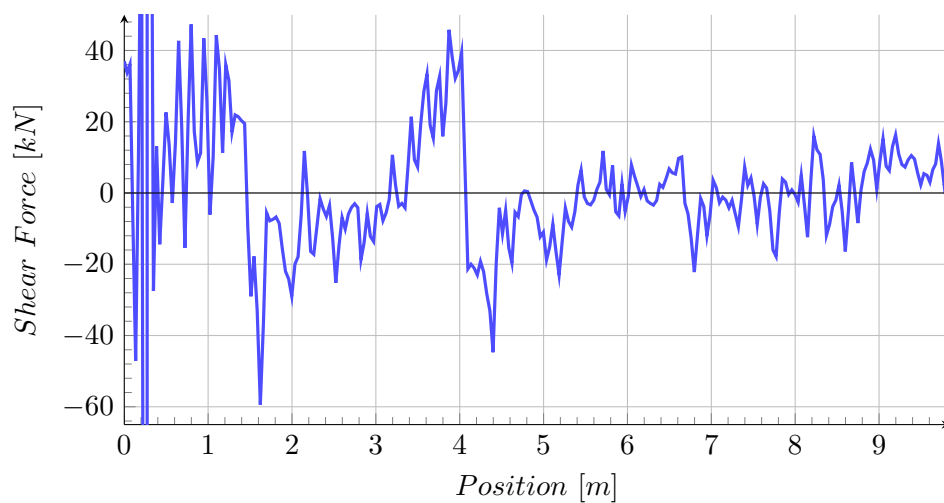


Figure 6.9: Static DEM 3D model shear force distribution.
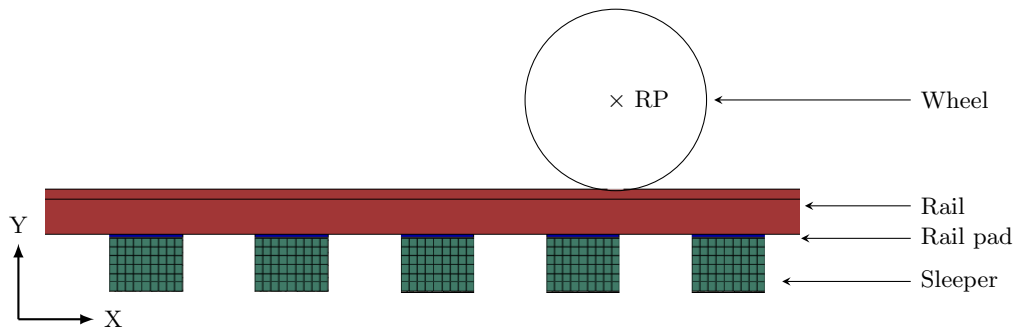
Figure 6.10: Section of the simplified ballast 2D model.

- inadequate compatibility between FEM and DEM — there are interaction difficulties between deformable FEM components and discrete particles;

- some modelling capabilities in Abaqus/Standard which help simplify the models, such as the elastic foundation option, are not available in Abaqus/Explicit; and

- if the ballast is modelled with discrete particles the transition model in the following chapter has to be modelled in 3D in Abaqus/Explicit, which will be complex, time consuming and computationally expensive.

By simplifying the DEM 3D model to a FEM 2D model the computational time and effort are greatly decreased and the extraction of results becomes more simplified. This section investigates the simplification of the DEM 3D model to a FEM 2D model; discusses the results obtained for the FEM 2D model; and compares the 2D results and reference rail measurements for calibration.

### 6.4.1  Static 2D Model

The simplified model of the ballasted rail only contains the wheels, rail, rail pads and sleepers, as seen in Figure 6.10. The ballast and subgrade are incorporated into the elastic foundation stiffness which is applied to the bottom of the sleepers. The elastic foundation stiffness is equal to $0.58\,\text{N/mm}^3$, which was calibrated by comparing the displacement measurements performed by P.J. Gräbe on the reference rail to the ballast 2D model displacement results. The elastic foundation stiffness is applied to the area below each sleeper, which has half the length of a sleeper in the z-direction, because of symmetry. When consulting the reference rail displacement measurements in Figure 6.15 the ballast and subgrade are seen to behave nearly elasticly and ballast settlement or deterioration ("plastic" behaviour) does not become apparent. The elastic behaviour of the reference structure displacements and the investigated Winkler [16] elastic foundation theory support the use of springs to model the ballast and subgrade.

The wheels and rail remain the same as in the 3D model, but are constrained to the 2D, $x - y$ plane. Plane stress elements are used for the rail pads and the sleepers are modelled with deformable, plane strain elements due to their length to width ratio.

Boundary conditions are applied to the rail ends, modelling the longitudinal symmetry ($x-$ $symm$) of the rail, and to the wheel reference points to prevent out of plane rotation. The two wheel loads are applied the same as in the static DEM 3D model, in the symmetry load positions. Vertical constraints are applied to the model via the elastic foundation. The static, general step is used to perform the static analysis of the ballasted rail model to yield the results shown below.

### 6.4.2   Static 2D Model Analysis Results

Results for the simplified ballast rail 2D model under static load conditions are shown in this section. Displacements, bending moments and shear forces are plotted for the rail and the displacement of the sleepers is plotted. These results are used to calculate the DAF when compared to the dynamic 2D model.

**Displacements**

Figure 6.11 shows the vertical displacements of the rail centreline and the sleepers for the statically loaded, simplified 2D model. Much of the rail displacement occurs due to the compression of the rail pads. This can be seen from the difference in maximum displacements between the rail and sleeper. The maximum rail deflection is -0.375 mm and the maximum sleeper deflection is -0.202 mm.

**Bending moments**

Bending moments that occur in the rail are shown in Figure 6.12. The maximum moment present in the rail is 10.7 kN.m and the minimum moment in the rail is -4.16 kN.m.

**Shear forces**

Figure 6.13 shows the shear force distribution for the rail. The step-wise shear force distribution in the rail is caused because the rail is only supported intermittently by the sleepers. The maximum shear force occurring in the rail is equal to 31.40 kN.

### 6.4.3   Dynamic 2D Model

The simplified, dynamic 2D model is similar to the static model, except for the wheels which traverse the rail to simulate train movement, similar to the wheels in the TMT model, and boundary conditions which are only applied to the rail ends for analysis stability. A dynamic, implicit step is used with quasi-static load application, no material damping applied and automatic time increments. This described model set-up yields the results presented in the section below.
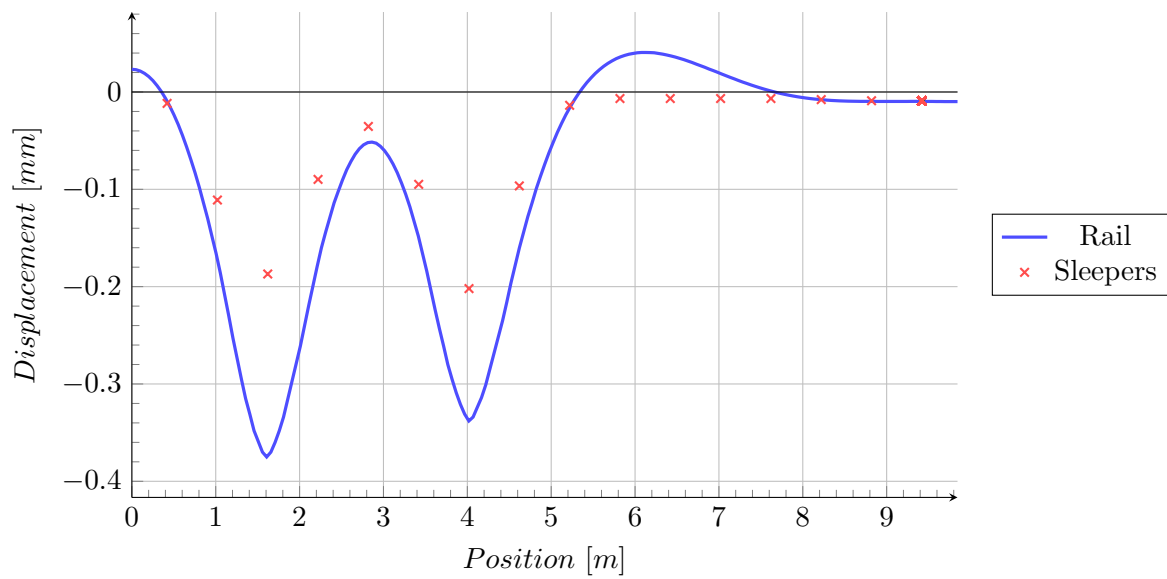
Figure 6.11: Static 2D model vertical displacements.
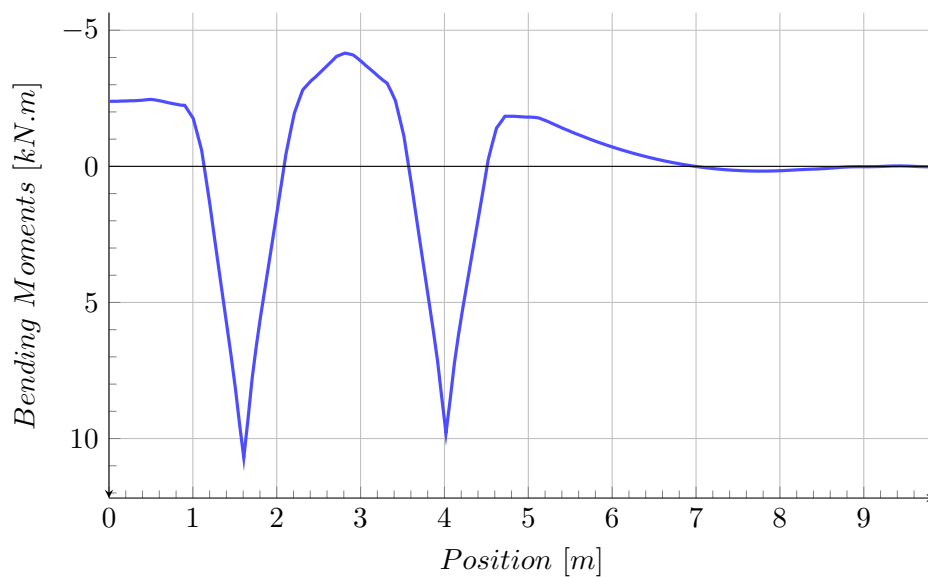


Figure 6.12: Static 2D model bending moment distribution.
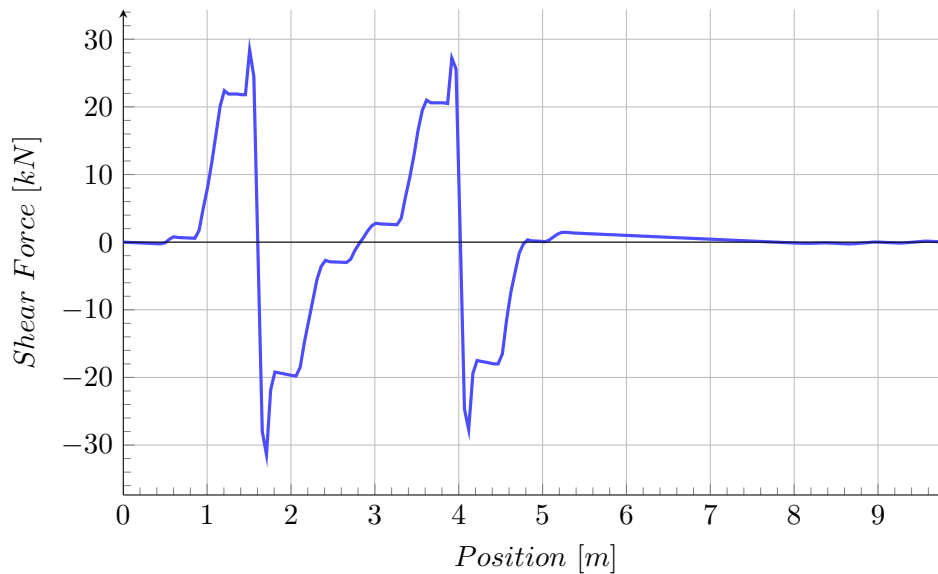
Figure 6.13: Static 2D model shear force distribution.

### 6.4.4   Dynamic 2D Model Analysis Results

Results for the simplified, ballast rail 2D model under dynamic load conditions are discussed here. The bending moment and shear force results are presented at time t = 0.1554 s when loading is similar to the static load geometry. Displacement results are shown over the time period it takes the wheels to traverse the whole length of the rail for a sleeper node and a rail node in the middle of the model in order to avoid as much of the boundary effects as possible. The displacement results are used to compare to the reference structure measurements. With the simplified 2D model the frequency analysis is available to perform the modal analysis of the structure; a modal analysis is not available in Abaqus/Explicit for the DEM model. Results of the modal response analysis of the structure are shown for two mode shapes: the first mode of vibration and a higher mode of vibration.

**Modal response**

Frequencies of 147.15 Hz and 154.87 Hz for modes one and five respectively were extracted from the frequency analysis of the structure. The mode shapes are shown in Figure 6.14. The frequencies of the ballasted rail structure are higher than the excitation frequencies (2.257 - 17.094 Hz) and no resonance is expected in the structure.

**Displacements**

The vertical displacement response of the rail and sleeper are shown in Figure 6.16. Along the centreline of the rail the maximum displacement is -0.39 mm and the maximum sleeper deflection is -0.21 mm. Figure 6.15 shows the displacement measurement data (by P.J. Gräbe) of the reference ballasted rail for four points on the rail, each point above a sleeper and with
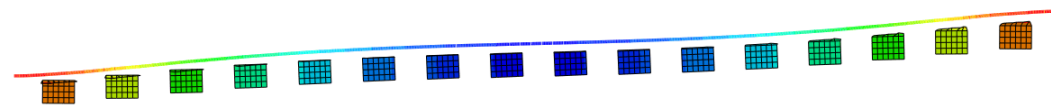
Mode 1 Frequency = 147.15 Hz.
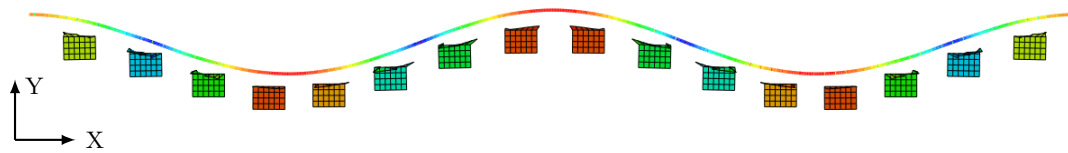
Mode 5 Frequency = 154.87 Hz.

Figure 6.14: Mode shapes.

three sleeper spacings between each point. The points on the rail were measured with different video resolutions. Measurement point B1 had the lowest resolution and point B3 the highest resolution and B3 provides the best fit to the model displacement data, which can be seen by comparing the displacement curve for B3 in Figure 6.15 to the rail displacement curve in Figure 6.16. The maximum deflection at the reference rail is equal to -0.41 mm for point B1. For calibration of the sleeper deflections the sleeper below point B3 was measured, it has a maximum deflection of -0.22 mm and is shown as B3-sleeper in Figure 6.15.

Through comparison of the static and dynamic sleeper displacements the DAF is calculated. With a maximum static deflection of -0.16 mm (Figure 6.11) and a maximum dynamic deflection of -0.21 mm (Figure 6.16) the DAF equates to 1.3.

**Bending moments**

Bending moments occurring in the rail are shown in Figure 6.17. The maximum moment present in the rail is 11.8 kN.m and the minimum moment in the rail is -6.25 kN.m.

**Shear forces**

Figure 6.18 shows the shear force distribution for the rail. Again the step-wise shear force distribution is noticed due to the intermittent sleeper support. The maximum shear force in the rail is 43.20 kN.

## 6.5   Summary

The objective of this chapter was to investigate an effective and accurate model for a ballasted rail. To ensure accurate modelling the different element types and modelling methods used in this chapter were investigated. The PD3D particle element type and the subgrade modelling
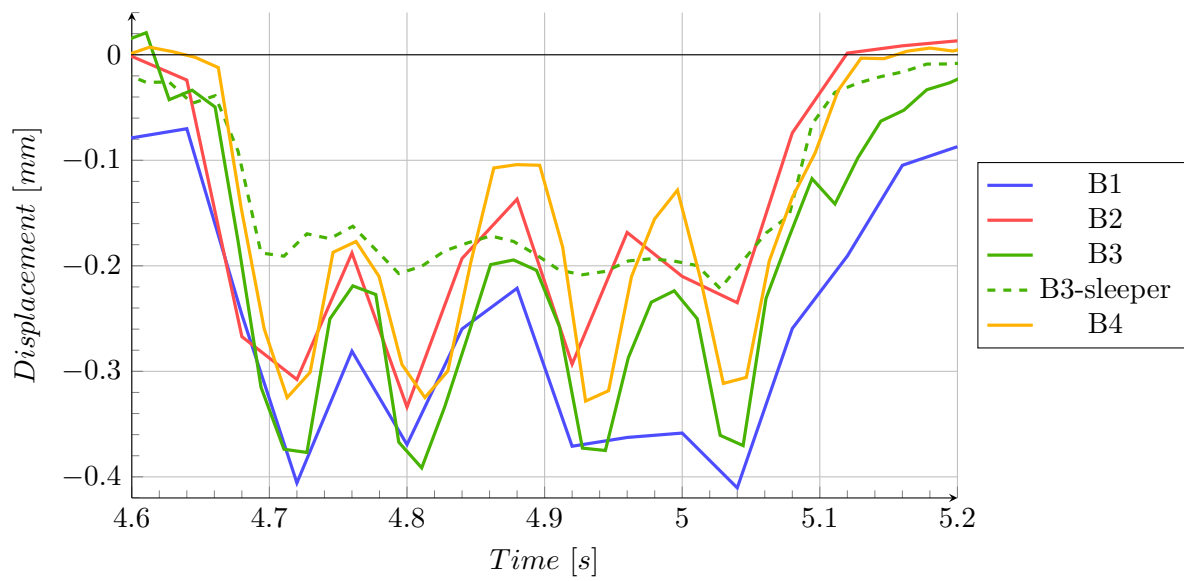
Figure 6.15: Reference rail vertical displacement measurement data.
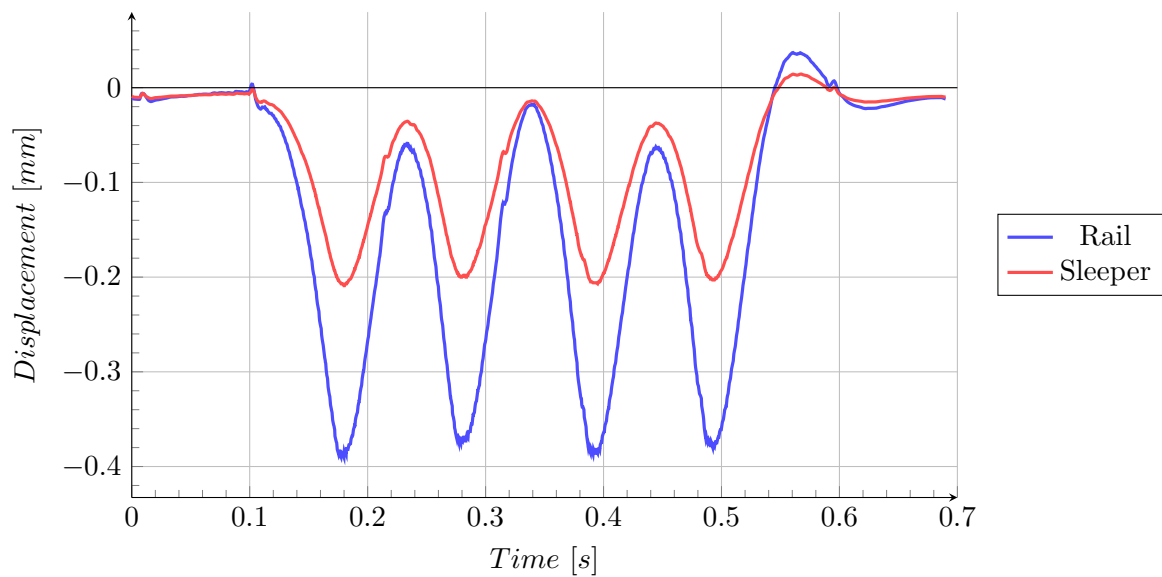


Figure 6.16: Dynamic 2D model time history of vertical displacement response.
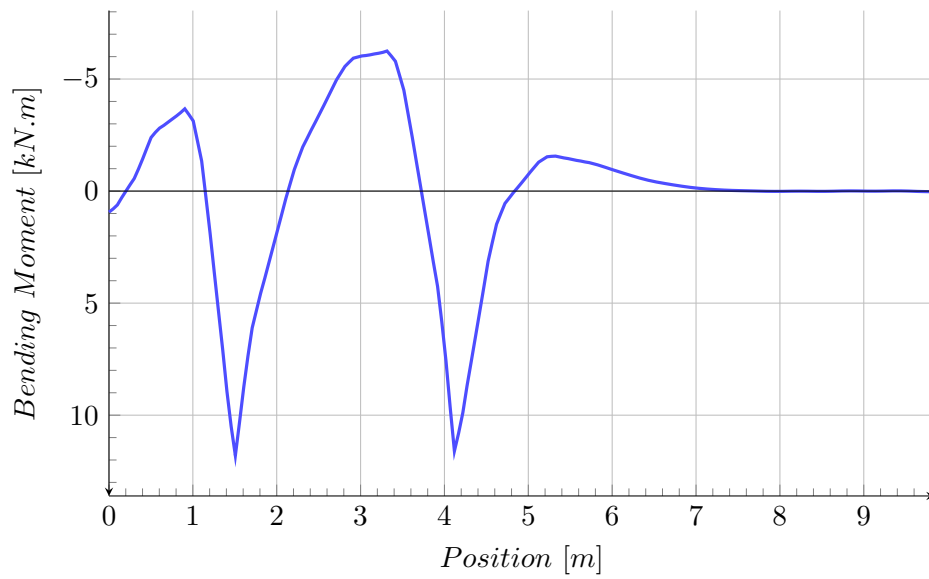
Figure 6.17: Dynamic 2D model bending moment distribution.
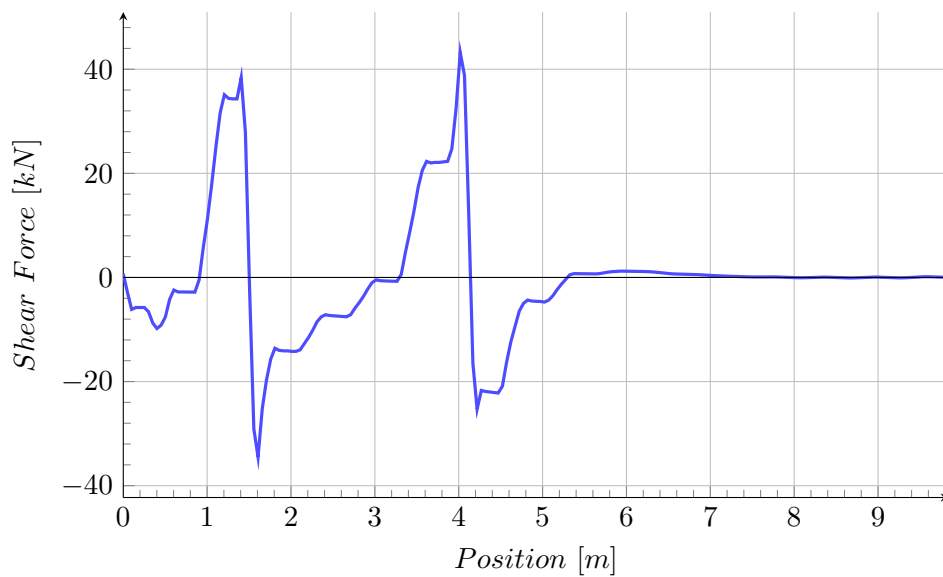


Figure 6.18: Dynamic 2D mode shear force distribution.

technique are important for the creation of the DEM 3D model. The subgrade was modelled as multiple plates [41, 22] with vertical stiffness values of $0.025 \times 10^6$ N/mm (the stiffness of the TMT model subgrade) assigned to each plate via springs. The interaction and contact modelling between PD3D particles was investigated. Interaction properties of the particles can be calculated with equations provided in the Abaqus User's manuals [12], but in DEM modelling the interaction properties are usually adapted to ensure accurate physical particle behaviour. To model the physical behaviour of the particle elements a contact stiffness of $1.0 \times 10^6$ N/mm and a friction coefficient of 0.8 was used.

A DEM 3D model can become very complex and cumbersome. To avoid this some simplifications were made such as, a single particle size was used, no particle clumping was used and the sleepers were modelled as rigid components. When using multiple particle sizes convergence issues occurred and the particles scatter, not converging to a static position. Deformable sleepers showed severe mesh distortions when interacting with particle elements. Even though these simplifications were made it remains a complex procedure to create the particles, allow proper settlement and define the correct interaction between the particles and other components. The rail pads were modelled as deformable components and showed severe mesh distortion, preventing the analysis from completing. Since it is outside the scope of this study to resolve issues found with modelling DEM in the software the results obtained were presented merely for future reference and can not be compared to the results of the simplified 2D models. To simplify the ballast model for use in the transition model a FEM 2D model was created to model the ballasted rail.

Modelling the ballast and subgrade in the 2D model was done by replacing the ballast and subgrade with an elastic stiffness of $0.58$ N/mm$^3$ which allows similar deflections in the rail when compared to the deflections measured on the reference structure. Both a static and dynamic analysis was performed on the 2D model to allow the calculation of the DAF. By using the maximum deflections of the sleepers the DAF was calculated as 1.03, for a travelling speed of 94 km/h. The dynamic results are similar to the static results due to the low masses and no damping included in the models, which result in quasi-static behaviour of the dynamic model. To calibrate the 2D model the maximum rail deflection of -0.41 mm and -0.22 mm sleeper deflection measured on the reference structure was used as conservative measurements. The 2D model maximum rail deflection is -0.39 mm and the maximum sleeper deflection is -0.21 mm which is within an acceptable 5 % of the reference structure deflections. A summary of the results obtained for the models analysed in this chapter and the previous chapter is shown in Table 6.3. The table includes results of the TMT structure from the previous chapter to allow a comparison between the TMT and ballasted structures.

Table 6.3: Ballasted rail and TMT results summary.

|  |  | Maximum Displacement [mm] | Maximum Bending Moment [kN.m] | Minimum Bending Moment [kN.m] | Maximum Shear Force [kN] |
|---|---|---|---|---|---|
| TMT | 3D stat | 0.79 (0.65) | 8.53 (9.11) | -1.92 (-6.37) | 43.85 (15.97) |
|  | 2D stat | 0.78 (0.68) | 8.10 (9.72) | -1.94 (-6.96) | 39.06 (18.28) |
|  | 2D dyn | 1.09 (0.93) | 10.20 (12.60) | -3.86 (-6.03) | 49.96 (20.10) |
| Ballast | 3D stat | 1.40 (0.93) | 11.9 | -6.52 | 59.40 |
|  | 2D stat | 0.38 (0.20) | 10.7 | -4.16 | 31.40 |
|  | 2D dyn | 0.39 (0.21) | 11.8 | -6.25 | 43.20 |

*Results in parentheses for the TMT results are RC beam results and results in parentheses for the ballast results are sleeper displacements.

# Chapter 7

# Ballast to TMT Transition Analysis

In this chapter the combination of the TMT 2D model and ballasted rail 2D model, to create the ballast-TMT transition model, is described. It is determined whether the method of modelling a transition with simplified 2D models is an accurate approach by comparing reference displacement measurements of a ballast-Sonneville transition to an Abaqus calibration model. At the transition between the ballast and TMT structures the structural behaviour due to dynamic loading is investigated and the results obtained are presented in a sensitivity analysis. The model description and results discussion are done for various transition models with different train speeds and rail irregularity angles to determine the sensitivity of the TMT structure, specifically the RC beam, with respect to the variables at a rail transition.

## 7.1   Dynamic Transition 2D Models

The models investigated in this section are a calibration model of the ballast-Sonneville reference transition and various ballast-TMT transitions. The calibration model simulates the ballast-Sonneville reference transition under the geometry and loading conditions of the structure at the time of the reference displacement measurements. Results shown for the calibration model are the maximum displacements at similar locations as used on the reference transition structure. The maximum displacements measured on the reference transition are also shown for a comparison between the reference and calibration displacements. Time histories of the reference rail and the calibration model are also shown. The different ballast-TMT transition models, created after the ballast-Sonnevile model has been calibrated, have train speeds and irregularity angles varying between 40 - 250 km/h and 0 - 0.012 rad respectively. Results of the ballast-TMT models are presented in the form of a sensitivity analysis for the maximum displacements, maximum and minimum bending moments and the absolute maximum shear forces in the RC beam.

99

(a) Constructed track [47].

(b) Track components [47].
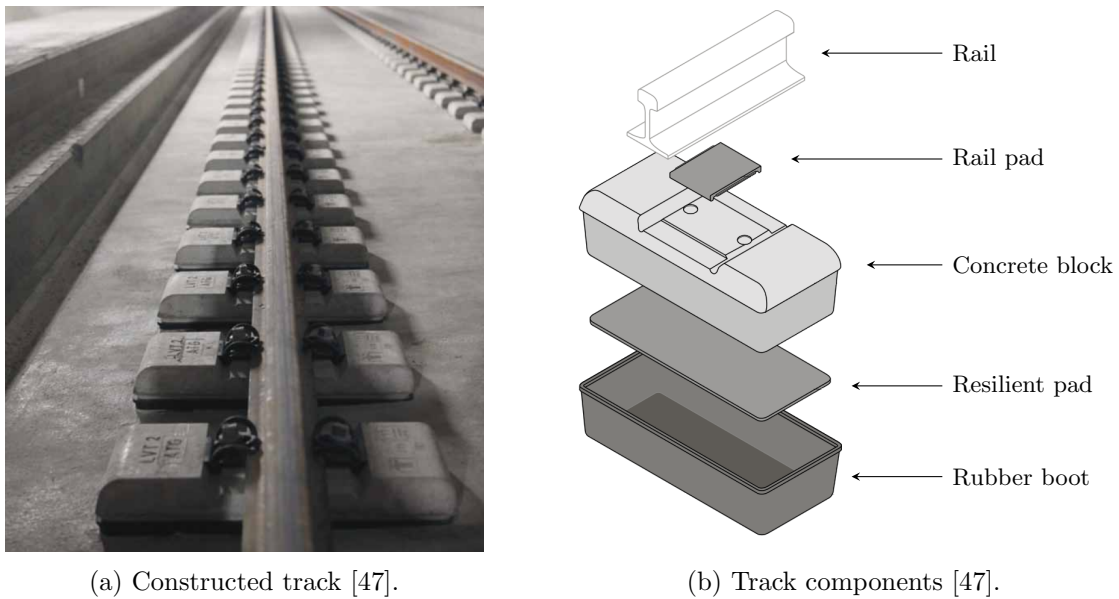
Figure 7.1: Sonneville track system.

### 7.1.1 Ballast-Sonneville Transition Calibration Model

The calibration model is created to allow a comparison with the reference ballast-Sonneville transition. The comparison is made to determine whether modelling the transition with simplified 2D FEM models will yield results which are representative of the rail behaviour at a transition.

Sonneville track is the track system used in the reference transition. The system rests the rail on a rail pad, which is placed and fixed on top of a concrete block; the concrete block rests on a resilient pad and is placed within a rubber boot, which is cast into unreinforced concrete. Figure 7.1b shows the component assembly of the Sonneville track system. The concrete blocks have a cross-section of 264 mm by 205 mm and a length of 640 mm with 12 mm thick pads of $0.025{\times}10^6$ N/mm stiffness below them. The unreinforced concrete spans the length of the rail, has a cross-section width of 3 800 mm and is 50 mm thick below the rubber boots [47]. Figure 7.1a shows a rail using the Sonneville track system.

The reference transition contains a transition zone in the form of an approach slab. An approach slab is a sloped concrete slab placed below the ballast at the transition from ballast to track. The transition zone is indicated in Figure 7.2, but the approach slab is not included in the model since a difference in vertical track stiffness has minimal effect on the response of the rail at a transition [30]. Varying vertical track geometry, caused by permanent ballast settlement and ballast deterioration, is another aspect of rail transitions which is visible at the reference transition. The approach slab and ballast settlement and deterioration creates varying vertical geometry of the sleepers at the transition. This varying vertical geometry is applied to the model by vertically translating the sleepers in the calibration model until the results are comparable to the reference measurements, shown in Figure 7.3.

The calibration model of the ballast-Sonneville transition is analysed with an implicit, dynamic
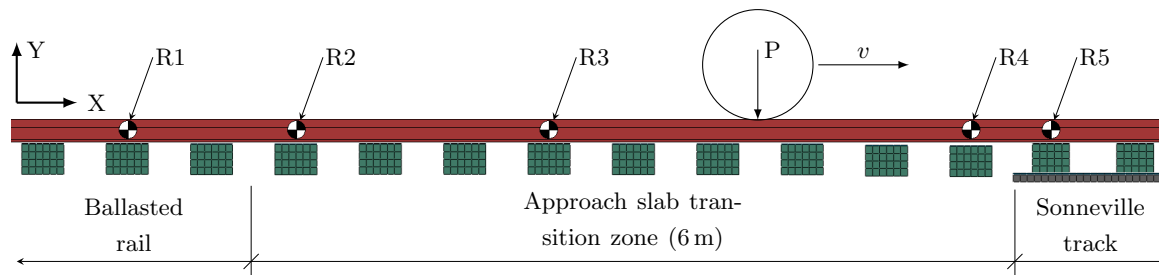
Figure 7.2: Section of the ballast-Sonneville transition calibration model with reference measurement points (R1-R5) shown.

step which is applied for quasi-static behaviour and automatic time increments are used. Components of the assembly are the four wheels, rail, rail pads, sleepers, and the Sonneville concrete blocks, rubber pads and concrete slab. All the components of the assembly are shown in Figure 7.2. The reference measurement points on the rail are also indicated in Figure 7.2. The foundation stiffness values are applied with the elastic foundation option to the base of the sleepers and the Sonneville slab. The ballast and ballast subgrade has a combined foundation stiffness of $5.8\,\mathrm{N/mm^3}$, the same as the ballasted model subgrade in Section 6.4, and the Sonneville subgrade has a stiffness of $0.1043\,\mathrm{N/mm^3}$, the same as the TMT subgrade in Section 5.4. The only boundary conditions are applied to the rail ends for analysis stability and wheel loads of $78.48\,\mathrm{kN}$ are applied to the rail at a speed of $94\,\mathrm{km/h}$. The length of the entire calibration model is $26\,\mathrm{m}$, which consists of a $10\,\mathrm{m}$ ballasted rail section, a $6\,\mathrm{m}$ transition zone section and a $10\,\mathrm{m}$ Sonneville track section.

### 7.1.2 Transition calibration model displacement results

For the calibration model the main focus is on the displacements at the reference measurement points. Figure 7.3 plots the maximum displacements measured at each point for both the reference transition and the calibration model. The maximum error between two similar measurement points is $4.6\,\%$ at point R5 and the maximum displacement seen at the transition is $3.9\,\mathrm{mm}$ at R4, as seen in Table 7.1. These results show that it is possible to model a transition with simplified 2D FEM models and that the geometry of the model can be manipulated to fit to any settled geometry of the sleepers at a transition. The position of the sleepers at the transition can be manipulated to achieve the desired displacement results since the settlement of sleepers at a transition are what create the increased displacements. The supporting stiffness below the sleepers from the subgrade and ballast is assumed to remain the same as determined for the ballasted rail model in Section 6.4. The possible vertical track stiffness increase from the transition slab is not included in the model. It is expected that the ballasted rail will have larger displacements than the slab track, but due to the rail pad, resilient pad and rubber boot shown in Figure 7.1b the Sonneville track system has larger displacements than the ballasted rail. Figure 7.4 plots the time histories of the measured data for the reference rail against the time histories of the calibration model. The calibration model gives a good representation of the reference rail displacements when comparing maximum displacements. The reason that the

reference displacements do not show the passing wheel loads as clearly as the calibration model is due to the low frequency at which displacement measurements were made on the reference rail.
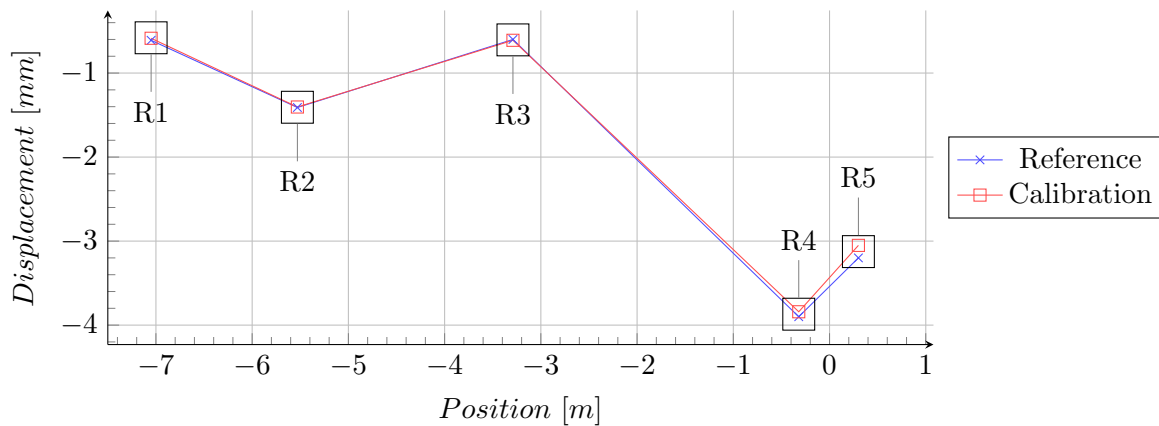


Figure 7.3: Reference transition maximum vertical displacements plotted against maximum vertical displacements calculated with the Abaqus calibration model with position measured from the edge of the Sonneville concrete slab.

Table 7.1: Summary of reference transition and calibration model maximum vertical displacements and errors at measurement points R1-R5.

|                                  | R1   | R2   | R3    | R4   | R5   |
|----------------------------------|------|------|-------|------|------|
| Reference displacements [mm]     | 0.61 | 1.41 | 0.60  | 3.90 | 3.20 |
| Calibration displacements [mm]   | 0.59 | 1.40 | 0.61  | 3.84 | 3.05 |
| Error [%]                        | 3.28 | 0.71 | -1.70 | 1.54 | 4.60 |
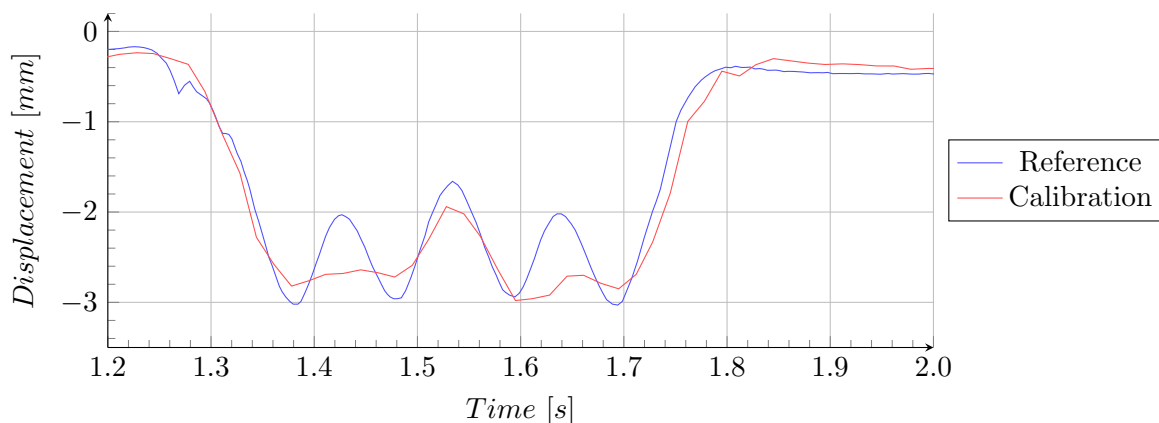


Figure 7.4: Rail vertical displacement time histories at point R5 for the reference rail and the Abaqus calibration model.

### 7.1.3  Ballast-TMT Transition Models

A model of the ballast-TMT transition is created by combining the separate 2D models created for the ballast (Chapter 6) and TMT (Chapter 5) rail structures, with the rail continuous over both models. As mentioned in Chapter 2 the irregularity angle of the rail, which occurs due to

permanent vertical settlement, has a greater contribution to the dynamic behaviour of the rail than the difference in stiffness between the supporting structures has, the difference in vertical track stiffness has negligible effect on the behaviour of the transition [30]. With no vertical geometry differences between the structures no adverse effects are seen, even when the train speeds vary between $60\,\mathrm{km/h}$ and $350\,\mathrm{km/h}$, see Figure 7.5 [30]. The influence of the train speeds do however become apparent when an irregularity angle is introduced. Because of these findings the models created for this study focus on the vertical geometry of the rail and the train speeds. The reference measurements shown in Figure 7.3 do not show the expected and necessary behaviour of a transition zone, a transition zone should provide a smooth transition between the different rail structures [43], which the reference transition zone does not provide as seen from Figure 7.3. In the ballast-TMT transition models a transition zone with ideal behaviour is assumed over the $6\,\mathrm{m}$ transition zone length. The ideal transition zone provides a linear increase in elevation between the two rail structures.
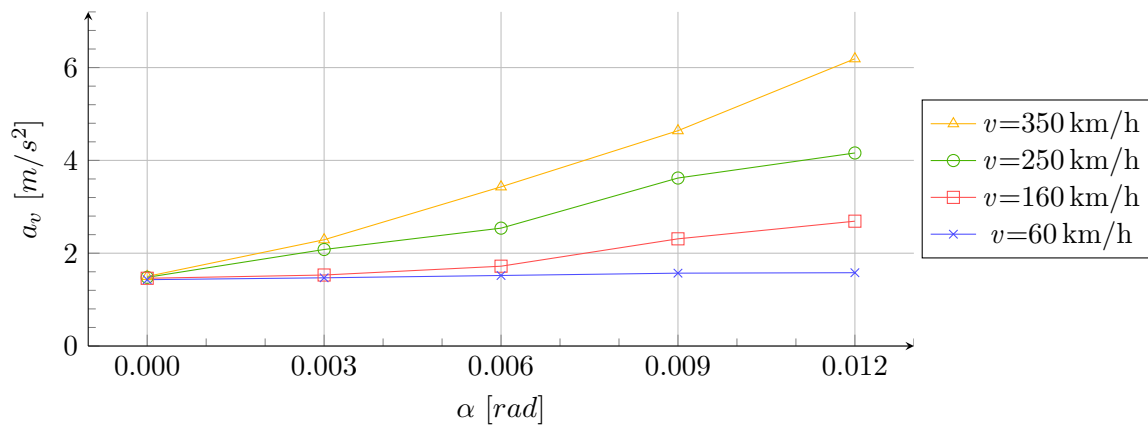


Figure 7.5: Maximum vertical accelerations ($a_v$) of a rail vehicle for different train speeds ($v$) and rail irregularity angles ($\alpha$) [30].

For the ballast-TMT transition models the implicit, dynamic step is used in the same manner as in the calibration model and boundary conditions and loading with the four wheels remain the same. A total of 16 models are created, each with a different train speed and irregularity angle, similar to the analyses performed by Lei and Mao [30] as shown in Figure 7.5. The models consists of a $10\,\mathrm{m}$ ballasted section, a $6\,\mathrm{m}$ transition section and a $10\,\mathrm{m}$ TMT section, as shown in Figure 7.6. In Figure 7.6 x is defined from the beginning of the RC beam to indicate the location of the maximum displacement, shear forces and bending moments in the results discussion. The different irregularity angles used are 0, 0.003, 0.006 and $0.012\,\mathrm{rad}$ and are equivalent to total ballasted rail settlements of 0, 18, 36 and $72\,\mathrm{mm}$ respectively. The different train speeds used are 40, 94, 160 and $250\,\mathrm{km/h}$. All the irregularity angles are applied over a distance of $6\,\mathrm{m}$, which is the length of the transition zone (approach slab) used at the reference transition, and the values of the irregularity angles are from research [30]. The $40\,\mathrm{km/h}$ train speed is representative of a freight train travelling speed [58], $94\,\mathrm{km/h}$ is the speed of the reference train, $160\,\mathrm{km/h}$ is the maximum speed of the reference train and $250\,\mathrm{km/h}$ is the minimum train speed at which a railway is considered a high-speed railway [40].
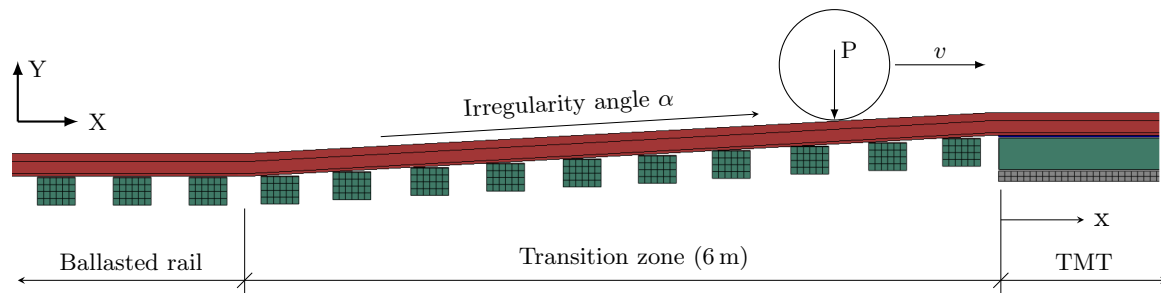
Figure 7.6: Section of the ballast-TMT transition model with an exaggerated ballasted rail settlement and irregularity angle.

### 7.1.4  Ballast-TMT Transition Models Results

The results of the different variations of the ballast-TMT transition are presented here. Maximum values of the displacements, bending moments and shear forces of each model are shown for the TMT RC beam. These results of the various models combine to create the sensitivity analysis of the RC beam with regard to train speed and irregularity angle in a transition.

**Displacements**

Figure 7.7 shows the displacement histories of four transition models at x = 0 m in the RC beam, each with a different irregularity angle and loaded at a train speed of 160 km/h. The waves present in the results after a time of 1.60 s are caused by the wheel loads being removed from the rail when they reach the end of the rail. Displacements for the RC beam show a linear increase over the irregularity angle range and minimal increase due to higher train speeds. Figure 7.8 shows the displacement sensitivity of the RC beam, measured at x = 0 m. For a train speed of 250 km/h and an irregularity angle of 0.012 rad the maximum displacement at the centre of the cross section of the RC beam is -1.58 mm.

**Bending moments**

The bending moment results are divided into maximum sagging and hogging bending moments. Figure 7.9 shows the maximum sagging bending moments obtained for the RC beam. At 250 km/h and no irregularity angle the maximum sagging bending moment is 12.89 kN.m, creating compression $\sigma_c = 3.14$ MPa and tension $\sigma_t = 2.54$ MPa stresses in the RC beam. In Figure 7.10 the maximum hogging bending moments in the RC beam are plotted. With a train speed of 250 km/h and an irregularity angle of 0.012 rad the maximum hogging bending moment is equal to -23.63 kN.m. This moment creates a compressive stress of $\sigma_c = 4.66$ MPa and a tensile stress of $\sigma_t = 5.76$ MPa in the RC beam.

The maximum sagging bending moments occur at x = 1.25 m in the RC beam for no irregularity angle and at x = 3.15 - 4.15 m for irregularity angles 0.003 - 0.12 rad. All maximum hogging bending moments occur at x = 0.85 - 1.05 m in the RC beam.
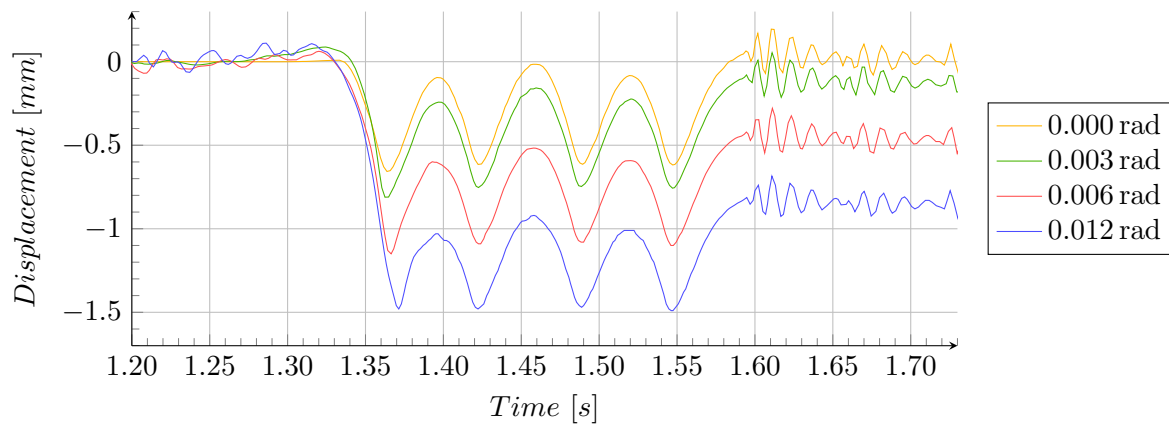
Figure 7.7: RC beam vertical displacement time histories at x = 0 m at a train speed of 160 km/h for different irregularity angles ($\alpha$).
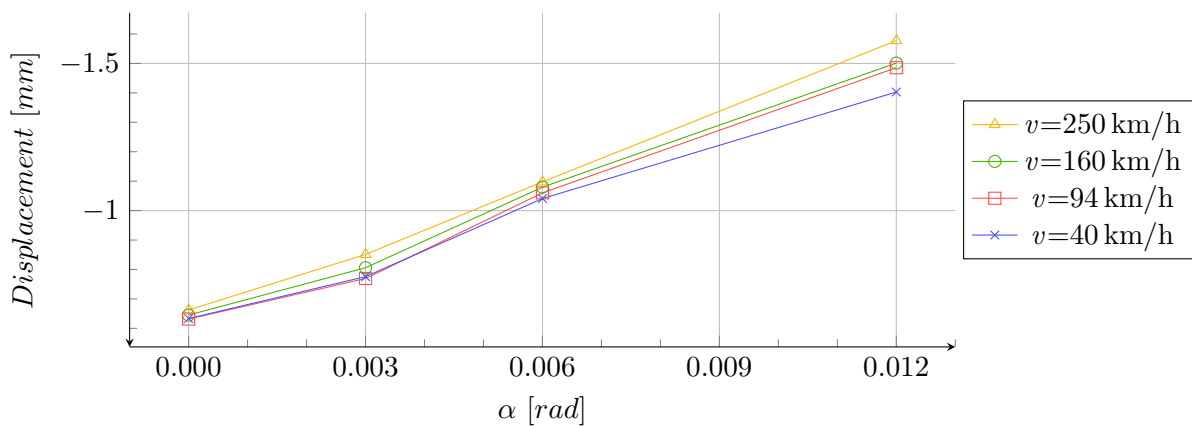


Figure 7.8: The increase in maximum displacements at x = 0 m in the TMT RC beam due to an increase in train speed ($v$) and rail irregularity angle ($\alpha$).

Figure 7.9 shows a slight decrease in maximum sagging bending moments. The sagging bending moments do not change as dramatically as the hogging bending moments because the wheel loads that cause the sagging bending moments remain constant for all models. The decrease in sagging bending moments could be attributed to the introduction of the irregularity angle and the large increase in the hogging bending moments.

**Shear forces**

Figure 7.11 shows the absolute maximum shear forces occurring in the RC beam. All maximum shear force values occur at x = 0.3 m in the RC beam. At irregularity angles of 0 and 0.003 rad and all train speeds there is no increase in the shear forces. Irregularity angles greater than 0.003 rad show an increase in shear forces and an increase in train speeds contributes to the increase of the shear forces. The maximum shear force of 53.43 kN occurs at the maximum train speed and irregularity angle of 250 km/h and 0.012 rad respectively.
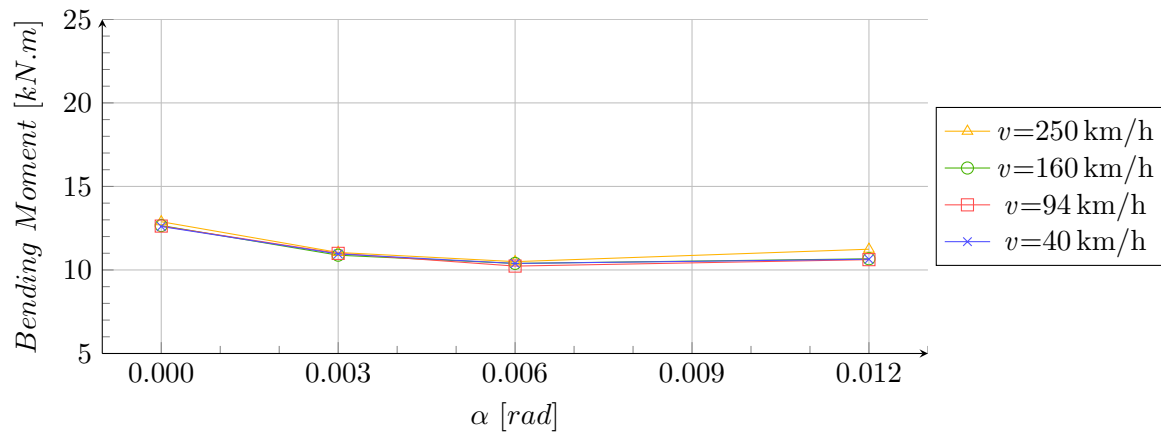
Figure 7.9: Maximum sagging bending moments at x = 1.25 m and 3.15 - 4.15 m in the TMT RC beam for different train speeds ($v$) and irregularity angles ($\alpha$).
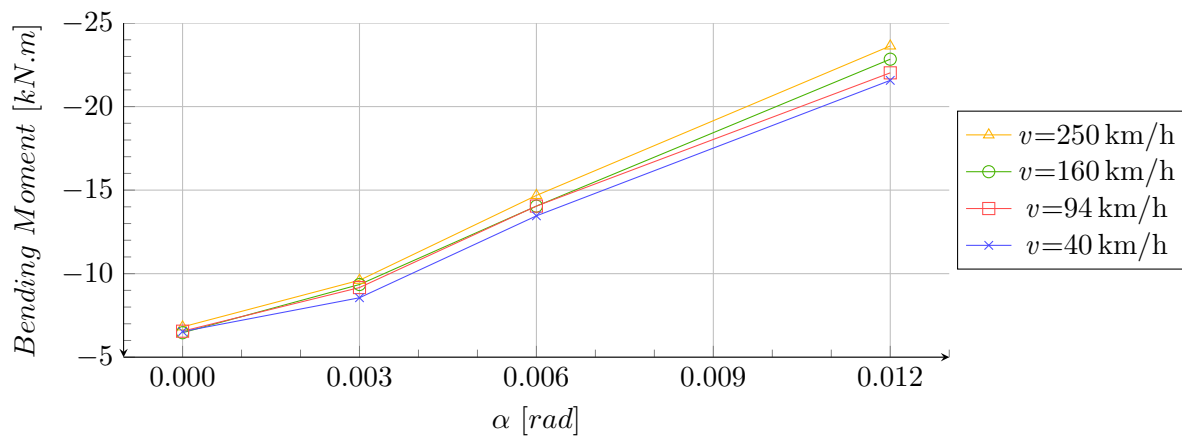


Figure 7.10: The increase in maximum hogging bending moments at x = 0.85 - 1.05 m in the TMT RC beam for increasing train speeds ($v$) and irregularity angles ($\alpha$).
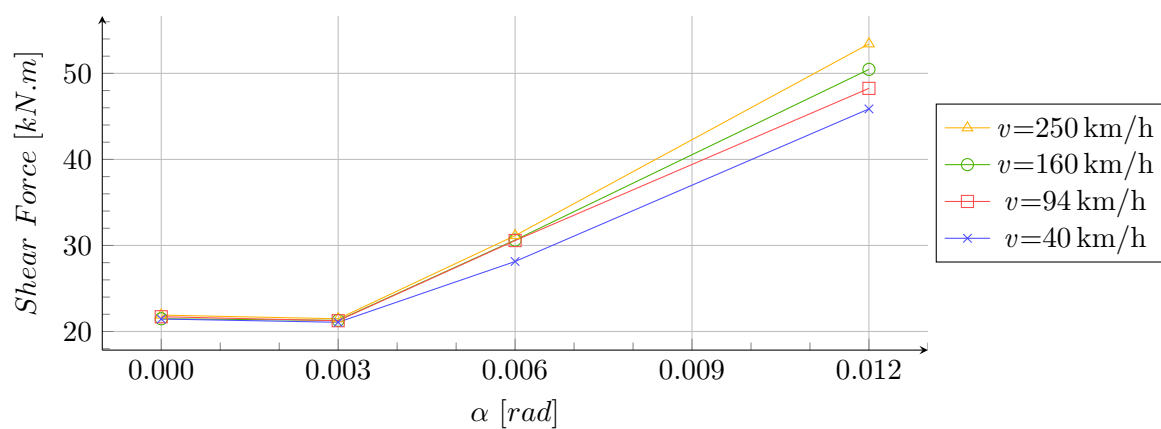


Figure 7.11: The increase in absolute maximum shear forces at x = 0.3 m in the TMT RC beam for increasing train speeds ($v$) and irregularity angles ($\alpha$).

## 7.2   Summary

One aim of this chapter was to determine whether modelling a rail transition could be accurately done with the use of a simplified 2D model. This was achieved by creating a 2D FEM model of a transition between ballasted rail and Sonneville track and the results of the model were calibrated with displacement measurements of an existing ballast-Sonneville transition. The ballast-Sonneville transition calibration model showed acceptable comparison to the reference measurements with all model displacements within 5 % of the reference measurements and a good comparison between the time histories of the reference rail and calibration model was seen. The behaviour of the reference transition was not as expected for a transition zone and a transition zone of 6 m long with a desired, uniformly changing elevation between rail structures was used in subsequent ballast-TMT transition models.

The final aim of this chapter was to determine the sensitivity of the TMT RC beam displacements, shear forces and bending moments with regard to the change in train speed and rail irregularity angle, which are the main influencing factors in the behaviour of the rail at a transition. A sensitivity analysis was performed with 16 ballast-TMT transition FEM 2D models with varying irregularity angles and train speeds.

Displacements, bending moments and shear forces were found to be sensitive to a change in irregularity angle, but the change in train speed has a minimal effect on the behaviour of the RC beam. Maximum sagging bending moments show a slight decrease, but mostly constant trend in maximum values measured, unlike the increase seen in maximum values for displacements, minimum bending moments and shear forces. The sagging moments remain constant because the wheel loads causing the sagging bending moments remain constant for all models and the slight decrease in the sagging bending moments is attributed to the change in rail geometry due to the introduction of the irregularity angle and the large increase in hogging bending moments. A summary of the results obtained for the sensitivity analysis is provided in Table 7.2.

Although research [30] shows that the difference in vertical track stiffness has little effect on the dynamic behaviour of the rail at a transition the difference in vertical stiffness leads to the initial change in vertical rail geometry and should therefore not be ignored completely. The results obtained in this chapter show that train speed and vertical rail geometry are the main contributing factors to the dynamic behaviour of the rail components at a transition. Focus, therefore, needs to be put on limiting the vertical rail settlement due to subsidence of the ballasted rail with a properly designed transition zone and regular track monitoring and maintenance. A properly designed transition zone would be a zone which limits the vertical rail settlement by increasing the vertical track stiffness of the ballast at the transition, but, more importantly, stabilizes the ballast to avoid lateral displacement, compaction and ballast degradation in order to minimize rail settlement and the irregularity angle.

Table 7.2: Summary of sensitivity analysis results.

| | Speed [km/h] | Irregularity angle, $\alpha$ [rad] | | | |
|---|---|---|---|---|---|
| | | 0 | 0.003 | 0.006 | 0.012 |
| Displacements [mm] | 40 | 0.63 | 0.78 | 1.04 | 1.40 |
| | 94 | 0.63 | 0.77 | 1.06 | 1.49 |
| | 160 | 0.65 | 0.81 | 1.08 | 1.50 |
| | 250 | 0.66 | 0.85 | 1.10 | 1.58 |
| Maximum sagging moments [kN.m] | 40 | 12.60 | 10.96 | 10.39 | 10.64 |
| | 94 | 12.63 | 10.99 | 10.23 | 10.62 |
| | 160 | 12.66 | 10.88 | 10.39 | 10.67 |
| | 250 | 12.89 | 11.04 | 10.50 | 11.24 |
| Maximum hogging moments [kN.m] | 40 | -6.53 | -8.56 | -13.56 | -21.57 |
| | 94 | -6.56 | -9.17 | -14.05 | -22.02 |
| | 160 | -6.46 | -9.35 | -14.04 | -22.84 |
| | 250 | -6.81 | -9.60 | -14.68 | -23.63 |
| Shear forces [kN] | 40 | 21.45 | 21.07 | 28.14 | 45.87 |
| | 94 | 21.72 | 21.25 | 30.57 | 48.26 |
| | 160 | 21.48 | 21.29 | 30.63 | 50.46 |
| | 250 | 21.91 | 21.48 | 31.15 | 53.43 |

# Chapter 8

# Conclusions and Recommendations

The conclusions of this study are presented in this chapter and recommendations based on the research and results are given. Also, based on the results obtained and the topics which fell outside the scope of the study some suggestions are made for future research.

## 8.1 Conclusions

The conclusions of this study are divided into three separate sections which cover the different rail structures analysed:

- Tubular Modular Track (TMT) structure

- Ballasted rail structure

- Ballast to TMT transition assembly — this last section contains the most important conclusions of this study

### 8.1.1 FEM Modelling and Analysis of TMT Structures

Using the method of the elastic foundation theory to replace the subgrade with an elastic spring model greatly simplifies the modelling of the TMT model and provides accurate behaviour of the structure under loading. The subgrade stiffness, used for the elastic foundation theory, can be obtained by modelling a square plate bearing test (PBT) of the subgrade.

The TMT structure can be modelled in 3D, which provides detailed insight on the behaviour of the structure when loaded. However, the 3D model can become computationally expensive due to the fine mesh size required to model the cross-section of the components and the relatively long length of the components. Extraction of results for a 3D model is time consuming, because bending moment and shear force results are not directly available in the model output and need to be calculated from cross-sectional stresses.

Simplifying the TMT model from 3D to 2D allows faster analysis of the structure as well as faster changes to the design, loading, assembly of the structure and analysis results extraction. In a 2D model the bending moments and shear forces are available as an output for the beam elements used in the 2D model of the rail assembly consisting of the rail, elastomeric pad, RC beam and grout. Compared to the 3D model results the results of the 2D rail are underestimated by acceptable margins, except for the bending moments, which are underestimated by 10 %. In the RC beam the displacement and shear force results are overestimated within acceptable margins and the bending moments are overestimated by 14 %. Even though this overestimation falls outside typical acceptable margins the results can be used because this would lead to a conservative design and an included safety factor for the design of the RC beam.

Modelling the structure in 2D allows modelling of the train wheels as 2D discs. This is a simpler method than applying the 3D wheel loads as Hertz theory contact points or modelling a complex 3D wheel. Using Hertz theory contact points for dynamic load application becomes an involved process where the load point spacing and time increments need to be investigated and a 3D wheel would need a fine mesh to model the complex geometry of the wheel. A 2D wheel avoids the use of point loads and the Hertz contact theory. It does not apply the wheel load as a point load, but as a distributed load similar to the Hertz contact theory; and a fine mesh is not required for the wheel, minimizing the computational cost of the model.

### 8.1.2   DEM and FEM Modelling and Analysis of Ballasted Rail Structures

A ballasted rail section can be modelled with the discrete element method (DEM), but creating a model which accurately represents the behaviour of the structure is a time consuming and complex exercise. Creating the discrete particles is complex, since discrete particles are not available in Abaqus/CAE and DEM analysis is only available in Abaqus/Explicit and in 3D, which restricts the model to certain modelling methods and element types and does not allow 2D simplification or the use of the elastic foundation option. Interaction properties between the particles and finite element (FE) components require extensive research to obtain the correct values, such as friction coefficient, normal contact force and shear contact force. This approach can be avoided by using a trial and error approach by changing the interaction properties until the required results are obtained, this approach requires field or lab test results to calibrate the model results against.

Results obtained for the ballasted rail DEM 3D model did not show the expected behaviour of the ballasted structure. This could be caused by limitations in the software used with respect to the ballast material modelling and the analysis process using DEM behaviour, preventing the analysis process to reach convergence and yield plausible results. A convergence error terminated the analysis procedure and created excessive distortion in the rail pad, creating irregularities in the rail results. Since it falls outside of the scope of this study to resolve issues within the new DEM software the obtained results were merely presented for future reference.

Field measurements of a ballasted rail section on the same rail where the transition reference measurements were taken show that ballast behaves linearly under load application and the

linear behaviour of the ballast is supported by the elastic foundation theory. Because of the linear behaviour of the ballast the ballasted model can be greatly simplified by applying the elastic foundation theory to replace the ballast particles and the subgrade with elastic supports. The reference field displacement measurements of the ballasted rail were used to obtain and calibrate the stiffness of the supporting ballast and subgrade.

Using the elastic foundation method with the obtained supporting ballast and subgrade stiffness to simplify the ballasted model allows the use of 2D simplification, which significantly decreases the computational cost and effort required for the DEM model. The results obtained by the simplified 2D model yield results which are comparable to reference measurements. A summary of the results obtained for the separate TMT and ballast models is shown in Table 6.3. Ballast behaviour such as settlement and deterioration is not modelled when using the elastic foundation assumption. Displacement results of the 2D ballasted model show the sleepers behaving independently and displacements in-between wheel loads quickly returning to unloaded values. The reference measurements show that the loaded sleepers have an effect on neighbouring sleepers and displacements do not return to zero in-between the application of the wheel loads.

### 8.1.3   FEM Modelling and Analysis of a Ballast-TMT Transition Assembly

The conclusions presented in this section are for the ballast-TMT transition model, the investigation of which was the main research objective of this study: the physical behaviour of the rail structure at the transition between TMT and ballasted rail and the sensitivity of the TMT structure to train speed and rail irregularity angle.

A comparison between a reference transition zone with field measurements and a calibration model, displayed in Figure 7.3 and Table 7.1, shows that a transition can be modelled in a finite element method (FEM) package with simplified 2D models. The field measurements of the transition zone were performed on an existing railway transition. Across the length of the transition displacement measurements were taken on the rail at five points. One measurement point was placed on the ballasted rail section, before the transition zone, three points were placed on the rail within the transition zone and one point was placed on the rail at the first concrete block on the Sonneville track.

The sensitivity analysis of the RC beam in the ballast-TMT transition was performed using a fixed transition zone length of 6 m, which is equal to the transition zone length of the reference transition. Over the transition zone length various irregularity angles were applied to simulate different degrees of ballasted rail settlement. For each of the irregularity angles the train speeds were varied between 40 and 250 km/h. The maximum displacements, bending moments and shear forces extracted from these various models were presented together to show the sensitivity of the TMT RC beam toward the change in irregularity angle and train speed in Figures 7.8, 7.9, 7.10 and 7.11 and Table 7.2.

Displacement results show that the displacement sensitivity of the RC beam exhibits linear behaviour where the displacements increase by 150 % from the minimum displacement to the

maximum displacement for an increase in both train speed and irregularity angle. All maximum displacements occur at x = 0 m in the RC beam.

The maximum sagging bending moments occur at x = 1.25 m in the RC beam for no irregularity angle and at x = 3.15 - 4.15 m for irregularity angles 0.003 - 0.12 rad. All maximum hogging bending moments occur at x = 0.85 - 1.05 m in the RC beam.

A slight decrease of 20 % is seen in maximum sagging bending moments. The sagging bending moments do not change as dramatically as the hogging bending moments because the wheel loads that cause the sagging bending moments remain constant for all models. The decrease in sagging bending moments could be attributed to the introduction of the irregularity angle and the large increase in the hogging bending moments. The increase of 310 % in the maximum hogging bending moments is attributed to the introduction and increase of the irregularity angle which causes greater hogging bending behaviour in the TMT RC beam.

Shear forces in the RC beam are not affected at irregularity angles of 0 and 0.003 rad and all train speeds. Irregularity angles higher than 0.003 rad at all train speeds increase the shear forces linearly with 150 % at x = 0.3 m in the RC beam.

Research has shown that the difference in vertical track stiffness has no significant effect on the dynamic behaviour of the rail components at a transition, but the difference in track stiffness leads to the initial change in vertical rail geometry and should therefore not be ignored completely [30].

The sensitivity analysis of the TMT structure shows that the sectional forces in the RC beam are increased due to an increase in both train speed and rail irregularity angle. By slowing trains down at a transition the increase in sectional forces that the RC beam is subjected to can be decreased. However, avoiding large irregularity angles through regular rail inspection and maintenance is of utmost importance. A properly designed transition zone, which increases the vertical track stiffness and stabilizes the ballast to prevent settlement, lateral displacement and deterioration of the ballast, will show a more significant decrease in the negative impacts on the RC beam.

## 8.2    Recommendations

This section makes recommendations for the analysis of the ballast-TMT transition based on the results obtained for this study and the conclusions made.

The TMT structure can be modelled in both 3D and 2D. For detailed component analyses a 3D model is recommended, but for a generalised analysis as in this study a 2D model is recommended due to the simplification and accurate results. The elastic foundation is recommended for both 2D and 3D models since it greatly simplifies the model and yields accurate results. It is, however, also recommended that the results of the PBT for the modulus of subgrade reaction be verified with field test results since soil foundation properties are difficult to predict.

DEM models are recommended for more in-depth investigations on the ballast itself, such as box-tests, inter-particle behaviour investigations and ballast models where settlement or deterioration are required. Investigation of ballast particle and inter-particle behaviour is recommended for these in-depth DEM models in order to achieve a model which better represents the real behaviour of the particles. Based on experience gained in this study DEM models are not recommended for large models of rail sections since an elastic foundation assumption provides accurate behaviour of the ballasted structure.

It is recommended that 2D models be used for the analysis of a long section of rail where only vertical loads are investigated. For a general investigation into rail behaviour a 2D model provides adequate insight into the behaviour of the structure. When investigating a more detailed aspect of the structure a 3D model may be required to provide better insight into topics such as stresses and strains or contact pressures.

Since the permanent settlement of the ballast at the transition (irregularity angle) is the main contributor to the negative dynamic behaviour of the rail the following recommendations can be considered to restrict ballast settlement:

- a containment structure, with walls along the side of the ballast and placed at the end of the ballasted rail at the transition, that restricts ballast settlement and prevents lateral ballast "flow" could ensure a smaller irregularity angle and decrease the required regular track maintenance at a transition;

- a bonding agent, such as bitumen, should increase the stiffness of the ballast slightly and prevent the ballast from "flowing" and creating an excessive irregularity angle; and

- regular transition maintenance, rail inspection and control of train speeds to avoid accelerated ballast settlement and irregularity angles becoming excessive is required.

## 8.3 Suggestions for Future Research

Suggestions for future research are presented in this section based on the topics which fell outside the scope of this study and based on the results obtained in this study.

Results shown for this study only include displacements, bending moments and shear forces. Future research could perform analyses on the transition and investigate other results such as accelerations, wheel contact forces, permanent displacements, component stresses and subgrade stresses. Parameters like train mass and train vehicle geometry can be included in the research parameters to provide insight into various types of railways for different trains.

The analyses in this study were performed on typical transition zones in order to perform the sensitivity analysis of the RC beam. Future research could perform an in-depth analysis on a transition with a specific transition zone in order to determine the impacts of the specific transition zone on the rail behaviour. For such a detailed investigation of the transition zone a DEM model would provide better insight into the behaviour of the ballast at the transition.

If an in-depth investigation is done on the ballast at the transition the research could include aspects such as ballast degradation and particle clumping. Ballast degradation could be an important contributing factor to the settlement at a transition and particle clumping should increase the accuracy of the particle behaviour, because clumped particles have irregular surfaces which should create better interaction between the particles and show more realistic ballast behaviour.

Before an in-depth investigation can be made on the ballast behaviour at a transition the ballast properties and behaviour need to be investigated and defined. The properties of granular materials for DEM analyses are available, but particle material properties are not scalable according to particle size. For different particles sizes and gradings the properties need to be redefined. Future research could investigate the ballast properties of the specific ballast used in this study.

At the transition between ballast and TMT a concentration is expected in the subgrade stresses and the TMT RC beam end stresses, because the RC beam support is no longer continuous. A detailed investigation of the subgrade at the end of the RC beams could show whether compaction of the subgrade occurs below the RC beams and if this contributes to the negative impacts of the transition on the rail structures.

In the 2D model the sleepers are supported discretely, but in practice sleepers are affected by the movement of adjacent sleepers. This effect is not included in this study. Including the effect of adjacent sleepers in future research will yield results which should compare better to field measurements.

Future research should include the sprung mass of the train vehicles and the participating mass of the ballast and soil below the structures. Excluding these masses result therein that the mass included in the models is very low. This will have a significant impact on the results of the dynamic analyses performed on the models.

# Bibliography

[1] Academia. Some useful numbers on the engineering properties of materials [internet], 2000 [cited 2014 Apr 8]. Available at: `http://www.academia.edu/4156626/Some_Useful_Numbers_on_the_Engineering_Properties_of_Materials_Geologic_and_Otherwise_Angle_of_internal_friction`.

[2] P. Antolín, N. Zhang, J.M. Goicolea, H. Xia, M.A. Astiz, and J. Oliva. Consideration of nonlinear wheel-rail contact forces for dynamic vehicle-bridge interaction in high-speed railways. *Journal of Sound and Vibration*, 332(5):1231–1251, 2013.

[3] F. Augsburg and U. Schüller. "Railway Undercarriage With a Radially Adjustable Wheel Axles", U.S. Patent 7 066 095, June, 2006.

[4] J. Blanco-Lorenzo, J. Santamaria, E.G. Vadillo, and O. Oyarzabal. Dynamic comparison of different types of slab track and ballasted track using a flexible track model. *Proceedings of the Journal of Rapid Transit*, 225(6):574–592, November 2011.

[5] J.E. Bowles. *Foundation analysis and design.* New York: McGraw-Hill, 5th edition, 1997.

[6] H.A. Buchholdt and S.E.M. Nejad. *Structural dynamic for engineers.* London: ICE publishing, 2nd edition, 2012.

[7] A.K. Chopra. *Dynamics of Structures - Theory and Applications to Earthquake Engineering.* Pearson Prentice Hall, 2007.

[8] R.F. Craig. *Craig's soil mechanics.* London: Spon Press, 7th edition, 2004.

[9] R.R. Craig Jr. and A.J. Kurdila. *Fundamentals of Structural Dynamics.* New Jersey: John Wiley & Sons, 2nd edition, 2006.

[10] D. Cui, L. Li, X. Jin, X. Xiao, and J. Ding. Influence of vehicle parameters on critical hunting speed based on Ruzicka model. *Chinese Journal of Mechanical Engineering*, 25(3):536–542, 2012.

[11] P.A. Cundall. A computer model for simulating progressive large-scale movements in block rock mechanics. In *In Proceedings of the symposium of the International Society for Rock Mechanics*, volume 1, 1971.

[12] Dassault Systémes. *Abaqus Analysis User's Guide*, Abaqus 6.14 edition.

[13] Dassault Systémes. *Abaqus Exmaple Problems Guide*, Abaqus 6.14 edition.

[14] Dassault Systémes. *Abaqus Theory Guide*, Abaqus 6.14 edition.

[15] C. Esveld. Innovations in railway track. In *Rail technology advancements in the Netherlands. International conference*, pages 15–1, 1997.

[16] C. Esveld. *Modern Railway Track*. MRT-Productions, Delft, Netherlands, 2nd edition, 2001.

[17] H. Feng. 3D-models of railway track for dynamic analysis. Master's thesis, Royal Institute of Technology, 2011.

[18] R.J. Furno. Formation measurements on tubular and conventional track at Amandelbult for the period Nov 2004 to Aug 2005. Technical Report March 2006, Spoornet, 2006.

[19] Gautrain. Track laying sequence [internet], 2009 Jul 3 [cited 2013 Nov 15]. Available from: `http://www.gautrain.co.za/construction/2009/07/track-construction/`.

[20] P.J. Gräbe. Tubular track tames the desert [internet], 2012 [cited 2013 Nov 15]. Available from: `http://www.railjournal.com/index.php/track/tubular-track-tames-the-desert.html`.

[21] H.M. Hilber, T.J.R. Hughes, and R.L. Taylor. Algorithms in structural dynamics. *Earthquake Engineering and Structural Dynamics*, 5(June 1976):283–292, 1977.

[22] H. Huang and S. Chrismer. Discrete element modeling of ballast settlement under trains moving at critical speeds. *Construction and Building Materials*, 38:994–1000, January 2013.

[23] H. Huang and E. Tutumluer. Discrete element modeling for fouled railroad ballast. *Construction and Building Materials*, 25(8):3306–3312, August 2011.

[24] J.L. Humar. *Dynamics of Structures*. CRC Press, 2012.

[25] B. Indraratna, N.T. Ngo, C. Rujikiatkamjorn, and J.S. Vinod. Behaviour of fresh and fouled railway ballast subjected to direct shear testing - A discrete element simulation. *International Journal of Geomechanics*, 14(1):34–44, 2014.

[26] Itasca Consulting Group Inc. *PFC3D - Particle Flow Code in 3 Dimensions - Theory and Background*, PFC3D 4.00 edition.

[27] F. Jin, C. Zhang, W. Hu, and J. Wang. 3D mode discrete element method: Elastic model. *International Journal of Rock Mechanics and Mining Sciences*, 48(1):59–66, January 2011.

[28] K. L. Johnson. *Contact Mechanics*. Cambridge University Press, 1987.

[29] B. Le Roux. Tubular track offers rail support at a competitive price. *Railway Gazette International*, 161(9):553–554, 2005.

[30] X. Lei and L. Mao. Dynamic response analyses of vehicle and track coupled system on track transition of conventional high speed railway. *Journal of Sound and Vibration*, 271(3-4):1133–1146, 2004. Cited By (since 1996):30.

[31] W.L. Lim and G.R. McDowell. Discrete element modelling of railway ballast. *Granular Matter*, 7(1):19–29, 2005. Cited By (since 1996):43.

[32] S. Lobo-Guerrero and L.E. Vallejo. Discrete element method analysis of railtrack ballast degradation during cyclic loading. *Granular Matter*, 8(3-4):195–204, 2006. Cited By (since 1996):35.

[33] M. Lu and G.R. McDowell. The importance of modelling ballast particle shape in the discrete element method. *Granular Matter*, 9(1-2):69–80, 2007. Cited By (since 1996):49.

[34] G.R. McDowell, W.L. Lim, A.C. Collop, R. Armitage, and N.H. Thom. Comparison of ballast index tests for railway trackbeds. In *Proceedings of the institution of civil engineers: Geotechnical engineering*, volume 157, pages 151–161, 2004. cited By (since 1996)13.

[35] G. Mitchell. Electronic communications, November 2014.

[36] A.V. Mittal and S.K. Maurya. Ballast Specification for High Axle Load (32.5T) and High Speed ($\geq$ 250kmph). *Indian Railways Institute of Civil Engineering, India*, n.d.

[37] J.S. Mundrey. Tracking for high-speed trains in india. *RITES*, 12(1):1–16, 2010.

[38] A.R. Pérez Winkler. An investigation of overhead crane wheel / rail / girder interaction. Master's thesis, University of Stellenbosch, 2003.

[39] RAIL.ONE. Concrete sleepers b70: The classic sleepers [internet], 2014 [cited 2014 Aug 18]. Available from: `http://www.railone.com/products-solutions/railways-and-commuter-traffic/ballasted-track-systems/concrete-sleepers-b70/`.

[40] S. Rashid. Parametric study of bridge response to high speed trains: Ballasted track on concrete bridges. Master's thesis, KTH Royal Institute of Technology, 2011.

[41] G. Saussine, C. Cholet, P.E. Gautier, F. Dubois, C. Bohatier, and J.J. Moreau. Modelling ballast behaviour under dynamic loading. part 1: A 2d polygonal discrete element method approach. *Computer Methods in Applied Mechanics and Engineering*, 195(19-22):2841–2859, 2006. Cited By (since 1996):45.

[42] M. Sebes, L. Chevalier, J. Ayasse, and H. Chollet. A fast-simplified wheel-rail contact model consistent with perfect plastic materials. *Vehicle System Dynamics*, 50(9):1453–1471, 2012.

[43] Y. Shan, B. Albers, and S.A. Savidis. Influence of different transition zones on the dynamic response of track-subgrade systems. *Computers and Geotechnics*, 48:21–28, 2013.

[44] F.J. Shaw. Dolomite ballast track report. Technical report, Bombela Maintenance (Pty) Ltd., 2011.

[45] F.J. Shaw. Transitions between tubular modular track and conventional track. Technical report, Tubular Track (Pty) Ltd., 2012.

[46] F.J. Shaw. Electronic communications, November 2013.

[47] Sonneville. Low vibration track (LVT) [internet], 2015 [cited 2015 Jul 8]. Available from: `http://www.sonneville.com/en/low-vibration-track-lvt/`.

[48] TATA Steel. Tata steel - rail technical guide [internet], 2013 [cited 2013 November 15]. Available from: `http://www.tatasteeleurope.com/en/products-and-services/long/rail/rail`.

[49] M.J.M.M. Steenbergen. Physics of railroad degradation: The role of a varying dynamic stiffness and transition radiation processes. *Computers and Structures*, 124:102–111, 2013. Article in Press.

[50] A.H. Stroud. *Approximate Calculation of Multiple Integrals*. Englewood Cliffs, N.J.: Prentice-Hall, 1971.

[51] Pandrol Track Systems. Pandrol fastclip FE [internet], 2014 [cited 2015 Mar 17]. Available from: `http://pandrol.com/product/pandrol-fastclip-fe`.

[52] C. Tengstrom. T-Track [internet], 2010 [cited 2013 Jun 18]. Available from: `http://www.slideshare.net/imadhammoud/mr-craig-tengstrm-kuwait-metro-and-rail?from_search=1`.

[53] K. Terzaghi. Evaluation of coefficient of subgrade reaction. *Geotechnique*, 5:297–326, 1955.

[54] The Engineering Toolbox. Material properties [internet], 2015 [cited 2015 Feb 24]. Available from: `http://www.engineeringtoolbox.com/`.

[55] Tubular Track. What is TMT? [internet], 2013 [cited 2013 Aug 5]. Available from: `www.tubulartrack.co.za/index.php/tubular-modular-track/what-is-tmt/`.

[56] E. Tutumluer, Y. Qian, Y.Y.M.A. Hashash, and J. Ghaboussi. Field validated discrete element model for railroad ballast. *AREMA 2011 Annual Conference*, 2011.

[57] J.C. Van Schalkwyk. Techniques for the Stiffening and the Control of the Displacement of Railway Ballast. Final year project, University of Stellenbosch. 2012.

[58] K.J.S. Verlinde. Finite element analysis of tubular track system. Master's thesis, University of Stellenbosch, 2012.

[59] W. Yan and F.D. Fischer. Applicability of the hertz contact theory to rail-wheel contact problems. *Archive of Applied Mechanics*, 70(4):255–268, 2000. Cited By (since 1996):32.